Engineering Journal

AISC — AMERICAN INSTITUTE OF STEEL CONSTRUCTION — FOUNDED 1921

Smarter. Stronger. Steel.

Engineering Journal

American Institute of Steel Construction

Dedicated to the development and improvement of steel construction, through the interchange of ideas, experiences and data.

The articles contained herein are not intended to represent official attitudes, recommendations or policies of the Institute. The Institute is not responsible for any statements made or opinions expressed by contributors to this Journal.

The opinions of the authors herein do not represent an official position of the Institute, and in every case the officially adopted publications of the Institute will control and supersede any suggestions or modifications contained in any articles herein.

The information presented herein is based on recognized engineering principles and is for general information only. While it is believed to be accurate, this information should not be applied to any specific application without competent professional examination and verification by a licensed professional engineer. Anyone making use of this information assumes all liability arising from such use.

Manuscripts are welcomed, but publication cannot be guaranteed. All manuscripts should be submitted in duplicate. Authors do not receive a remuneration. Guidelines for authors are printed on the inside back cover.

Engineering Journal (ISSN 0013-8029) is published quarterly. Subscriptions: Members: one subscription, $40 per year, included in dues; Additional Member Subscriptions: $40 per year. Non-Members U.S.: $160 per year. Foreign (Canada and Mexico): Members $80 per year. Non-Members $160 per year. Published by the American Institute of Steel Construction at 130 E Randolph Street, Suite 2000, Chicago, IL 60601.

Periodicals postage paid at Chicago, IL and additional mailing offices.

Postmaster: Send address changes to *Engineering Journal* in care of the American Institute of Steel Construction, 130 E Randolph Street, Suite 2000, Chicago, IL 60601.

Subscriptions: subscriptions@aisc.org, 312.670.2400

Archives: Search at **www.aisc.org/ej**. Article downloads are free for current members and are avaialable for a nominal fee for non-members.

Letter from the Editor
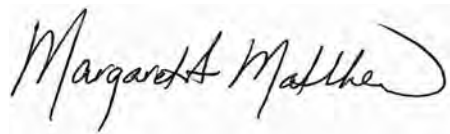
Dear Readers,

Hello and Happy New Year! As we head into the new year, I would like to take this opportunity to recognize all of the hard work of our reviewers, last year and every year. Their contributions are invaluable to the success of the *Journal* as we continue to strive to bring you the very best papers and information in the steel construction industry. A list of our 2018 reviewers is posted on the AISC web site at www.aisc.org/ej.

Is there a steel design topic you would like to see in *EJ*? We are always looking for ideas for papers. Authors interested in submitting papers should visit our web site at www.aisc.org/ej for author guidelines and submittal information.

Best wishes for a healthy and happy 2019!

Best Regards,

Margaret A. Matthew, P.E.
Editor

Observations from Cyclic Tests on Deep, Wide-Flange Beam-Columns

Paper by GULEN OZKULA, JOHN HARRIS and CHIA-MING UANG
(First Quarter 2017)

Discussion by BRUCE F. MAISON

The writer congratulates the authors for a truly impressive number of lab tests on beam-columns (Ozkula et al., 2017). Such data are valuable for advancing our knowledge of actual component behaviors in step with the gaining popularity of performance-based seismic design. The purpose of this Discussion is to point out that component backbone curves are strongly influenced by the specimen loading history (protocol) used in lab tests, and realistic seismic loading protocols ought to be included when formulating backbone curves.

The loading protocols used in the authors' tests were mostly those from AISC 341 (AISC, 2010) consisting of fully reversed cyclic loading at progressively increasing peak displacement amplitudes. The AISC 341 loading protocol is for moment connection qualification in new construction. It provides evidence that a component satisfies certain ductility requirements and is a consistent way to compare the relative performance of different components. The protocol does not mimic actual earthquake loading histories and is *not* specifically intended for use in backbone curve formulation. As a result, backbone curves derived from the envelope of cyclic test data may not adequately describe component behavior at near-collapse inelastic displacement levels (FEMA, 2009). The component ductility can be significantly underestimated. Loading protocols used in tests to demonstrate connection qualification are not the same as those for backbone curve formulation.

Figure 1 illustrates the significant difference in component response resulting from the loading protocol used in the test. A backbone curve based on the cyclic envelope would be appropriate if the earthquake generates numerous fully reversed cycles of response, but the monotonic test would be a better backbone if the quake generates few cycles. Near-collapse seismic response is more like a monotonic as opposed to fully reversed cyclic loading (Krawinkler, 2009). Note how the strength deterioration in the authors' backbone curve is an artifact from the load reversal points in the loading protocol.

The authors' study included one test of strong-axis bending under monotonic loading. Backbone curves for the Group 2 tests (W24×131) are shown in Figure 2. Specimen 2L-P (monotonic loading) had no strength deterioration at a story-drift ratio (SDR) of 4%. However, specimen 2L (fully reversed cyclic loading) had notable strength deterioration. The authors' observation that most of the strong-axis bending specimens were not able to deliver a plastic rotation of 0.03 radian is relevant to AISC 341 component qualification requirements. However, in the context of actual earthquake performance, the observation is not as ominous as might be perceived by the casual reader. Albeit, more tests using realistic earthquake loading histories are needed for confirmation.

The new ASCE 41-17 (2017) recognizes the importance of loading protocols and provides additional freedom in protocol selection to better reflect actual seismic demand patterns. It does not prescribe a specific "one-size-fits-all" loading protocol due to the wide variation of factors involved with a particular component—for example, performance objective, type of structure, and seismic setting. To ensure reasonable protocols are selected for a particular component and project, concurrence is required by independent peer reviewers experienced with the use of test data in design and analysis of structures.

Figure 3 shows a loading protocol depicting a median building response from a maximum considered earthquake (MCE). It is based on statistics from analysis of a four-story building model subjected to numerous earthquake records (Maison and Speicher, 2016). Note how the protocol has a bias in the positive direction and relatively few response cycles. A monotonic push to component failure is added at the end of the cycling portion to capture response at large near-collapse displacement levels. Another protocol based on long duration earthquakes has a similar pattern but with more response cycles (Maison and Speicher, 2018).

Because most prior component tests were performed using fully reversed cyclic loadings, ASCE 41-17 allows

Bruce F. Maison, Consulting Engineer, El Cerrito, CA.
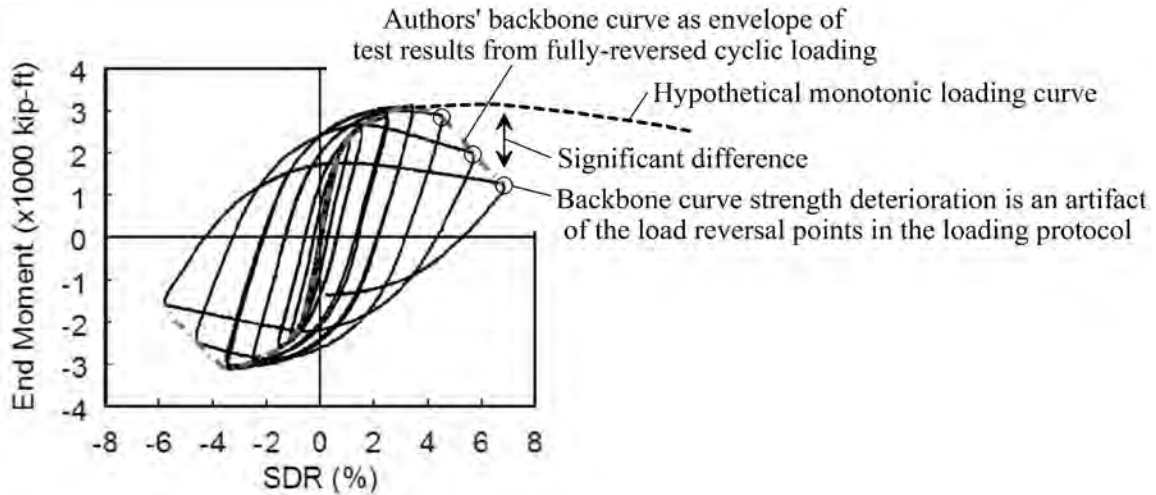Email: maison@netscape.com

Fig. 1. Comparison of backbone curves derived from fully reversed and
monotonic loading protocols (adapted from Fig. 11a of Ozkula et al., 2017).
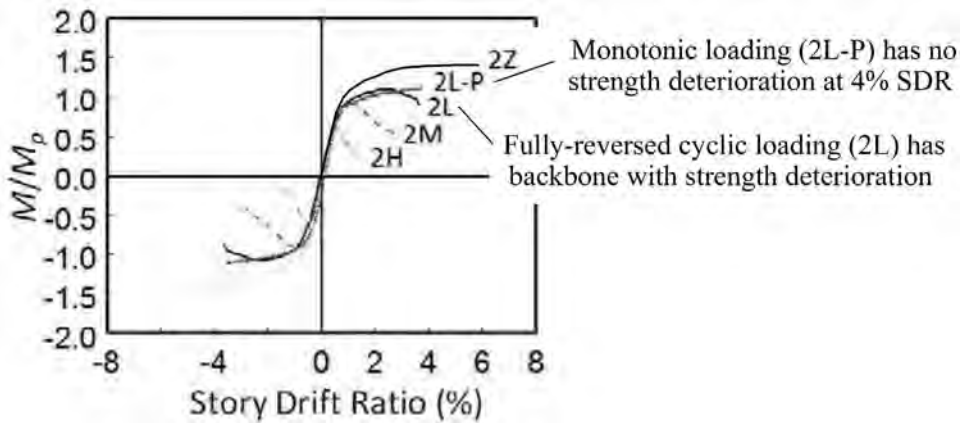

Fig. 2. Backbone curves derived from Group 2 (W24×131) lab tests (adapted from Fig. 12b of Ozkula et al., 2017)
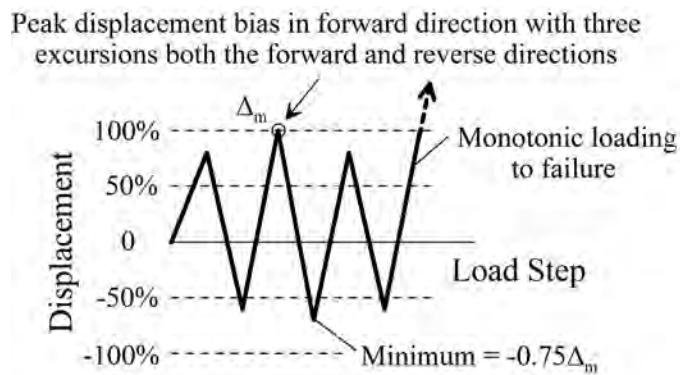

Fig. 3. MCE level median loading protocol (adapted from Fig. 18 of Maison and Speicher, 2016).

such test data to be supplemented to better define behavior at large near-collapse displacement levels. It is permitted to combine cyclic and monotonic test data in the formulation of backbone curves in cases where the cyclic tests show specimen strength degradation that is an artifact of the loading protocol as that shown in Figure 1. Figure 4 from ASCE 41-17 illustrates one way this can be done. As a precaution, a displacement limit is placed in the monotonic data leading to the abrupt decline in the backbone at point *E*.

In closing, the writer appreciates the value of the authors' research but encourages the inclusion of test data from realistic earthquake and/or monotonic load patterns in the future to supplement AISC 341 cyclic testing, thus providing more comprehensive results that are better suited for ASCE 41 backbone curve formulation.

REFERENCES

AISC (2010), *Seismic Provisions for Structural Steel Buildings,* ANSI/AISC 341-10, American Institute of Steel Construction, Chicago, IL.

ASCE (2017), *Seismic Rehabilitation of Existing Buildings*, ASCE/SEI 41-17, American Society of Civil Engineers, Reston, VA.

FEMA (2009), "The Effects of Strength and Stiffness Degradation on Seismic Response," Technical Report FEMA P-440A, Federal Emergency Management Agency, Washington, DC.

Krawinkler, H. (2009), "Loading Histories for Cyclic Tests in Support of Performance Assessment of Structural Components, *Proceedings of the 3rd International Conference on Advances in Experimental Structural Engineering (3AESE)*, San Francisco, October.

Maison, B.F., and Speicher, M.S. (2016), "Loading Protocols for ASCE 41 Backbone Curves," *Earthquake Spectra*, Vol. 32, No. 4, November.

Maison, B.F., and Speicher M.S. (2018), "Importance of Experiment Loading Protocols in Developing ASCE 41-17 Backbone Curves," *11th U.S. National Conference on Earthquake Engineering,* Earthquake Engineering Research Institute, Los Angeles, CA, June.

Ozkula, G., Harris, J., and Uang, C.M. (2017), "Observations from Cyclic Tests on Deep, Wide-Flange Beam-Columns," *Engineering Journal*, AISC, Vol. 54, No. 1, pp. 45–59.
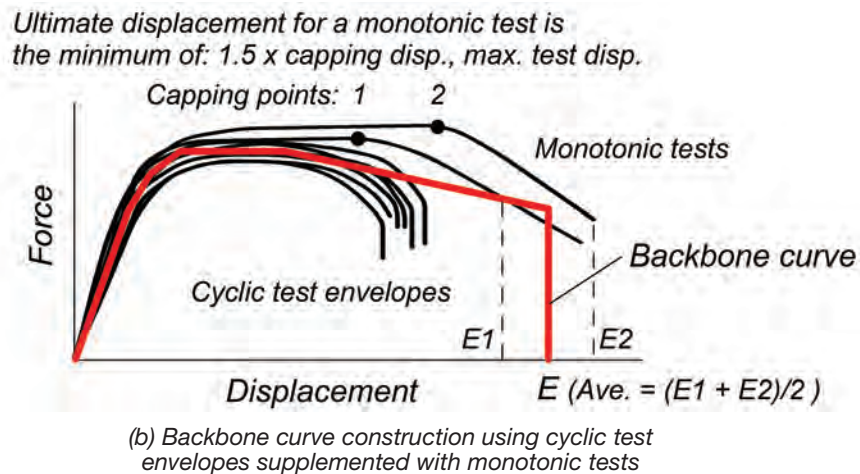
(b) Backbone curve construction using cyclic test envelopes supplemented with monotonic tests

Fig. 4. Illustration of backbone curve derived from combination of cyclic and monotonic test data [adapted from Fig. 7-6 of ASCE 41-17 (2017)].

Clearance for Welded Joints

BO DOWSWELL

ABSTRACT

Inadequate clearance can affect weld quality and efficiency. In extreme cases, obstructions may cause a lack of fusion between the base metal and the weld metal, causing a reduction in strength. Although flux cored arc welding (FCAW) and gas metal arc welding (GMAW) have replaced shielded metal arc welding (SMAW) as the primary fabrication processes for structural steel fabrication, existing clearance recommendations are based on the SMAW process. Because the geometry of a FCAW or GMAW welding gun is much different from that of a SMAW electrode, the historic values recommended for the SMAW process may not apply to FCAW and GMAW.

Experimental specimens were fabricated with the FCAW process to determine practical limits on connection geometry for welding joints with limited access. Each specimen was evaluated by sectioning and etching the weld at two locations along the length. Two weld clearance issues are addressed: (1) fillet welding near obstructions and (2) doubler plate welds.

The obstructed fillet weld specimens were used to determine the minimum clearance requirements for joints welded with the FCAW process. The cross-sectioned welds showed that as the distance between the weld and the obstruction plate decreased, both the production efficiency and the penetration into the base metal decreased. Revised clearance recommendations for FCAW and GMAW welding were proposed.

The doubler plate specimens were used to provide information regarding the root-pass penetration for square-cut plates, based on the plate thickness and the distance from the inner surface of the flange to the edge of the plate. The results of this study, which was limited to only eight specimens, validated the common practice of cutting the edge square at doubler plates less than ⅜ in. thick. For doubler plates thicker than ¼ in., a groove angle, α, of 15° to 30° may be required to ensure consistent weld quality.

Keywords: welded joints, FCAW, GMAW, doubler plates, weld clearance.

INTRODUCTION

Although strength is the primary consideration for welded joints, proper joint clearance is required to ensure high-quality welds. Inadequate clearance can affect weld quality and efficiency, leading to increased costs and delayed schedules. In extreme cases, obstructions may cause a lack of fusion between the base metal and the weld metal, causing a reduction in strength.

Welder and Equipment Access

The area near the weld must be clear, with enough room for equipment and welder access. For this purpose, Shaw (1996) recommended "at least 18 in. of clear space around the joint." This clearance should be maintained until the inspection has been completed. For field welding, erectors can provide project-specific clearance requirements based on their personnel and equipment.

Electrode Positioning Clearance

In addition to welder and equipment access, clearance must also be provided for electrode positioning. For proper fusion and penetration, the welder must be able to direct the arc against the base metal. When an obstruction is present, the electrode is forced into a nonoptimal position, potentially causing lower penetration and difficulty achieving the correct weld profile.

Fillet Welding Near Obstructions

The recommended electrode clearance for shielded metal arc welding (SMAW) welding is shown in Figure 8-11 of the 15th Edition *Steel Construction Manual* (AISC, 2017), which is reproduced here as Figure 1. For horizontal welds, the AISC *Manual* recommends a 30° electrode angle, with an absolute minimum angle of 27° (based on a 2-to-1 slope). These recommendations were first included in the AISC publication, *Structural Shop Drafting* (AISC, 1953), with the additional comment that "the root of the weld shall be visible to the operator." Similar clearances were proposed by Priest (1943) and Grover (1946) more than seven decades ago, when SMAW was the prevalent welding process for steel structures.

A special condition is shown in AISC *Manual* Figure 8-12 (shown here as Figure 2), where weld access is available at the member end. In this case, the clearance is independent of the flange width, and the angle between the electrode and

Bo Dowswell, P.E., Ph.D., Principal, ARC International, LLC, Birmingham, AL. Email: bo@arcstructural.com

the longitudinal weld axis is critical. For further information, see Part 8 of the AISC *Manual*, where a 20° minimum electrode angle is recommended for straight electrodes.

An additional parameter that may affect weld clearance requirements is the "banking" of weld metal to counteract the effect of gravity for welds made in the horizontal position. To obtain equal-leg fillet welds, the welder typically rotates the electrode toward the horizontal surface so the arc is directed more toward the vertical surface. Based on this, a vertical obstruction may be more critical than a horizontal obstruction in the welding of joints in the horizontal position.
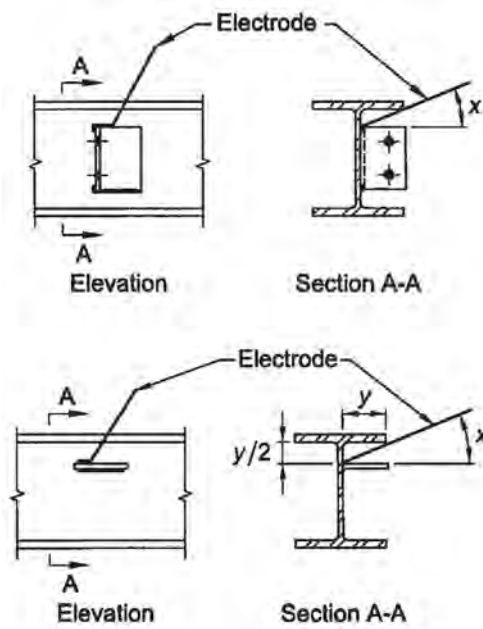
AISC Design Guide 21, *Welded Connections—A Primer for Engineers* (Miller, 2017), describes the different processes and where they are commonly used. Flux cored arc welding (FCAW) is the most common process for welding steel structures. Many shops now use gas-shielded flux cored arc welding (FCAW-G) or gas metal arc welding (GMAW) in production, and self-shielded flux-cored arc welding (FCAW-S) is the most used process for field welding.

As shown in Figure 3, the geometry of a FCAW or GMAW welding gun is much different from that of a SMAW "stick" electrode. Additionally, electrode manipulation techniques may be different between the processes. Therefore, the historic values previously recommended for the SMAW process may not apply to FCAW and GMAW.
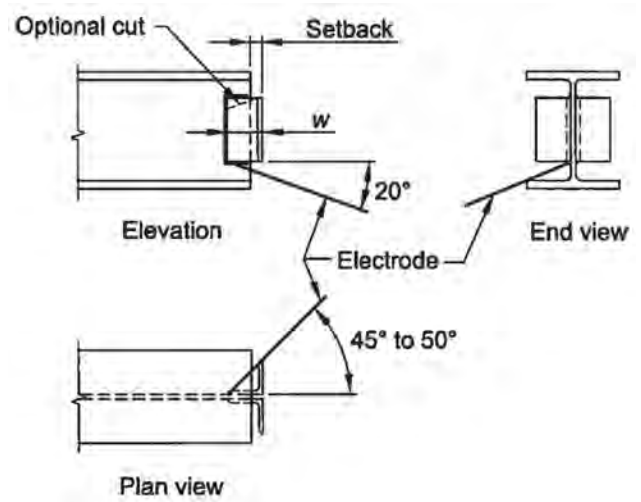

Fig. 1. Clearances for SMAW welding.

Fig. 2. Clearances for welding near the end of members.

(a)   *(b)*

Fig. 3. Fillet weld joints using the FCAW-G process: (a) unobstructed; (b) obstructed.

Groove Welds

The main function of a weld preparation is to facilitate the required weld metal penetration. The preparation must provide adequate access so the arc can be directed against the base metal. Figure 4(a) shows a T-joint with a square groove preparation that is not prequalified because the arc cannot be directed against the base metal. A similar detail is shown for a corner joint in Figure 4(b). For relatively thin materials, the corner joint is prequalified because arc access is not obstructed as it is for the T-joint. A prequalified T-joint with a single-bevel weld preparation is shown in Figure 4(c), where the arc can be easily directed against the beveled surface.

Doubler Plate Welds

AISC Design Guide 13, *Stiffening of Wide-Flange Columns at Moment Connection: Wind and Seismic Applications*

(Carter, 1999), discusses several different weld configurations for web doubler plates, including both fillet- and groove-welded joints. For the groove-welded option, a typical weld detail is shown in Figure 5, which is similar to Figures 4(a) and 4(c). Doubler plates for structures designed in accordance with the AISC *Seismic Provisions* (AISC, 2016) must be welded according to Section 4.3 of AWS D1.8 (AWS, 2016). In this case, only groove welding is allowed, and the variables defined in D1.8 must be followed.

For nonseismic design, the plate edge is often located at the tangent point of the column fillet ($R = 0$). However, detailing the joint with an encroachment onto the fillet ($R < 0$), as shown in AISC *Manual* Figure 10-3, can reduce the weld metal. In addition to the cost savings, reductions in weld metal can decrease flange rotations caused by weld shrinkage.

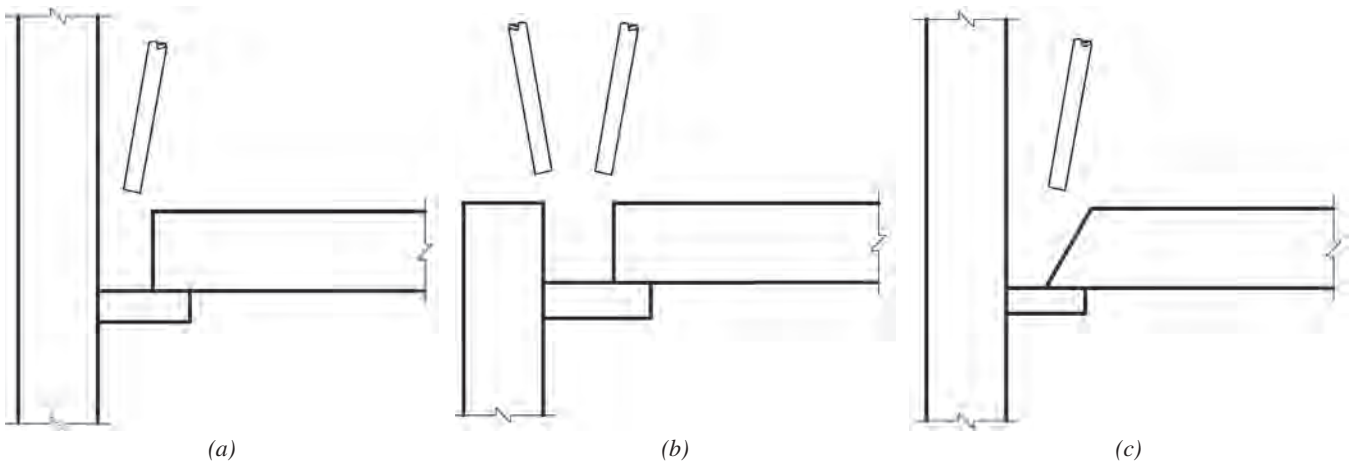For thick doubler plates, a groove angle, α, of 30° is common, but angles as low as 15° have been used successfully.

Fig. 4. Arc access: (a) not prequalified; (b) prequalified for limited thickness; (c) prequalified for unlimited thickness.
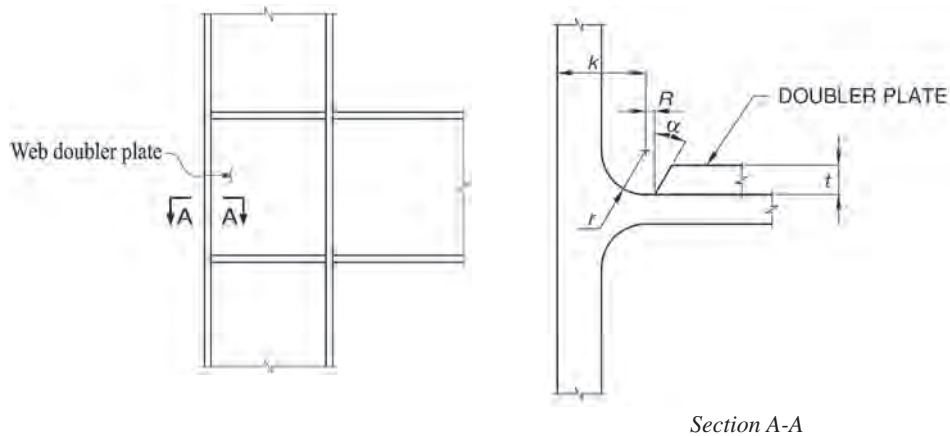

Section A-A

Fig. 5. Doubler plate groove welds.

For thin doubler plates, square-cut plates (α = 0°) are often used to eliminate the plate preparation and reduce the weld metal volume. Square-cut preparations must be limited to thin plates because proper fusion between the weld metal and the doubler plate is attained by weld penetration into the doubler plate, essentially melting the plate corner and creating a groove angle as the weld progresses. Current fabrication practices vary, but generally, plates less than 3/8 in. thick are cut square and plates 3/8 in. and thicker are beveled; however, the author is not aware of any published recommendations for this detail.

OBJECTIVES

The objective of this research is to determine practical limits on connection geometry for welding joints with limited access. Two weld clearance issues are addressed:

1. *Fillet welding near obstructions.* The obstructed fillet weld specimens were used to determine the minimum clearance requirements for joints welded with the FCAW process.

2. *Doubler plate welds.* The doubler plate specimens were used to provide information regarding the root-pass penetration for square-cut plates based on the plate thickness and the distance from the inner surface of the flange to the edge of the plate. These specimens were also used to determine the effect of joint geometric constraints on the fusion into the doubler plate edge.
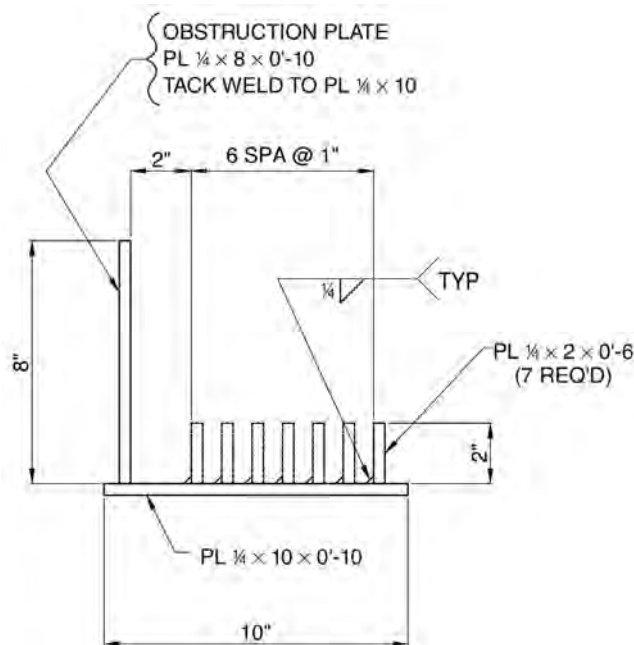

Fig. 6. Weld clearance specimen detail.

PROCEDURE

To determine the effect of clearance on the quality of welded joints, specimens were fabricated, sectioned and inspected. All specimens were fabricated by AISC-certified fabricators using the FCAW-G process. Because the equipment for GMAW is similar to that of FCAW-G, the clearance requirements are similar. Due to the absence of a gas nozzle, less clearance is required for the FCAW-S process. Each shop selected a welder to participate in the project based on an average level of skill and experience. Each weld was visually inspected by the fabricator, and any deficiencies were noted. The selected welders completed a questionnaire, and the engineering/production managers were interviewed for further information. All specimens were sectioned by cold-sawing at two locations perpendicular to the weld. The saw-cut sections were macro-etched with a 10% Nital etchant, which consists of 10 ml nitric acid and 90 ml ethyl alcohol. Etching reveals the grain structure, allowing the boundaries of the weld metal, base metal, and heat affected zone to be identified. Further information on the procedures is provided in the sections, "Fillet Welding Near Obstructions" and "Doubler Plate Welds." The welding procedure specifications for each participating fabricator are listed in Appendix A.

FILLET WELDING NEAR OBSTRUCTIONS

This part of the project studied clearance requirements by sectioning specimens that were welded at various distances from an obstruction plate. Three fabricators each welded specimens in three different positions for a total of nine specimens.

Procedure

The weld clearance specimens used a 1/4- × 8-in. plate to simulate an obstruction. Each specimen was fabricated with seven test welds, as shown in Figure 6. The outermost 1/4- × 2-in. plate was welded first, and the assembly sequence progressed toward the obstruction plate. Figure 7 shows the weld sequences, labeled location 1 through location 7, with location 7 closest to the obstruction plate.

One large fabricator and two medium-size fabricators participated in this part the project. Each fabricator supplied three specimens, with two specimens welded in the horizontal position and one specimen welded in the vertical position. For the specimens welded in the horizontal position, position A was oriented with the obstruction plate in the vertical direction, and position B had the obstruction plate in the horizontal direction as shown in Figures 8(a) and 8(b), respectively. A specimen welded in the vertical-position, designated position C, is shown in Figure 8(c).

Each specimen was identified with the designation,

FPC-L, where F is the fabricator number, P is the welding position, C designates the cross-sectional cut location along the weld length, and L is the weld location number. After sectioning and etching the specimens, the weld leg sizes and effective throat dimensions were measured from a digital image in AutoCAD software.

RESULTS

Representative samples of the sectioned fillet weld specimens for each welding position are shown in Figure 9. The digitally measured weld leg sizes and effective throat dimensions are listed in Table B-1 of Appendix B. The measured dimensions, shown in Figure 7, are the effective throat, E, and the fillet weld leg sizes, w_1 and w_2.

As indicated in Table B-1, several of the weld leg measurements are less than the specified size of ¼ in. However, these welds passed the fabricator's visual inspection and meet the visual inspection acceptance criteria requirements of AWS D1.1 (AWS, 2015) Table 6.1, which allows a minimum size of ¼ in. – ³⁄₃₂ in. = 0.156 in. over 10% of the weld
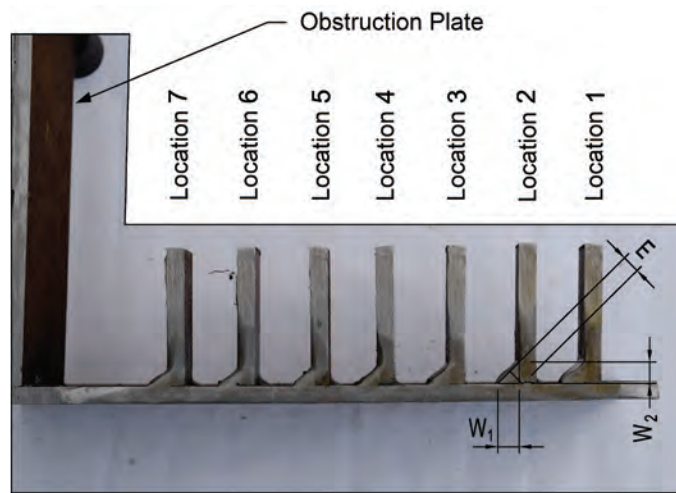

Fig 7. Section of a completed weld clearance specimen.

(a)   *(b)*   *(c)*

Fig. 8. Specimen positions: (a) position A; (b) position B; (c) position C.

(a) Location 3

(b) Location 7

Position A

(c) Location 1

(d) Location 7

Position B

(e) Location 5

(f) Location 7

Position C

Fig. 9. Fillet weld specimens.

length. Based on the specified leg size, the theoretical effective throat is:

$$E_t = \frac{\frac{1}{4} \text{ in.}}{\sqrt{2}} = 0.177 \text{ in.}$$

Specimen 1B2-3 is the only weld with a measured effective throat less than 0.177 in. At this section, the measured dimension is only 4% less than the theoretical value. A reduction in the effective throat at this location could be predicted by evaluating the slightly undersized leg 1. Because leg 1 was undersized over less than 10% of the weld length, the slightly undersized effective throat can be considered within tolerance.

The welds for specimens 1A1-1, 1A1-2, 1A2-1, 1A2-2, 1B1-1, 1B1-2, 1B2-1 and 1B2-2 were rejected by the inspector without repair. The rejected welds were in positions 1 and 2, which were farthest from the obstruction plate. Several of the rejected specimens have undersized weld legs; however, the effective throat dimensions for these specimens are greater than the theoretical values.

As the distance between the weld and the obstruction plate decreases, the electrode angle changes, causing the arc to be increasingly directed toward the $\frac{1}{4}$- × 10-in. plate and away from the $\frac{1}{4}$- × 2-in. plates. This causes an increase in the leg aspect ratio, w_1/w_2, and a decrease in the penetration into the base metal at leg 2. The leg aspect ratios for each specimen are listed in Table A-1. The mean values for all specimens are plotted in Figure 10, which shows approximately equal leg sizes for locations 1 through 5. For locations 6 and 7, the mean value for w_1 is approximately 15 to 20% greater than w_2. This effect is clearly demonstrated in Figures 11(a), 11(b) and 11(c), which were welded in position C at locations 5, 6 and 7, respectively. In this case, the aspect ratios for locations 5, 6 and 7 are 1.20, 1.25 and 1.70, respectively.

Generally, all welds showed good fusion at both plates;

however, the penetration depth at the $\frac{1}{4}$- × 2-in. plates (leg 2) decreased as the distance between the weld and the obstruction plate decreased. The specimen in Figure 9(c), at location 1, showed normal root penetration. For the weld closest to the obstruction plate, Figure 9(d) shows less penetration at leg 2.

A measure of the efficiency reduction is the area ratio, A_m/A_t, where A_m is the weld metal area calculated with the measured leg sizes and A_t is the theoretical weld metal area calculated with the specified leg size. The area ratios for each specimen are listed in Table A-1. And the mean values for all specimens are plotted in Figure 12. At location 1, A_m is approximately 20% more than A_t. As the distance between the weld and the obstruction plate decreases the area ratio shows an upward trend to a maximum mean value of 1.33 at location 5.

One of the welders reported no problems except that the angle of the welding gun was restricted for welding in the
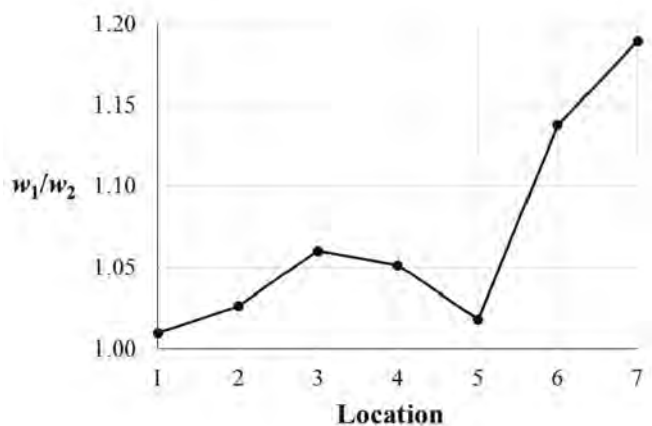

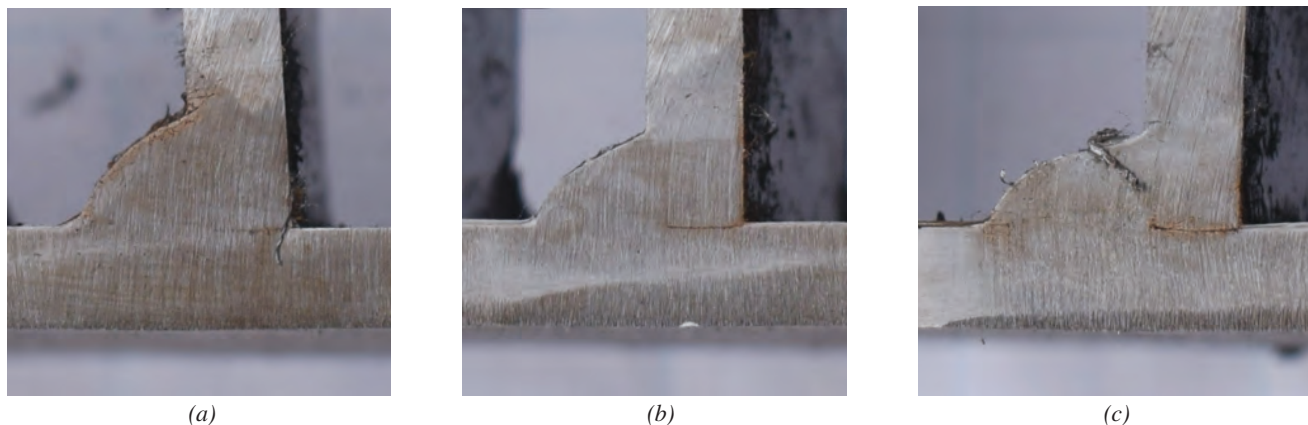Fig. 10. Mean leg aspect ratio, w_1/w_2, for each weld location.

Fig. 11. Fillet weld specimens—position C: (a) location 5; (b) location 6; (c) location 7.

vertical position at location 7. This affected the weld leg ratio and the production efficiency. The welder for another fabricator noted that, for all three welding positions, weld quality and production efficiency was affected only for welds at locations 6 and 7. Although the production efficiency was perceived to be the primary issue, the welder also expressed concerns regarding the potential effects on the weld fusion and penetration.

Conclusions

The cross-sectioned welds showed that as the distance between the weld and the obstruction plate decreased, both the production efficiency and the penetration into the base metal parallel to the obstruction plate (at leg 2) decreased. Another issue at location 7, where the welds are 2 in. from the obstruction plate, is the limited access for measuring the weld size with a standard gage. Although the penetration at leg 2 was generally low at location 6, where the welds are 3 in. from the obstruction plate, the measured effective throats exceeded the nominal values. This is because the decrease in penetration was compensated by an increase in weld metal. In interviews, welders expressed concerns regarding the potential effects of the obstruction on the weld fusion and penetration at locations 6 and 7, which may have caused them to increase the weld metal deposited.

Recommendations

Suggested clearances for FCAW and GMAW fillet welds are shown in Figure 13. The minimum values correspond to clearances required to maintain the expected weld strength based on proper fusion and weld throat size. The recommended values provide enough clearance to ensure normal production efficiency. Two joint geometries are considered: case 1, where the welded element is parallel to the obstruction, and case 2, where the welded element is perpendicular to the obstruction.
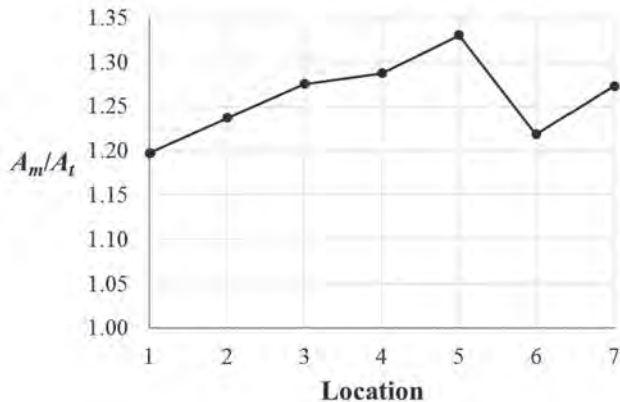
- Case 1: When welding near wide obstructions (large b-dimension), the welder's hand and the welding gun must fit into the opening while allowing enough room for proper electrode manipulation. For this geometry, the required clearance, c_{min}, is the minimum of $b/2$ and 4 in. This should be considered the absolute minimum clearance. As with the SMAW process, a 30° electrode angle is recommended for optimum production efficiency, resulting in the $0.6b$ clearance recommendation.

- Case 2: This configuration does not require the entire welding gun to fit within the clearance dimension, allowing less restrictive clearances. Due to the high heat input with the FCAW and GMAW processes and the increased access between the gas nozzle and the weld surface, c_{min} is dependent on the plate thickness, t. If these requirements cannot be met, the plate edge can be beveled as shown in Figure 5, with a fillet weld placed along the skewed edge. Some of the recommendations for case 2 are based on the results discussed in the section of this paper on doubler plate welds.

DOUBLER PLATE WELDS

Eight simulated doubler plate specimens were sectioned to evaluate the effect of various geometric parameters on the root-pass penetration for square-cut doubler plates. The specimen variables were the plate thicknesses and the distance from the inner surface of the flange to the edge of the plate.

Recommended:

$c_{min} = \min(0.6b, 5 \text{ in.})$

Minimum:

$c_{min} = \min(b/2, 4 \text{ in.})$

$t \leq \frac{5}{16}$ in.:

$c_{min} = \frac{3}{4}$ in.

$\frac{5}{16}$ in. $< t \leq \frac{5}{8}$ in.:

$c_{min} = \min(b/2, 2 \text{ in.})$

$\frac{5}{8}$ in. $< t$:

Recommended:

$c_{min} = \min(b/2, 3\frac{1}{2} \text{ in.})$

Minimum:

$c_{min} = \min(b/2, 2\frac{1}{2} \text{ in.})$

(a)   *(b)*

Fig. 13. Recommended clearances for FCAW and GMAW fillet welds: (a) case 1; (b) case 2.

Fig. 12. Mean area ratio, A_m/A_t, for each weld location.

Procedure

Eight simulated doubler plate specimens were supplied by a single fabricator. As shown in Figure 14, drop material from a recent project was used for the W-shape, with extension tabs tack-welded to the flange tips to produce the dimensions of a W14×90 column. The specimens are 9 in. long. The root pass was welded in the horizontal position, which is the same as the flat position for the completed groove weld. The simulated doubler plate was square cut ($\alpha = 0°$) with the variable dimensions shown in Figure 15. The distance from the inner surface of the flange to the edge

(a)

(b)

Fig. 14. Doubler plate specimens: (a) ¾-in. specimen; (b) ¼-in. specimen.

of the plate, x, was either ⅝ in. or 1¼ in., and four different plate thicknesses were used: ¼, ⅜, ½ and ¾ in. Because the concerns are associated with proper fusion at the plate edge and penetration at the root pass, only the first pass was completed, and the remaining passes required to complete the joint were omitted.

Results

Representative samples of the etched sections are shown in Figures 16, 17, 18 and 19 for the specimens with ¼-, ⅜-,

½- and ¾-in. doubler plate thicknesses, respectively. As shown in Figure 16, all sections with a ¼-in. doubler plate showed good fusion and penetration into both the column and the plate. The heat input from welding melted the plate edge, creating adequate access for the welder to direct the arc toward the base metal.

The welding heat did not have the same effect on the thicker specimens. Many of the ⅜-, ½- and ¾-in. specimens had adequate fusion and significant penetration, as shown for the ⅜-in. doubler plate specimen shown in Figure 17(b)
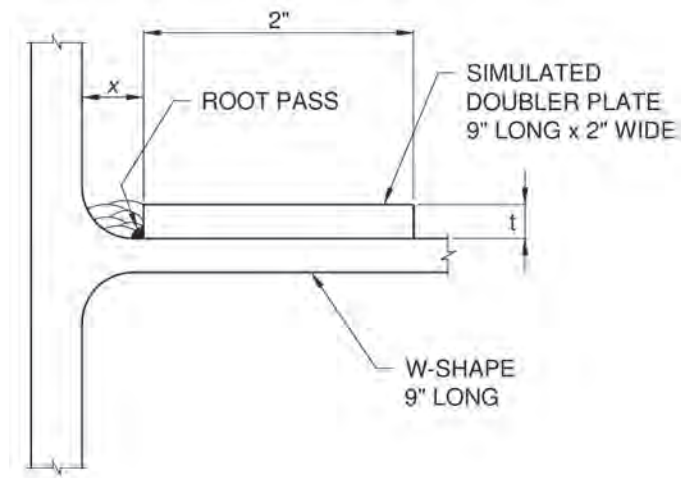
Fig. 15. Doubler plate specimen dimensions.

| (a) | (b) |

Fig. 16. ¼-in. doubler plate specimen: (a) x = 1¼ in.; (b) x = ⅝ in.

and the ¾-in. doubler plate specimen shown in Figure 19(a). However, the specimens in Figures 17(c), 18(b), 19(b) and 19(c) had a lack of root penetration, and the specimens in Figures 18(c) and 19(b) had a low penetration depth at the doubler plate. Although these problems were more prevalent for the specimens with $x = ⅝$ in., they were also present for the specimens with $x = 1¼$ in.

Conclusions

Adequate fusion and penetration can be consistently obtained for ¼-in. square-cut ($\alpha = 0°$) doubler plates welded with the FCAW process. However, portions of the weld at some of the thicker (⅜, ½ and ¾ in.) plates showed a lack of root penetration. Because proper electrode positioning is

(a)

(b)

(c)

Fig. 17. ⅜-in. doubler plate specimens: (a) x = 1¼ in.; (b) x = ⅝ in.; (c) x = ⅝ in.

Fig. 18. ½-in. doubler plate specimens: (a) x = 1¼ in.; *(b)* x = 1¼ in.; *(c)* x = ⅝ in.

Fig. 19. ¾-in. doubler plate specimens: (a) x = 1¼ in.; *(b)* x = ⅝ in.; *(c)* x = ⅝ in.

gained by melting the edge of the thinner plates, varying the root opening, R (Figure 5), had no observable effect on the weld quality.

Recommendations

Based on the results of this study, which was limited to only eight specimens, the common practice of cutting the edge square ($\alpha = 0°$) at doubler plates less than 3/8 in. thick has been validated. Because the root opening, R, had no observable effect on the weld quality, $R \leq 0$ is recommended for doubler plates less than 3/8 in. thick.

For doubler plates thicker than 1/4 in., a beveled edge preparation with a groove angle, α, of 15° to 30° may be required to ensure consistent weld quality. Based on the results of the 1/4-in. doubler plate specimens, it is expected that a 1/4-in. root face could be used for these joints to reduce the weld metal while maintaining weld quality. It is believed that $R \leq 0$ will be acceptable for this condition.

CONCLUSIONS

Inadequate clearance can affect weld quality and efficiency. In extreme cases, obstructions may cause a lack of fusion between the base metal and the weld metal, causing a reduction in strength. Although FCAW and GMAW have replaced SMAW as the primary fabrication processes for structural steel fabrication, existing clearance recommendations are based on the SMAW process. Because the geometry of a FCAW or GMAW welding gun is much different from that of a SMAW "stick" electrode and because electrode manipulation techniques may be different between the processes, the historic values recommended for the SMAW process may not apply to FCAW and GMAW.

Experimental specimens were fabricated with the FCAW process to determine practical limits on connection geometry for welding joints with limited access. Each specimen was evaluated by sectioning and etching the weld at two locations along the length. Two weld clearance issues are addressed: (1) fillet welding near obstructions and (2) doubler plate welds.

The obstructed fillet weld specimens were used to determine clearance requirements for joints welded with the FCAW process. This part of the project studied clearance requirements by evaluating specimens that were welded at various distances from an obstruction plate. The cross-sectioned welds showed that as the distance between the weld and the obstruction plate decreased, both the production efficiency and the penetration into the base metal decreased. Revised clearance recommendations for FCAW and GMAW welding were proposed for two joint geometries: case 1, where the welded element is parallel to the obstruction, and case 2, where the welded element is perpendicular to the obstruction. These suggested clearances are shown in Figure 13.

The doubler plate specimens were used to evaluate the effect of various geometric parameters on the root-pass penetration for square-cut doubler plates. The specimen variables were the plate thicknesses and the distance from the inner surface of the flange to the edge of the plate. Based on the results of this study, which was limited to only eight specimens, the common practice of cutting the edge square ($\alpha = 0°$) at doubler plates less than 3/8 in. thick has been validated. Because the root opening, R, had no observable effect on the weld quality, $R \leq 0$ is recommended for doubler plates less than 3/8 in. thick. For doubler plates thicker than 1/4 in., a groove angle, α, of 15° to 30° may be required to ensure consistent weld quality. It is expected that a 1/4-in. root face could be used for these joints to reduce the weld metal while maintaining weld quality.

REFERENCES

AISC (1953), *Structural Shop Drafting*, Vol. 2, American Institute of Steel Construction, Chicago, IL.

AISC (2016), *Seismic Provisions for Structural Steel Buildings*, ANSI/AISC 341-16, American Institute of Steel Construction, Chicago, Illinois.

AISC (2017), *Steel Construction Manual*, 15th Ed., American Institute of Steel Construction, Chicago, IL.

AWS (2015), *Structural Welding Code-Steel*, AWS D1.1:2015, American Welding Society, Miami, FL.

AWS (2016), *Structural Welding Code-Seismic Supplement*, AWS D1.8/D1.8M, American Welding Society, Miami, FL.

Carter, C.J. (1999), *Stiffening of Wide-Flange Columns at Moment Connections: Wind and Seismic Applications*, Design Guide 13, AISC, Chicago, IL.

Grover, L. (1946), *Manual of Design for Arc Welded Steel Structures*, 1st Ed., Air Reduction Sales Co., New York, NY.

Miller, D.K. (2017), *Welded Connections—A Primer for Engineers*, Design Guide 21, 2nd Ed., AISC, Chicago, IL.

Priest, H.M. (1943), "The Practical Design of Welded Steel Structures," *Journal of the American Welding Society*, Vol. 22, No. 9 (September), pp. 677–695.

Shaw, R. (1996), Seminar Notes, "Structural Welding: Design and Specification," Steel Structures Technology Center, Howell, MI.

APPENDIX A
## WELDING PROCEDURE SPECIFICATIONS

Fabricator 1

AWS - Prequalified Welding Procedure Specification (pWPS)

Identification #

Company name			Originated by	
Welding process	FCAW		Date	
Process type	Semi-automatic		Authorized by	
			Date	

Position

Joint design used				
Joint type	TC - T or corner joint		Welding position:	Groove All
Joint design	Single bevel groove (4)			Fillet All
Backing	Yes		Vertical progression	Up
Backing material	Steel		**Electrical characteristics**	
Root opening (R)*	(in.) 1/4, +1/16, -0 (+1/4, 1/16)		Transfer mode (GMAW)	Spray
Root face (f)*	(in.) n/a		Current type	DCEP
Groove angle (a)*	(deg.) 45, +10, -0 (+10, -5)		Other	Constant Voltage (CV) power supply
Radius (J - U)*	(deg.) n/a		**Technique**	
Back gouging	No		Stringer or weave bead	Stringer or Weave
Back gouging method	n/a		Multi/single pass (per side)	Single or Multiple

* Datum: As Detailed (As Fit-Up)

Base metals			Number of electrodes	Single electrode
Spec., type or grade	AWS D1.1 Table 3.1 Group II		Spacing: Longitudinal	(in.) -
Thickness: Groove	(in.) T1:unlimited T2:unlimited		Lateral	(in.) -
Fillet	(in.) All		Angle	(deg.) -
Diameter (Pipe)	(in.) Unlimited		Contact tube to work	(in.) 0.5 - 1
Filler metals			Peening	Not permitted
AWS Specification	5.20		Interpass cleaning	Brushing or grinding
AWS Classification	E71T-1C-H8		**Preheat**	
Shielding			Preheat temp.: Min.	(°F) See notes
Flux	-		Interpass temp.: Min.	(°F) See notes
Electrode-flux (class)	-		Max.	(°F) See notes
Gas composition	CO2 (A5.32 SG-C)		**Post weld heat treatment**	
Gas flow rate	(cfh) 25-45		Temperature	(°F) None
Gas cup size	(in.) 1/2-3/4		Time	(hrs) -

Welding procedure

Layer	Pass	Process	Filler metal class	Filler metal diameter (in.)	Current type / polarity	Amps	Wire feed speed (in./min)	Volts	Travel speed (in./min)	Joint details
1	All	FCAW	E71T-1C-H8	0.045	DCEP	150-290	200-500	24-29	6-15	
1	All	FCAW	E71T-1C-H8	0.052	DCEP	165-300	200-500	25-29	6-15	

Designation   TC-U4a-GF
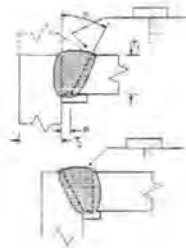
Notes

PREHEAT/INTERPASS
For thickness 1/8 to 3/4(in.): 32(°F). Preheat to 70(°F) if the base metal temperature is below 32(°F).
Over 3/4 thru 1-1/2(in.): 150(°F).
Over 1-1/2 thru 2-1/2(in.): 225(°F).
Over 2-1/2(in.): 300(°F).
See additional information page for further limitations

Signature 1		Signature 2	
Name		Name	Signature
Date		Date	
Signature 3		Signature 4	
Name	Signature	Name	Signature
Date		Date	
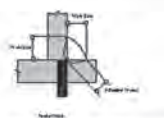
WPS No.	FCAW-1F	Revision	10	Date 9/12/14	By

Authorized By _____ Date 10/20/1998 Prequalified ☒

Welding Process(es) FCAW _____ Type: Manual ☐ Machine ☐ Semi-Auto ☒ Auto ☐

Supporting PQR(s) N/A

JOINT

Type T-Joint

Backing Yes ☐ No ☒ Single Weld ☒ Double Weld ☒

Backing Material N/A

Root Opening See Note 5 Root Face Dimension N/A

Groove Angle 90 Radius (J-U) N/A

Back Gouge Yes ☐ No ☒

Method N/A

BASE METALS

Material Spec. AWS Grp I or II to AWS Grp I or II

Type or Grade AWS Grp I or II to AWS Grp I or II

Thickness: Groove ( ) _____ - _____

Fillet ( )Unlimited - Unlimited

Diameter (Pipe,) 1" - Unlimited

FILLER METALS

AWS Specification A5.20

AWS Classification E71-T1or E71-T5

SHIELDING

Flux	Gas CO2
N/A	Composition 100%
Electrode-Flux (Class)	Flow Rate 35-45 CFH
N/A	Gas Cup Size 1/2 to 3/4 in.

PREHEAT

Preheat Temp., Min. See Note 2

Thickness	Up to 3/4"	Temperature	32
	Over 3/4" to 1-1/2"		50
	Over 1-1/2" to 2-1/2"		150
	Over 2-1/2"		225

Interpass Temp., Min. See Note 3 Max. 400

POSITION

Position of Groove Flat Fillet ALL

Vertical Progression: ☒ Up ☐ Down

ELECTRICAL CHARACTERISTICS

Transfer Mode (GMAW):

Short-Circuiting ☐ Globular ☒ Spray ☐

Current: AC ☐ DCEP ☒ DCEN ☐ Pulsed ☐

Other Constant Voltage

Tungsten Electrode (GTAW):

Size N/A Type N/A

TECHNIQUE

Stringer or Weave Bead Both

Multi-pass or Single Pass (per side) Both

Number of Electrodes 1

Electrode Spacing: Longitudinal N/A

Lateral N/A

Angle N/A

Contact Tube to Work Distance 1/2 to 3/4

Peening Not Allowed

Interpass Cleaning Brushing or Grinding

POSTWELD HEAT TREATMENT PWHT Required ☐

Temp. N/A Time N/A

WELDING PROCEDURE

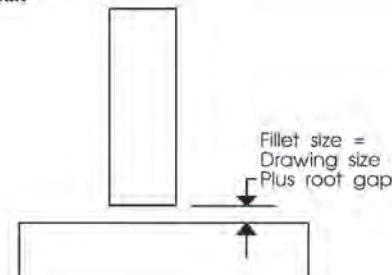| Layer/Pass	Process	Filler Metal Class	Diameter	Cur. Type	Amps or WFS	Volts	Travel Speed	Other Notes
1 - OUT	FCAW	E71-T1orE71-T5	.045	DCEP	165 - 270	24 - 32	15 - 21 ipm	
1 - OUT	FCAW	E71-T1orE71-T5	.052	DCEP	220 - 405	25 - 35	20 - 30 ipm	
1 - OUT	FCAW	E71-T1orE71-T5	1/16 in	DCEP	300 - 500	28 - 36	20 - 30 ipm	

Fabricator 3

AWS D1.1 Prequalified Welding Procedure Specification (WPS)

WPS No. **TFillet**   Date **5/18/2015**   Rev. No. **0**   Page 1 of 2

Prepared By: _____   Date **5/18/2015**

Welding Process(es)/Type(s) **FCAW/Semiautomatic**

Joint Design Used	Joint Detail
Weld Type Fillet welds	
Fillet Type T-joint	
Double Welded No	
Backing Yes Material Base Metal	
Root Opening 3/16 in. Root Face N/A	
Groove Angle N/A Radius N/A	Fillet size = Drawing size Plus root gap
Back Gouging No Method N/A	

Base Metals
Base Metal ASTM A 572, Grade 50
Thickness: Groove N/A
Thickness: Fillet 1/8 in. min.
Pipe Diameter 3/8 in. min.

Groups I & II

Position
Weld Position: Fillet All Positions
Weld Position: Groove N/A
Vertical Progression Vertical up
5/16

Filler Metals
AWS Specification 5.20
AWS Classification E71T-1
Weld Size 5/16 in.

Shielding
Gas 100% CO2   Flow Rate 32-60 CFH
Gas Cup Size 5/8-3/4
Electrode-Flux (Class) N/A
Flux Trade Name N/A

Electrical Characteristics
Power Source
Output Constant Voltage
Current / Polarity DCEP (reverse)
Transfer Mode Globular arc
Tungsten Electrode: Type N/A
Tungsten Electrode: Size N/A

Preheat
Preheat Temperature, Min. 32°F
Interpass Temperature, Min. 32°F   Max. 500°F

Minimum Preheat and Interpass Temperatures for given thickness:
    1/8" thru 3/4" incl.: 32°F (70°F if less than 32°F)
Over 3/4" thru 1-1/2" incl.: 50°F
Over 1-1/2" thru 2-1/2" incl.: 150°F
            Over 2-1/2": 225°F

Technique
Stringer or Weave Bead Stringer or weave bead
Multi/Single Pass Single or multipass
Number of Electrodes 1
Electrode Spacing: Longitudinal N/A
    Lateral N/A   Angle N/A
Contact Tube to Work Distance 3/8 to 3/4
Peening Not allowed.
Interpass Cleaning Chipping hammer, wire brush and grind as
                needed.

Postweld Heat Treatment
Temperature None
Time (hr.) None

Welding Procedure

Pass or Weld Layer(s)	Process	Filler Metal AWS Classification	Size (in.)	Current Type & Polarity	Amps	Volts	Travel Speed (in/min)
ALL	FCAW	E71T-1	0.052	DCEP (reverse)	220 - 270	26-30	12 - 20
ALL	FCAW	E71T-1	0.045	DCEP (reverse)	200 - 240	25-28	9 - 15

APPENDIX B
WELDING NEAR OBSTRUCTIONS MEASURED WELD DIMENSIONS

Table B-1. Measured Specimen Dimensions

Specimen	w_1	w_2	E	w_1/w_2	A_m	A_m/A_t	Specimen	w_1	w_2	E	w_1/w_2	A_m	A_m/A_t
1A1-1	0.33	0.31	0.23	1.06	0.051	1.64	1C2-1	0.20	0.23	0.19	0.87	0.023	0.74
1A1-2	0.30	0.31	0.25	0.97	0.047	1.49	1C2-2	0.22	0.25	0.19	0.88	0.028	0.88
1A1-3	0.29	0.28	0.21	1.04	0.041	1.30	1C2-3	0.24	0.21	0.19	1.14	0.025	0.81
1A1-4	0.25	0.23	0.19	1.09	0.029	0.92	1C2-4	0.21	0.23	0.20	0.91	0.024	0.77
1A1-5	0.24	0.27	0.21	0.89	0.032	1.04	1C2-5	0.27	0.28	0.22	0.96	0.038	1.21
1A1-6	0.26	0.24	0.20	1.08	0.031	1.00	1C2-6	0.25	0.25	0.22	1.00	0.031	1.00
1A1-7	0.29	0.24	0.20	1.21	0.035	1.11	1C2-7	0.25	0.21	0.19	1.19	0.026	0.84
1A2-1	0.26	0.27	0.21	0.96	0.035	1.12	2A1-1	0.29	0.28	0.20	1.04	0.041	1.30
1A2-2	0.26	0.31	0.22	0.84	0.040	1.29	2A1-2	0.27	0.30	0.22	0.90	0.041	1.30
1A2-3	0.28	0.24	0.20	1.17	0.034	1.08	2A1-3	0.27	0.30	0.21	0.90	0.041	1.30
1A2-4	0.29	0.30	0.23	0.97	0.044	1.39	2A1-4	0.29	0.32	0.21	0.91	0.046	1.48
1A2-5	0.28	0.26	0.22	1.08	0.036	1.16	2A1-5	0.29	0.32	0.21	0.91	0.046	1.48
1A2-6	0.27	0.24	0.20	1.13	0.032	1.04	2A1-6	0.25	0.29	0.19	0.86	0.036	1.16
1A2-7	0.30	0.28	0.25	1.07	0.042	1.34	2A1-7	0.29	0.25	0.21	1.16	0.036	1.16
1B1-1	0.20	0.26	0.19	0.77	0.026	0.83	2A2-1	0.25	0.27	0.18	0.93	0.034	1.08
1B1-2	0.20	0.30	0.20	0.67	0.030	0.96	2A2-2	0.24	0.27	0.20	0.89	0.032	1.04
1B1-3	0.28	0.27	0.20	1.04	0.038	1.21	2A2-3	0.28	0.30	0.20	0.93	0.042	1.34
1B1-4	0.24	0.26	0.20	0.92	0.031	1.00	2A2-4	0.27	0.30	0.20	0.90	0.041	1.30
1B1-5	0.24	0.30	0.20	0.80	0.036	1.15	2A2-5	0.26	0.29	0.20	0.90	0.038	1.21
1B1-6	0.26	0.29	0.21	0.90	0.038	1.21	2A2-6	0.28	0.30	0.21	0.93	0.042	1.34
1B1-7	0.27	0.25	0.21	1.08	0.034	1.08	2A2-7	0.27	0.24	0.18	1.13	0.032	1.04
1B2-1	0.21	0.24	0.19	0.88	0.025	0.81	2B1-1	0.28	0.28	0.22	1.00	0.039	1.25
1B2-2	0.21	0.26	0.21	0.81	0.027	0.87	2B1-2	0.33	0.28	0.21	1.18	0.046	1.48
1B2-3	0.24	0.25	0.17	0.96	0.030	0.96	2B1-3	0.34	0.31	0.23	1.10	0.053	1.69
1B2-4	0.27	0.24	0.18	1.13	0.032	1.04	2B1-4	0.38	0.26	0.21	1.46	0.049	1.58
1B2-5	0.25	0.27	0.20	0.93	0.034	1.08	2B1-5	0.34	0.28	0.23	1.21	0.048	1.52
1B2-6	0.26	0.25	0.18	1.04	0.033	1.04	2B1-6	0.34	0.23	0.20	1.48	0.039	1.25
1B2-7	0.24	0.22	0.18	1.09	0.026	0.84	2B1-7	0.33	0.29	0.23	1.14	0.048	1.53
1C1-1	0.26	0.29	0.21	0.90	0.038	1.21	2B2-1	0.28	0.27	0.21	1.04	0.038	1.21
1C1-2	0.25	0.23	0.21	1.09	0.029	0.92	2B2-2	0.31	0.25	0.22	1.24	0.039	1.24
1C1-3	0.27	0.24	0.21	1.13	0.032	1.04	2B2-3	0.34	0.27	0.23	1.26	0.046	1.47
1C1-4	0.24	0.28	0.22	0.86	0.034	1.08	2B2-4	0.38	0.27	0.22	1.41	0.051	1.64
1C1-5	0.27	0.23	0.21	1.17	0.031	0.99	2B2-5	0.32	0.26	0.21	1.23	0.042	1.33
1C1-6	0.23	0.25	0.23	0.92	0.029	0.92	2B2-6	0.35	0.21	0.19	1.67	0.037	1.18
1C1-7	0.26	0.22	0.21	1.18	0.029	0.92	2B2-7	0.34	0.28	0.23	1.21	0.048	1.52

Specimen	w_1	w_2	E	w_1/w_2	A_m	A_m/A_t	Specimen	w_1	w_2	E	w_1/w_2	A_m	A_m/A_t
2C1-1	0.24	0.32	0.22	0.75	0.038	1.23	3B1-1	0.34	0.30	0.25	1.13	0.051	1.63
2C1-2	0.25	0.26	0.23	0.96	0.033	1.04	3B1-2	0.30	0.28	0.23	1.07	0.042	1.34
2C1-3	0.25	0.26	0.23	0.96	0.033	1.04	3B1-3	0.32	0.29	0.26	1.10	0.046	1.48
2C1-4	0.25	0.26	0.23	0.96	0.033	1.04	3B1-4	0.30	0.31	0.22	0.97	0.047	1.49
2C1-5	0.31	0.30	0.26	1.03	0.047	1.49	3B1-5	0.30	0.32	0.24	0.94	0.048	1.54
2C1-6	0.30	0.23	0.20	1.30	0.035	1.10	3B1-6	0.31	0.29	0.25	1.07	0.045	1.44
2C1-7	0.40	0.26	0.24	1.54	0.052	1.66	3B1-7	0.34	0.27	0.24	1.26	0.046	1.47
2C2-1	0.40	0.24	0.22	1.67	0.048	1.54	3B2-1	0.32	0.29	0.25	1.10	0.046	1.48
2C2-2	0.30	0.25	0.22	1.20	0.038	1.20	3B2-2	0.30	0.31	0.24	0.97	0.047	1.49
2C2-3	0.27	0.28	0.23	0.96	0.038	1.21	3B2-3	0.33	0.28	0.23	1.18	0.046	1.48
2C2-4	0.27	0.28	0.21	0.96	0.038	1.21	3B2-4	0.31	0.30	0.22	1.03	0.047	1.49
2C2-5	0.26	0.28	0.22	0.93	0.036	1.16	3B2-5	0.28	0.31	0.23	0.90	0.043	1.39
2C2-6	0.26	0.24	0.23	1.08	0.031	1.00	3B2-6	0.31	0.31	0.23	1.00	0.048	1.54
2C2-7	0.23	0.30	0.25	0.77	0.035	1.10	3B2-7	0.33	0.27	0.21	1.22	0.045	1.43
3A1-1	0.28	0.26	0.22	1.08	0.036	1.16	3C1-1	0.29	0.26	0.21	1.12	0.038	1.21
3A1-2	0.36	0.25	0.21	1.44	0.045	1.44	3C1-2	0.30	0.29	0.23	1.03	0.044	1.39
3A1-3	0.34	0.28	0.24	1.21	0.048	1.52	3C1-3	0.28	0.28	0.24	1.00	0.039	1.25
3A1-4	0.32	0.28	0.22	1.14	0.045	1.43	3C1-4	0.32	0.31	0.22	1.03	0.050	1.59
3A1-5	0.36	0.30	0.23	1.20	0.054	1.73	3C1-5	0.28	0.29	0.24	0.97	0.041	1.30
3A1-6	0.35	0.28	0.22	1.25	0.049	1.57	3C1-6	0.32	0.28	0.26	1.14	0.045	1.43
3A1-7	0.39	0.23	0.22	1.70	0.045	1.44	3C1-7	0.28	0.31	0.26	0.90	0.043	1.39
3A2-1	0.24	0.27	0.21	0.89	0.032	1.04	3C2-1	0.26	0.26	0.20	1.00	0.034	1.08
3A2-2	0.34	0.26	0.22	1.31	0.044	1.41	3C2-2	0.31	0.30	0.24	1.03	0.047	1.49
3A2-3	0.35	0.29	0.25	1.21	0.051	1.62	3C2-3	0.24	0.30	0.22	0.80	0.036	1.15
3A2-4	0.31	0.25	0.23	1.24	0.039	1.24	3C2-4	0.31	0.30	0.26	1.03	0.047	1.49
3A2-5	0.38	0.29	0.23	1.31	0.055	1.76	3C2-5	0.29	0.30	0.25	0.97	0.044	1.39
3A2-6	0.35	0.22	0.21	1.59	0.039	1.23	3C2-6	0.31	0.30	0.27	1.03	0.047	1.49
3A2-7	0.39	0.24	0.23	1.63	0.047	1.50	3C2-7	0.30	0.32	0.28	0.94	0.048	1.54

Orange-shaded cells indicate a weld that was rejected by the CWI.

Blue-shaded cells indicate that the measured dimension is less than the nominal dimension.

A_m = weld metal area calculated with the measured leg sizes, in.[2]

A_t = weld metal area calculated with the nominal specified leg size, in.[2]

E = effective throat, in.

w_1 = fillet weld leg size at the ¼- × 10-in. plate, in.

w_2 = fillet weld leg size at the ¼- × 2-in. plate, in.

Post-Buckling Mechanics of a Square Slender Steel Plate in Pure Shear

MARIA E. MOREYRA GARLOCK, SPENCER E. QUIEL, PETER Y. WANG,
JOSÉ ALÓS-MOYA and JONATHAN D. GLASSMAN

ABSTRACT

Thin (slender) steel plates possess shear strength beyond the elastic buckling load, which is commonly referred to as the post-buckling capacity. Semi-empirical equations based on experimental tests of plate girders have been used for decades to predict the ultimate post-buckling strength of slender webs. However, several recent studies have shown that the current models for predicting the ultimate shear post-buckling capacity of thin plates are based on some incorrect assumptions regarding their mechanical behavior. As a result, the current design equations provide an approximate estimate of capacity for the range of parameters in the test data upon which they are founded. This paper explores the fundamental behavior of thin plates under pure shear. Such a fundamental examination of shear post-buckling behavior in thin plates is needed to enable design procedures that can optimize a plate's shear strength and load-deformation performance for a wider range of loading and design parameters. Using finite element analyses, which are validated against available results of previous experimental tests, outputs such as plastic strains, von Mises stresses, principal stresses, and principal stress directions are examined on a buckled plate acting in pure shear. The internal bending, shear, and membrane stresses in the plate's finite elements are also evaluated. In this study, these evaluations are performed for a simply supported plate with an aspect ratio equal to 1.0 and slenderness ratio equal to 134. Results show that localized bending in the plates due to the out-of-plane post-buckling deformations appear to be a significant factor in the ultimate shear post-buckling capacity of the plate. Also, the compressive stresses continue to increase beyond the onset of elastic buckling in some regions of the plate, contrary to current design assumptions. Overall, this study provides new insights into the mechanics of shear post-buckling behavior of thin plates that can be exploited for design procedures that are consistent with mechanical behavior.

Keywords: shear, buckling, tension field, slender plates, web, plate girder.

INTRODUCTION

Deep steel beams (i.e., plate girders) have thin webs and are commonly used in steel construction for buildings but most notably in bridges. The design of these elements is often controlled by the shear strength of the slender web plate. Web plates that elastically buckle due to shear load still possess a significant amount of post-buckling shear strength. Post-buckling capacity is utilized in the design of many bridge girders due to high web slenderness, which is necessitated by large girder depths and weight/material savings. This post-buckling behavior has attracted the attention of researchers and engineers since the 1880s (e.g., Basler, 1961; Wagner, 1931; Wilson, 1886). Since 1931, more than a dozen proposals have been developed to explain and predict the post-buckling shear strength of thin webs in plate girders (e.g., Höglund, 1997; Porter et al., 1975). A detailed discussion of the differences between several of the aforementioned proposals is provided by White and Barker (2008). Despite these numerous proposals, the true mechanics and post-buckling behavior are still not fully understood, particularly the contributions of the compression field and vertical stiffeners to the ultimate post-buckling shear strength.

Previous publications have provided extensive discussions on the various proposed plate shear buckling models throughout the literature (Ziemian, 2010; White and Barker, 2008; Yoo and Lee, 2006), and all the models are based on tension field action. Tension field theory posits that the main source of this post-buckling shear strength is the development of tensile stresses in a defined diagonal field, which is mobilized after the onset of elastic shear buckling. Recent research, however, has shown that the fundamental assumptions upon which tension field action is based do not represent the full mechanical response of web shear buckling (Yoo and Lee, 2006; Glassman and Garlock, 2016; Jha, 2016).

Maria E. Moreyra Garlock, Associate Professor, Princeton University, Princeton, NJ. Email: mgarlock@princeton.edu (corresponding)

Spencer E. Quiel, Assistant Professor, Lehigh University, Bethlehem, PA. Email: seq213@lehigh.edu

Peter Y. Wang, Graduate Student, Princeton University, Princeton, NJ. Email: pywang@princeton.edu

José Alós-Moya, Ph.D., P.E., Researcher/Production Manager, UPV/ACCIONA, València, Spain. Email: joalmo11@upv.es

Jonathan D. Glassman, Ph.D., P.E., Senior Engineer, Exponent Inc., Los Angeles, CA. Email:glassman.jonathan@gmail.com

In addition, the current AISC *Specification* (2016) recognizes that the vertical stiffener does not carry the full vertical component of the tension field force. In previous editions, this stiffener was designed for an area consistent with the assumed vertical component of the tension field force, whereas it is currently designed for flexural stiffness only. This change rightly recognizes that the vertical stiffener provides lateral stiffness to define the web panelization—it does not act as an anchor for the tension field. As noted in the AISC *Specification* Commentary: "…transverse stiffeners in I-girders designed for shear post-buckling strength, including tension field action, are loaded predominantly in bending due to the restraint they provide to lateral deflection of the web. Generally, there is evidence of some axial compression in the transverse stiffeners due to the tension field, but even in the most slender web plates permitted by the AISC *Specification*, the effect of the axial compression transmitted from the post-buckled web plate is typically minor compared to the lateral loading effect. Therefore, the transverse stiffener area requirement from prior AISC *Specifications* is no longer specified" (AISC, 2016). However, the design equations that predict the post-buckling capacity are still based on the original tension field design procedures. Using the current approach, the load path for the tension field action is, therefore, incomplete—the vertical component of the diagonal tension field must be resolved via a different mechanism. The study presented in this paper provides, for the first time, insights to the behavior of thin web plates that, with more investigation, can lead to updated design recommendations that include a completed load path.

This paper explores the fundamental behavior of thin plates under pure shear. Using validated finite element analyses, outputs such as plastic strains, von Mises stresses, principal stresses, and principal stress directions are examined on the buckled plate. The through-thickness bending and membrane stresses in the plate elements are also evaluated. These evaluations are performed for a plate with an aspect ratio equal to 1.0 and slenderness ratio equal to 134. Examining this single case provides novel insights into plate

shear buckling behavior that will be used as a basis for future work, which will examine a wider range of plate parameters.

FINITE ELEMENT MODEL

The plate used for this study is based on standard plans for typical steel girder highway bridges specified by the Federal Highway Administration (FHWA, 1982). A 90-ft (27.4-m) span design was used as a prototype, where the depth, D, equals 58 in. (1473 mm) and the web thickness, t_w, equals $\frac{7}{16}$ in. (11 mm). In practice, many of these girders are designed with a transverse stiffener spacing, a, greater than D; however, in this study we assume $a = D$. Future work will examine other stiffener spacings. The steel was modeled with a yield stress equal to 50 ksi (345 MPa), a modulus of elasticity equal to 29,000 ksi (200 GPa), and Poisson's ratio equal to 0.3. It will be shown that the steel remained in the elastoplastic region for the range of strains encountered in the analyses (well before strain-hardening occurs).

The finite element (FE) model was developed in the software Abaqus (Dassault Systemes, 2011) using the simply supported boundary conditions shown in Figure 1. Note that the boundary conditions used here represent an approximation of the actual boundary conditions and may incorporate flanges and stiffeners, each of varying stiffness. To achieve perfectly symmetric stress results, the boundary conditions used by the authors differ only slightly from those used by Glassman and Garlock (2016), which restrained the *Y*-translation on the left side instead of applying a load. The elastic critical shear buckling load, V_{cr}, and the ultimate post-buckling shear load, V_u, are not affected by this slight modification in boundary condition.

Yoo and Lee (2006) used boundary conditions that were different from both configurations mentioned earlier. In their studies, the *z*-direction translation is free on all four sides. Such a boundary condition represents a lower-bound solution for V_u. The current study's boundary conditions assume axially rigid flanges and are thus closer to an upper-bound solution. All boundary conditions discussed here result in
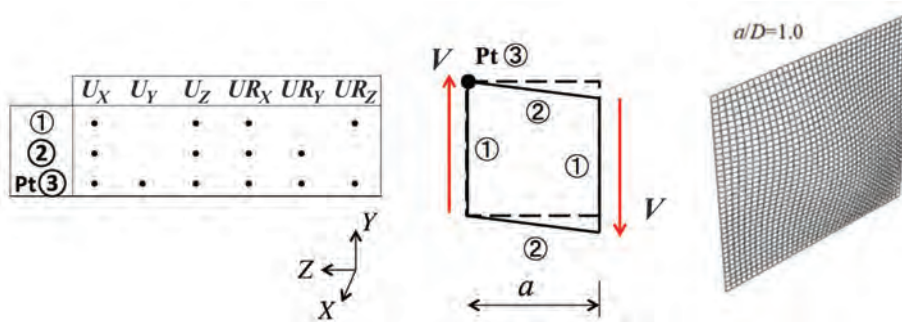

Fig. 1. Boundary conditions of the FE model (left), and mesh density in first mode buckled shape (right). Location 3 is a point (Pt) on the upper left corner.

the same V_{cr}. Comparing V_u using the Yoo and Lee (2006) boundary conditions to that produced by the current study's boundary conditions (Figure 1), one obtains V_u values equal to 437 kips and 593 kips, respectively, when analyzing the prototype plate. The current study's results match those of Glassman and Garlock (2016), which correlated well to experimental results (as will be discussed later in this paper). The authors, therefore, proceed with the boundary conditions of Figure 1 for the remainder of this paper.

The thin plate was meshed using S4 shell elements (doubly curved, general-purpose, finite membrane strains) with four integration points on the surface, as shown in Figure 2. A preliminary study was conducted to determine an appropriate number of section points through the depth, in which three, five, seven, and nine section points at each surface integration point were evaluated by examining stress values and shear load sustained at $V = V_u$. The results for five, seven, and nine section points differed by less than 1%, and five section points as shown in Figure 2 are therefore used for all other analyses discussed in this paper.

To capture the plate transition from its initial unbuckled state to post-buckling behavior to ultimate shear strength, nonlinear analyses were conducted using a modified Riks procedure. These analyses require the insertion of an initial geometric imperfection to perturb the mesh prior to loading, which allows the load-displacement curve to proceed beyond the buckling bifurcation point and progress into the post-buckled behavior until V_u is reached (Glassman and Garlock, 2016). To create this initial geometric imperfection, the eigenmode shape associated with the lowest elastic positive eigenvalue is multiplied by a defined scale factor. Previous research by Garlock and Glassman (2014) found that a scale factor of $D/10{,}000$ was sufficient for these models, and this scale factor was therefore selected for the present study. Mesh convergence studies were conducted using an eigenvalue extraction analysis. The final mesh selected is shown in Figure 1 and is equal to 37×37 elements [approximately 1.57 in. (40 mm) square each].

Using this approach, the FE solution for the elastic shear buckling load, V_{cr}, equaled 345 kips (1535 kN). This value has less than 1% error compared to a theoretical solution of 343 kips (1526 kN), which is obtained from Equation 1:

$$\tau_{cr} = k \frac{\pi^2 E}{12(1-\nu^2)\left(D/t_w\right)^2} \tag{1}$$

In Equation 1, τ_{cr} is the elastic shear buckling stress, E is Young's modulus, ν is Poisson's ratio, D is the depth of the plate, t_w is the plate thickness, and k is the elastic shear buckling coefficient. The value of k is a function of the span-to-depth (aspect) ratio (a/D) of the plate and the boundary conditions applied to its edges (Timoshenko and Gere, 1961). For a plate with $a/D = 1$ and simply supported on all four edges, $k = 9.34$. D/t_w is the slenderness ratio, which is a measure of how susceptible the plate girder is to web shear buckling. The elastic critical shear buckling load, V_{cr}, is calculated by multiplying Equation 1 by $D \times t_w$.

The modeling approach described earlier has also been validated via comparison to experimental test data for various a/D and D/t_w ratios. Glassman and Garlock (2016) considered the results of 16 previous experiments whose results are published in Basler et al. (1960), Bergfelt and Hovik (1968), Kamtekar et al. (1972), Rockey and Skaloud (1972), Evans et al. (1977), and Narayanan and Rockey (1981). Glassman and Garlock's (2016) FE models used the same setup conditions as discussed earlier and showed very close agreement with the ultimate post-buckling shear capacity, V_u, of each plate. Specifically, the FE models predicted V_u values to within ~10% of the published experimental values with one exception where the flange-to-web thickness ratio (t_f/t_w) was quite large compared to other tests (thus influencing that plate's boundary conditions more so than the other validation cases).

RESULTS

Sign Conventions and Definitions

To properly interpret the finite elements results, the definitions and sign conventions of the stresses, moments and rotations are defined in this paper as follows, in the context of the Abaqus output:

- Tensile stresses are positive and compressive stresses are negative.

- SP:1 and SP:5 refer to the section points on the two surfaces of the plate as shown in Figure 2.

- The element stresses, σ_1, σ_2 and σ_{12} are defined in Figure 3(a) in the positive direction.
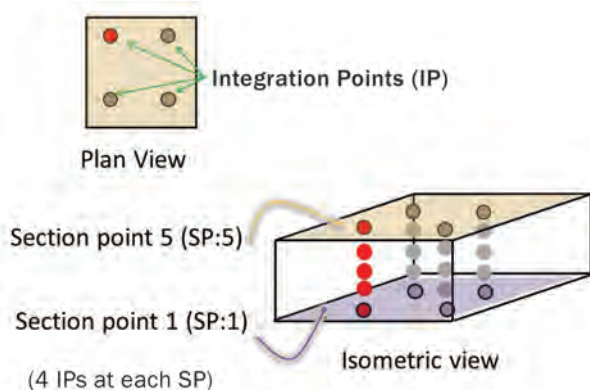

Fig. 2. Integration points and section points on each shell finite element.

- Maximum principal stresses (σ_{max}) are the maximum positive value, thus typically corresponding to maximum tensile stresses. If no tension is present, the value will be negative, thus corresponding to the minimum compressive value [see Figure 3(b)].

- Minimum principal stresses (σ_{min}) are the maximum negative value, thus typically corresponding to maximum compressive stresses. If no compression is present, the value will be positive, thus corresponding to the minimum tensile value [see Figure 3(b)].

- Von Mises stresses are defined for the principal plane stress condition defined by Equation 2, where σ_y is the yield stress. Figure 4 plots this yield surface.

$$\sigma_y^2 = \sigma_{max}^2 + \sigma_{min}^2 - \sigma_{max}\sigma_{min} \qquad (2)$$

Figure 5 shows the shear force-deformation plot with V_{cr} and V_u for this plate labeled for clarity. Deformation is measured at the lower right corner of the plate as shown by the dot in the inset figure. Note that the plot can be divided into three phases of shear loading. Phase I represents the elastic state prior to buckling. In phase II, the plate has exceeded V_{cr} but still exhibits nearly linear behavior. In phase III, the plate's force-deformation behavior becomes highly nonlinear. For this plate, the boundary between phases II and III lies approximately at the shear halfway between V_{cr} and V_u. In the following sections, the stresses and strains throughout the plate will be evaluated at two values of loading: (1) in phase II at $V = 1.15 \times V_{cr}$ (when the plate has recently buckled) and (2) in phase III at V_u (when the plate has reached its peak shear load during post-buckling response).

Ultimate Shear Post-Buckling Load, V_u, and Deformation

Figure 6 illustrates the final deformed shape at the ultimate (post-buckling) shear load, V_u, that, for this plate, equals 593 kips (2636 kN). The out-of-plane deformations are manifested in three half-wavelengths or bulges from point B to point D. The surface shown in Figure 6 represents the SP:5 face from Figure 2. Therefore, along the "tension field" (from
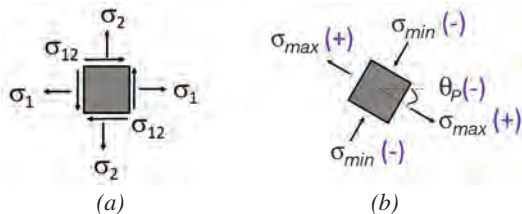
point A to point C, where the red color represents maximum out-of-plane positive displacement), it will be shown that the SP:5 stresses will be in tension and SP:1 stresses will be in compression due to the significant bending in the plate. Conversely, in Figure 6, where the dark blue color shows large negative displacement, SP:5 stresses will be in compression and SP:1 stresses will be in tension. A thorough analysis of the stresses will be discussed in sections to follow, where it will be shown that the plate bending due to this post-buckling out-of-plane deformation dominates the response when V_u is reached.

Plate Behavior Just after Elastic Buckling

Before the plate reached the elastic shear buckling load V_{cr}, the FE results were consistent with the theoretical behavior of a plate under pure shear: The angle of the principal stress, θ_p, was 45°, and the principal stresses in tension and compression (σ_{max} and σ_{min}, respectively) were equal and opposite to one another and also equal to the shear stress [$V/(D \times t_w)$, where V is the applied load]. Note that Abaqus does not output θ_p—this value was derived using σ_1, σ_2 and σ_{12} with the well-established equation based on Mohr's circle. In this section, the state of the plate when the shear $V = 1.15 \times V_{cr}$ (i.e., near the beginning of post-buckling behavior) is examined to enable a comparison to ultimate post-buckling behavior when V_u is reached. The following behavior is observed:

- *Principal stress direction, θ_p:* Figure 7 plots the θ_p contours for $V/V_{cr} = 1.15$. It can be seen that this angle has not changed significantly from the pre-buckling state when this angle was 45°.
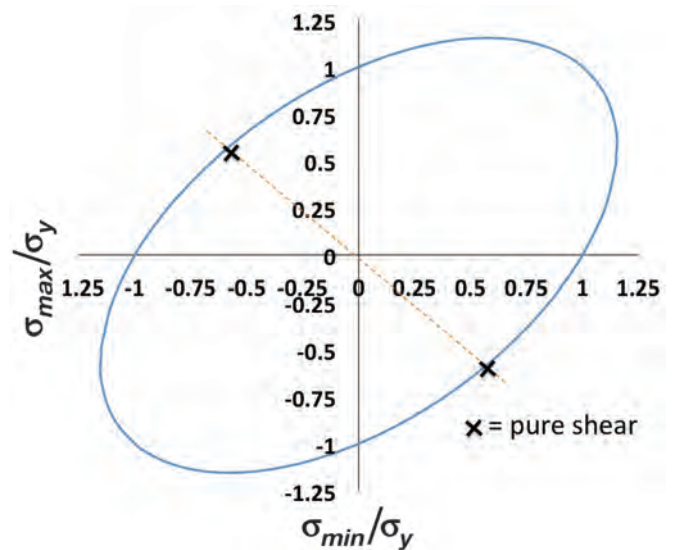

Fig. 3. (a) Positive stresses on element; (b) principal stresses and principal stress direction (with Abaqus sign convention in parentheses).

Fig. 4. Von Mises yield surface.

- *Principal stresses:* Figure 8 plots the σ_{min} and σ_{max} contours for $V/V_{cr} = 1.15$. None of these stresses have reached yield (50 ksi, 345 MPa), and the magnitude of σ_{min} (compressive principal stress) is comparable to that of σ_{max} (tension principal stress). At an elastic buckling load of 344 kips (1532 KN), the elastic buckling stress theoretically equals 13.7 ksi (95 MPa). At $V = 1.15 \times V_{cr}$, Figure 8 shows that both σ_{min} and σ_{max} have generally increased beyond 13.7 ksi.

- *Von Mises stresses*: Figure 9 plots the von Mises stress contours for $V/V_u = 1.15$. As would be expected, the stresses are shown to be well below yield (50 ksi).

Though the contour patterns are similar, Figures 7, 8 and 9 all show some variation in the magnitudes of plotted results between the SP:1 and SP:5 faces of the plate. More significant levels of variation are shown for the principal and von Mises stresses in Figures 8 and 9. The stress patterns on the opposing SP:1 and SP:5 faces highlight the emergence of bending moment through the thickness of the post-buckled plate in addition to in-plane stress. These moments are caused by second-order bending due to in-plane compression of the buckled plate. Each of the three half-wavelengths of this prototype's buckled shape experiences "bulging" as the top right and bottom left corners of the plate (from B to
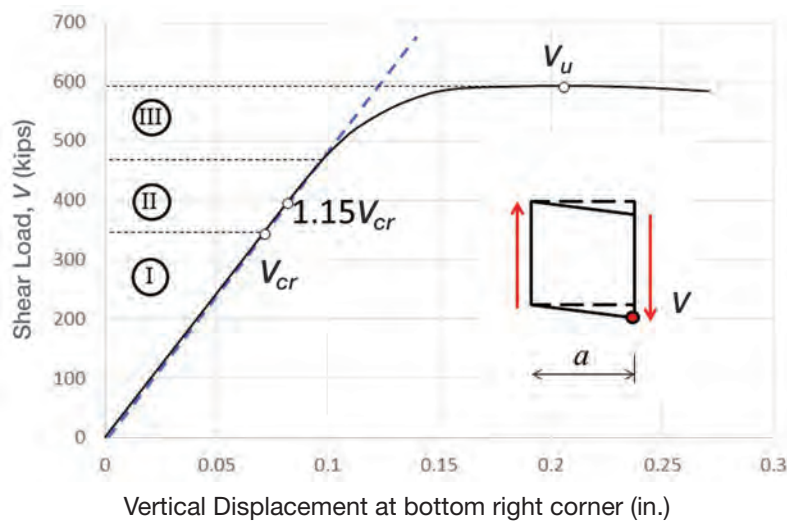

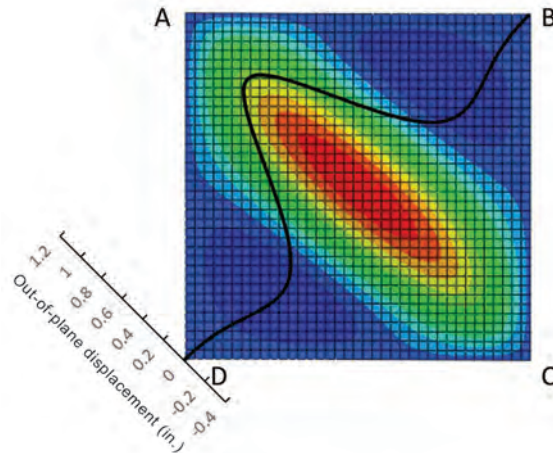Fig. 5. Shear displacement of the plate, with V_{cr} and V_u labeled.

Fig. 6. Deformed shape contour at V_u, with out-of-plane deformation plot superimposed (dark black line). The face shown (front face) corresponds to SP:5; the back face (not shown) corresponds to SP:1 (see Fig. 2).

D in Figure 6) are pushed closer together by the pure shear force.

Plate Behavior at the Ultimate Shear Post-Buckling Load, V_u

The following observations are made regarding the stress state of the plate when the shear, V, equals the ultimate shear post-buckling load, $V_u = 593$ kips (2636 kN).

- *Principal stress direction, θ_p*: Figure 10 plots the θ_p contours for $V = V_u$. It can be seen that this angle is no longer ~45° and now varies between 15° and −65°. Also, the values are now significantly different on each face (SP:1 and SP:5) because the principal stresses are also different on each face. θ_p is shown to be largely dependent on the out-of-plane post-buckled deformation.

- *Principal stresses:* Figure 11 plots the σ_{min} and σ_{max} contours for $V = V_u$. Both σ_{min} and σ_{max} have reached yield in the regions marked by the bold lines encircling gray shading. The magnitudes, signs (positive, negative) and locations of these stresses are related to the out-of-plane post-buckled deformation (and bending) of the plate at V_u as seen previously in Figure 6. The σ_{max} contours for SP:5 in Figure 11 show a distinct band of yielding in the tension field direction, which generally supports the assumptions in the current state of practice. However, the σ_{max} contours for SP:1 show much lower maximum stress (actually remaining negative in compression) in

this same region due to bending. The σ_{min} stresses at yield are located along the tension field for SP:1 and along two smaller bands that are parallel to the tension field at SP:5. These stresses represent the compression face of bending in the buckled half-wavelength bulges along the diagonal. The emergence of these large compressive stresses on the SP:1 face indicates that the large tensile stresses in the tension field on the SP:5 face are caused by a combination of in-plane stress and second-order bending.

- *Von Mises stresses*: Figure 12 plots the von Mises stress contours for $V = V_u$. Nearly the entire plate surface has reached the von Mises yield condition (at 50 ksi, again shown with bold lines and gray shading) on both faces. At ultimate shear, the plate experiences a near saturation of von Mises yielding due to the combination of internal forces that develops in its buckled shape. Figure 12 shows that face SP:5 experiences a more widespread saturation of von Mises yielding than SP:1, which has a distinct band of yielding along the tension field diagonal and two other "pockets" of yield parallel to it. Note that bending-induced compression stress has caused von Mises yielding in the tension field diagonal on face SP:1 rather than in-plane tensile stresses. This deviates from the current state of practice, which assumes in-plane stress to be the primary contributor to reaching ultimate shear capacity.

- *Equivalent plastic strains*: Figure 13 plots (for $V = V_u$) the equivalent plastic strains normalized by the yield
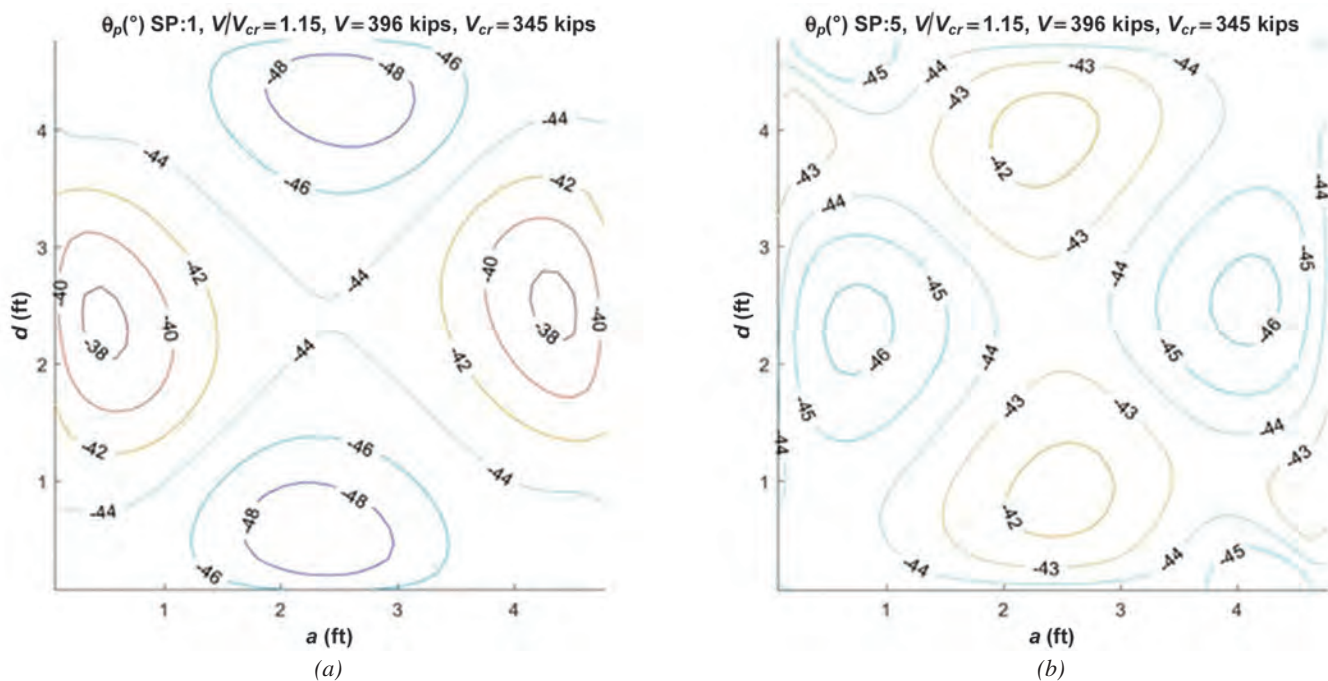

Fig. 7. Principal stress direction, θ_p, for $V/V_{cr} = 1.15$ in degrees: (a) = SP:1; (b) = SP:5 (see Figs. 2, 3).
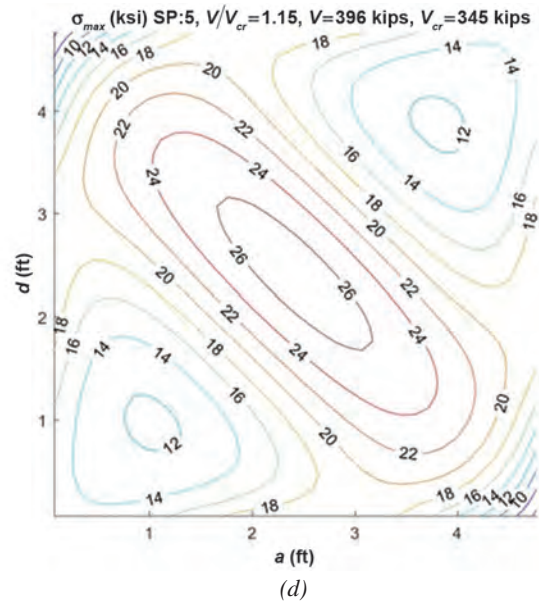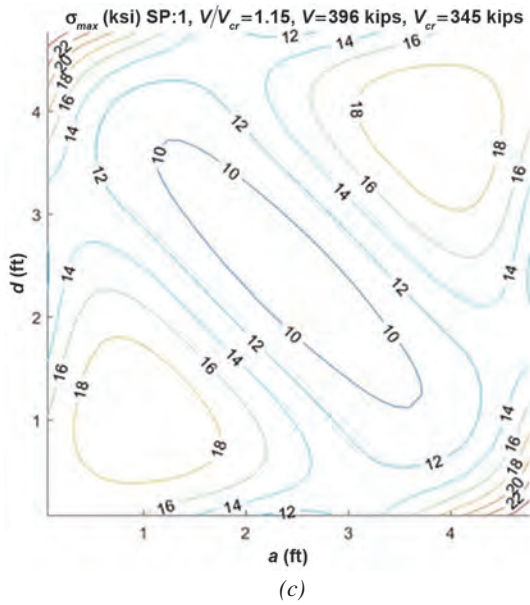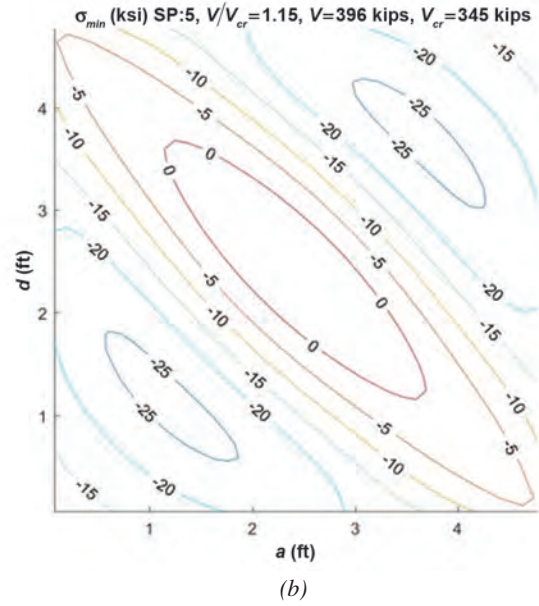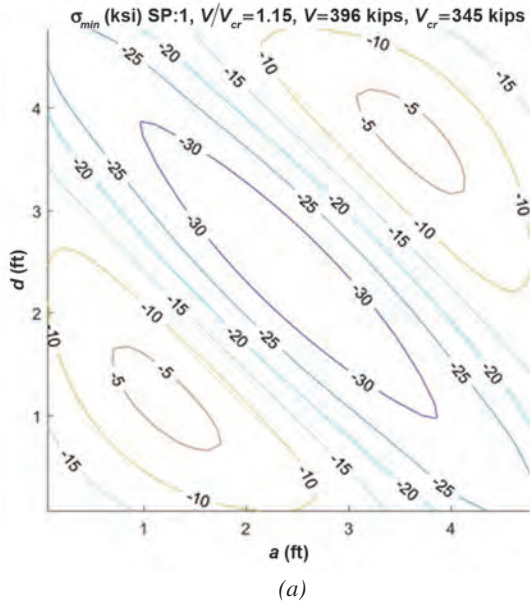
Fig. 8. Principal stresses σ_{min} (a; b) and σ_{max} (c; d) for $V/V_{cr} = 1.15$ (ksi): (a), (c) = SP:1; (b), (d) = SP:5 (see Figs. 2, 3).
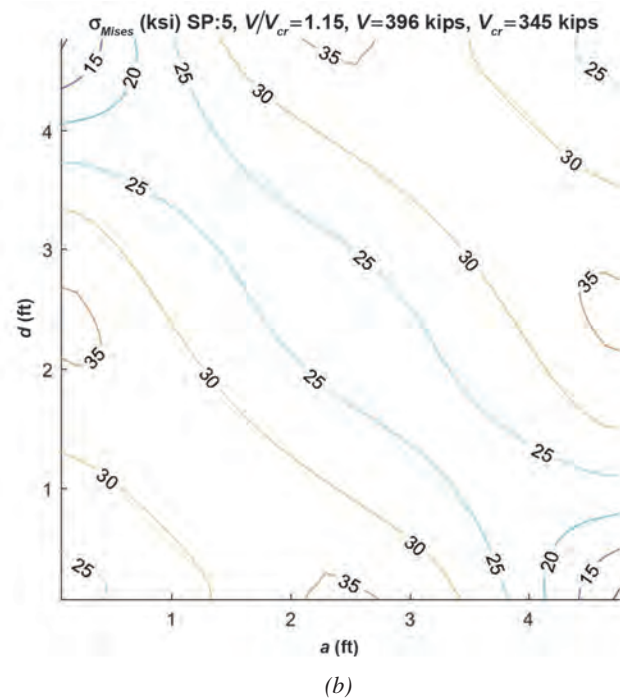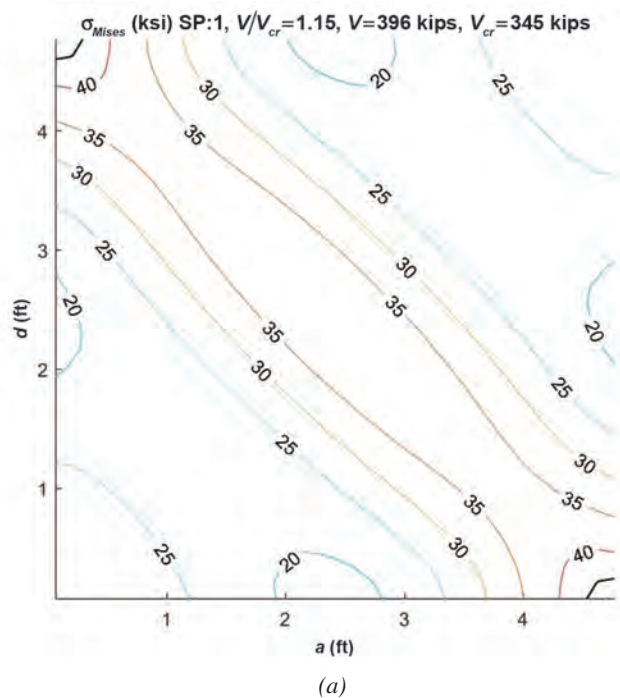
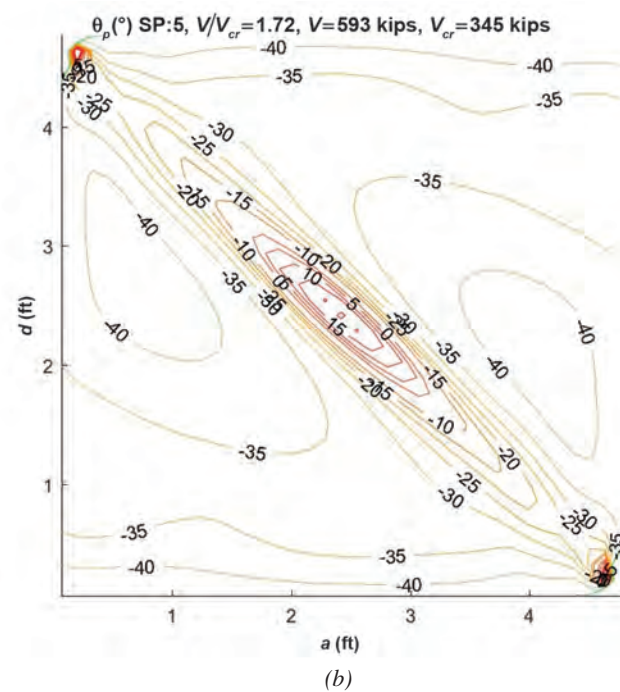Fig. 9. Von Mises stresses for V/V_{cr} = 1.15 (ksi). (a) = SP:1; (b) = SP:5 (see Figs. 2, 3, 4).
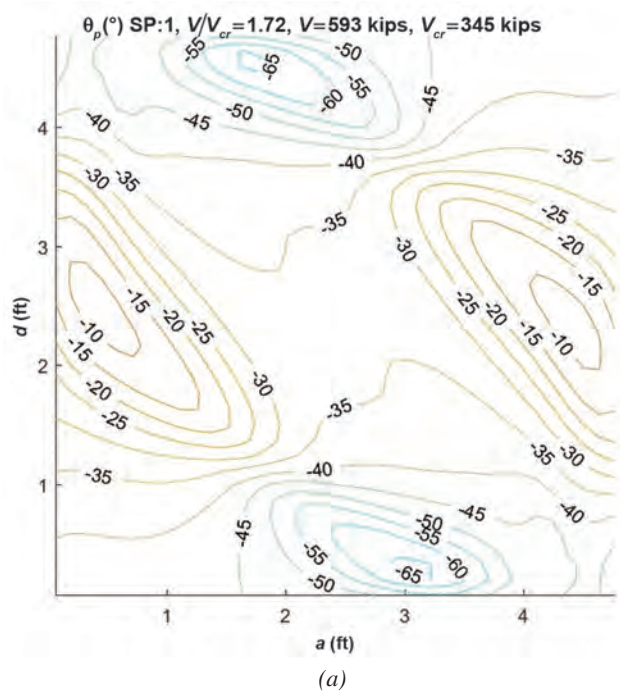

Fig. 10. Principal stress direction, θ_p, for $V = V_u$ in degrees: (a) = SP:1; (b) = SP:5 (see Figs. 2, 3).
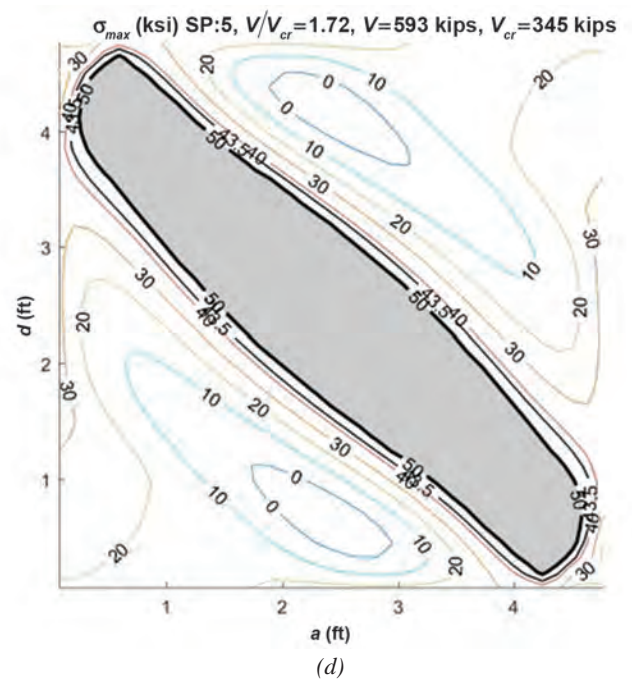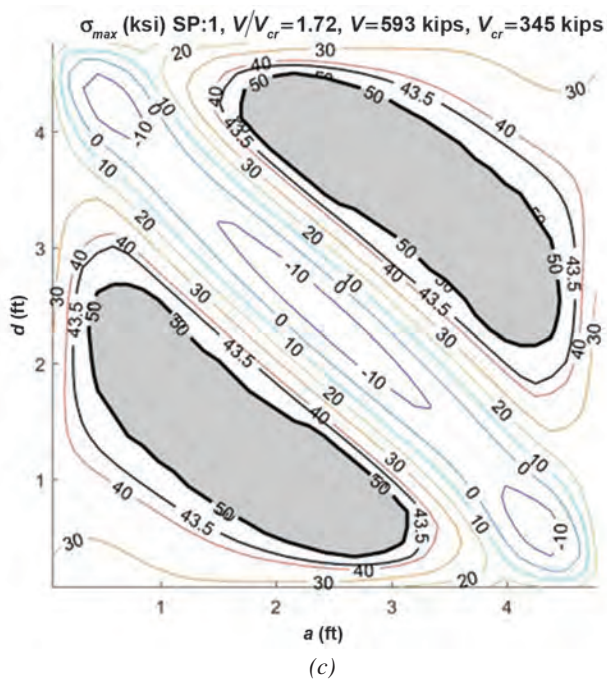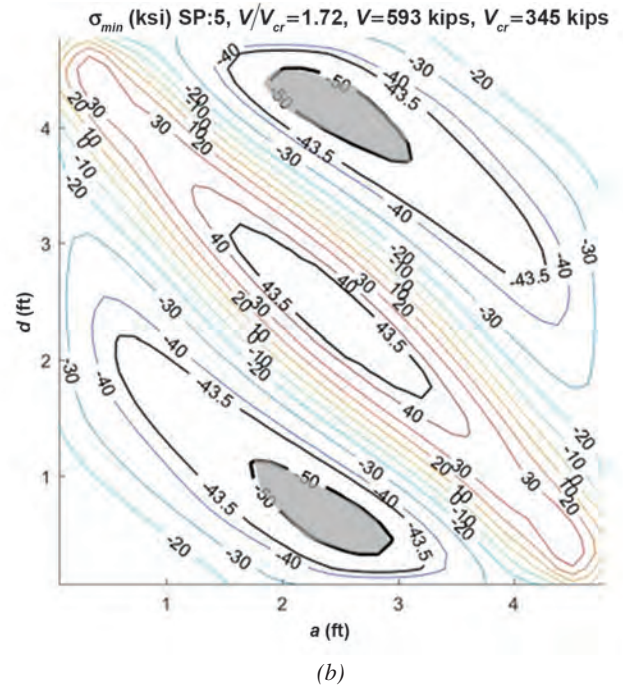
Fig. 11. Principal stresses σ_{min} (a; b) and σ_{max} (c; d) for $V = V_u$ (ksi). (a), (c) = SP:1; (b), (d) = SP:5 (see Figs. 2, 3). Gray-shaded regions represent areas that have reached yield.

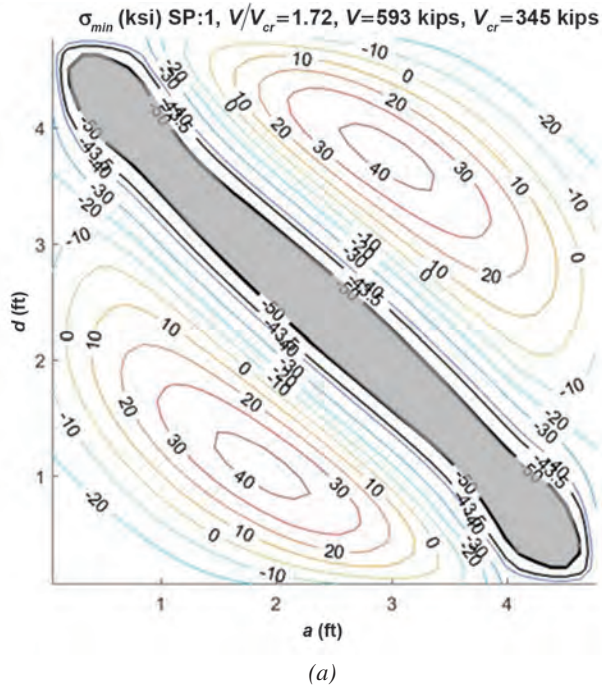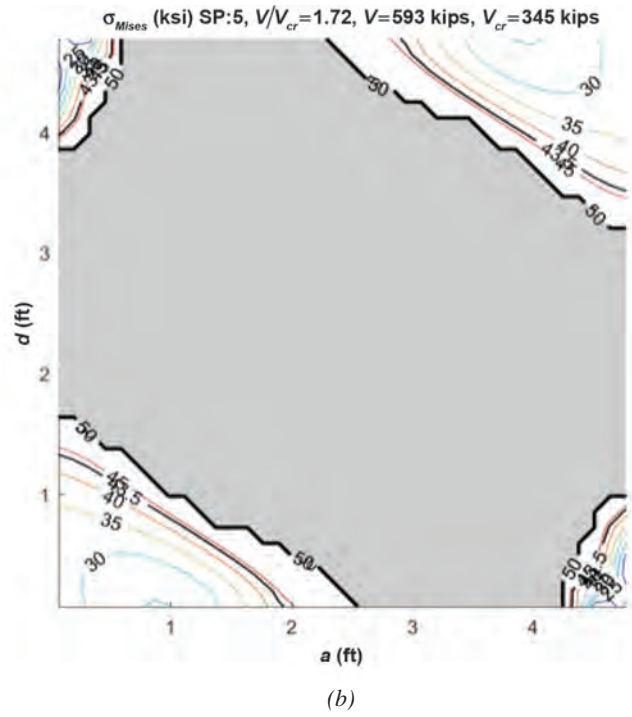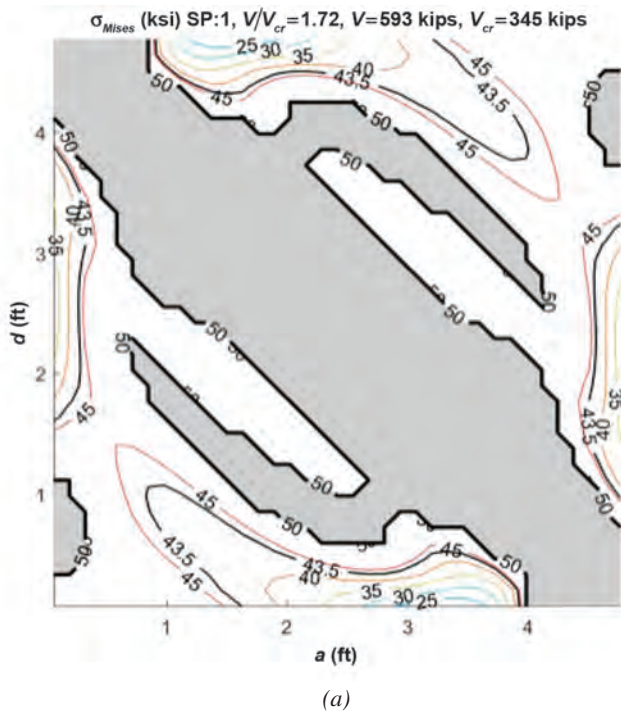Fig. 12. Von Mises stresses for $V = V_u$ (ksi): (a) = SP:1; (b) = SP:5 (see Figs. 2, 4).
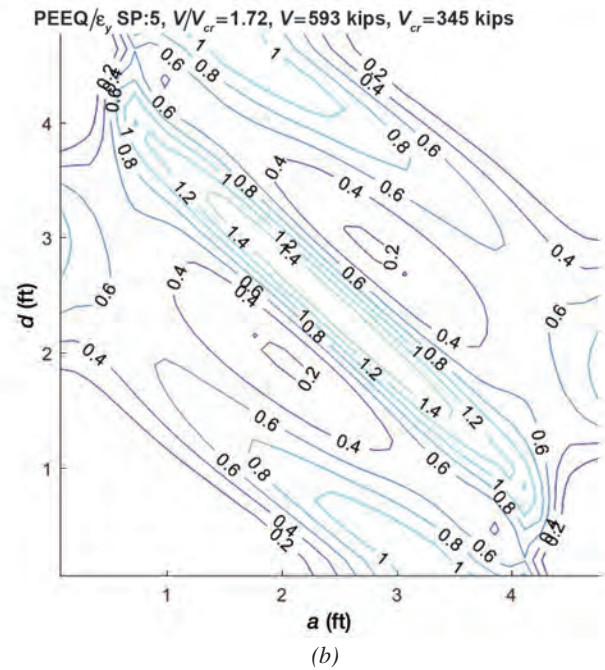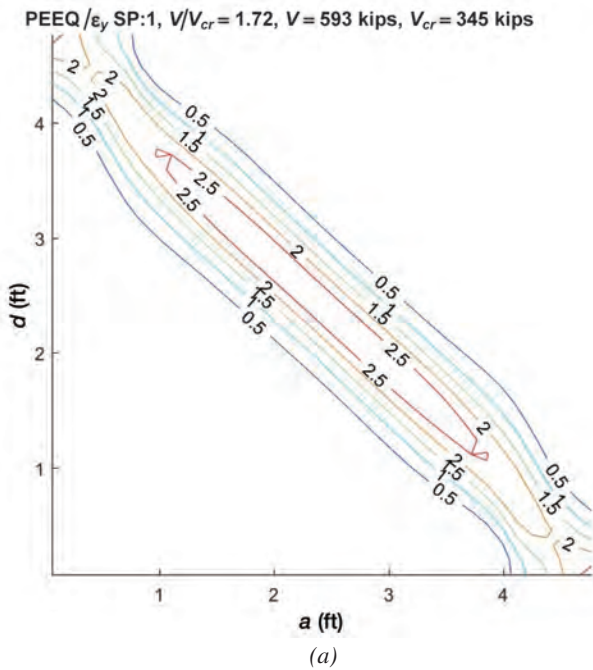Gray-shaded regions represent areas that have reached yield.

Fig. 13. Equivalent plastic strains normalized by yield strain ($\varepsilon_y = 0.001725$) for $V = V_u$: (a) = SP:1; (b) = SP:5.

strain ($\varepsilon_y = 0.001725$) to provide a relative measurement of ductility utilization. This value quantifies the plastic strain as related to von Mises plasticity. When comparing to Figure 12, it can be seen that these strain values are greater than zero only where yield has been reached. In the tension field region, the equivalent plastic strains are larger than $2 \times \varepsilon_y$ on one face and just slightly greater than ε_y on the other face. The material model assumes strain hardening begins at a strain value equal to 0.02. From Figure 12, it can be inferred that the strains in the plates are well below this value.

Bending Stresses at the Ultimate Shear Post-Buckling Load, V_u

The results presented thus far indicate that bending through the thickness of the plate due to post-buckled out-of-plane deformations has a large effect on the stress distribution. In this section, the axial stress is distinguished from the bending stress for both σ_1 and σ_2 (see Figure 3). The stresses are output at the five section points (SPs; i.e., the through-thickness integration points) through the shell element thickness (see Figure 2). Abaqus outputs the total stress and the average section stress (i.e., membrane axial stress) at each SP. The bending stress is calculated by subtracting the membrane stress from the total stress.

Figure 14 presents the axial (in-plane) and bending (second-order) stresses through the plate thickness for $V = V_u$ (ksi). Figure 14(a) represents stress patterns typically seen along the tension field. These stresses are nearly linear through the depth and become slightly nonlinear at the top and bottom surface, where the stresses, considering von Mises plasticity, have reached yield. Figure 14(b) represents stress patterns typically seen outside of the tension field (near-upper-right and lower-left corners). In these regions,

the stresses are linear through the depth and smaller than those in the tension field.

Figure 15 presents the axial stress (top row) and bending stress at SP:1 and SP:5 (middle and lower rows) for both σ_1 (left column) and σ_2 (right column). It is clearly seen that bending stresses dominate because their magnitudes are nearly two times larger than axial stress for σ_1 and on the order of 10 times larger for σ_2. These plots clearly show that second-order moment in the post-buckled shape makes a significant contribution to the onset of ultimate shear capacity.

Figure 16 provides additional illustration of the bending in the plate by plotting σ_{min} and σ_{max} at the shell element in the center of the plate against the vertical plate displacement at the bottom corner for both SP:1 and SP:5. The point of elastic shear buckling when V_{cr} is reached is clearly shown where SP:1 and SP:5 bifurcate for both σ_{min} and σ_{max}. This increasing divergence clearly indicates the onset of second-order bending moment through the thickness of the plate. At V_u, SP:1 and SP:5 are significantly different for both σ_{min} and σ_{max}.

Membrane Stresses at the Ultimate Shear Post-Buckling Load, V_u

It is worthwhile to observe the influence of stresses independent of bending effects. Thus, this section discusses the membrane stresses (i.e., the axial stresses), which are equal to the membrane forces divided by the plate thickness. Figure 17 plots the membrane stresses along the diagonal directions of the compression and tension paths (at $-45°$ and $+45°$, respectively) when the shear load equals V_u. Figure 17(a) marks with a thick bold line the 13.7-ksi (95-MPa) contour, which represents the stress at the elastic shear buckling load, V_{cr}. Inside the dark bold line, stresses are at or below 13.7 ksi, while outside of this region compressive stresses
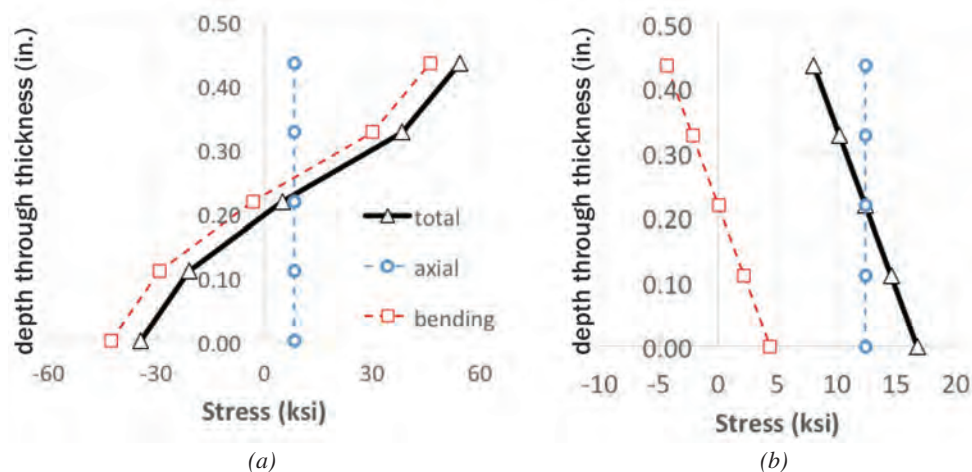
Fig. 14. Plot of axial and bending stresses in the σ_1 direction through the plate thickness for $V = V_u$: (a) representative stresses along tension field; (b) = representative stresses outside of tension field (near-upper-right and lower-left corners).
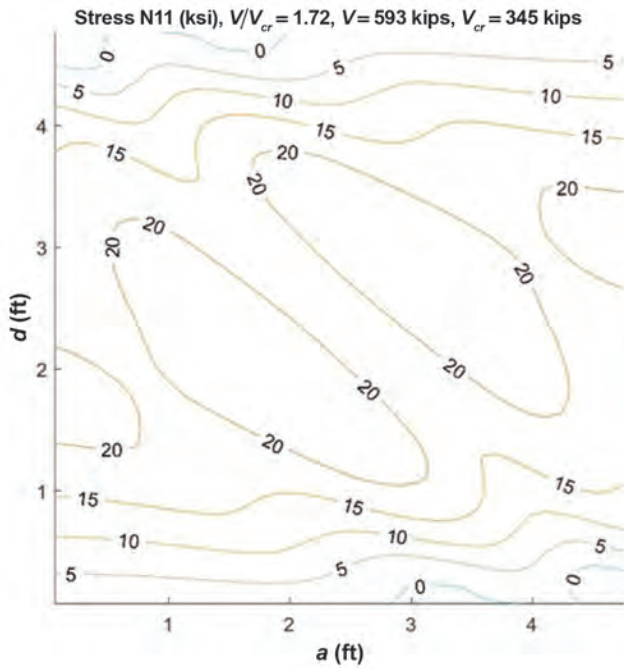
(a) Axial stress—for σ_1 direction
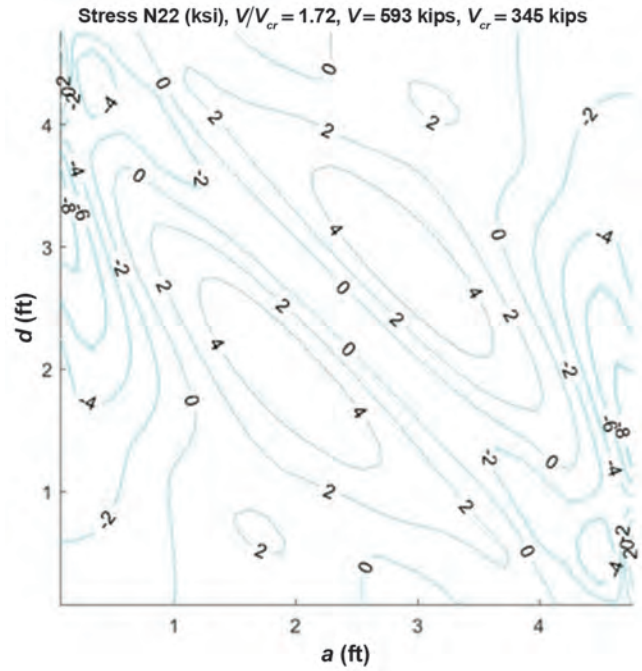
(b) Axial stress—for σ_2 direction
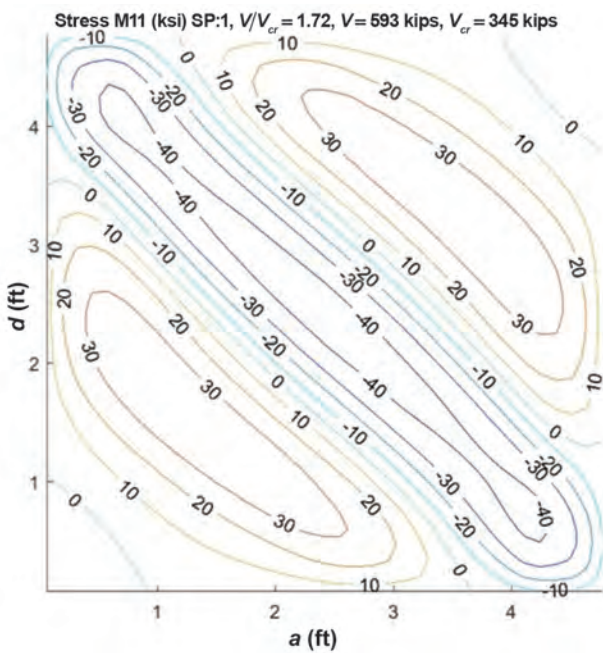
(c) Bending stress—for σ_1 direction; SP:1 face
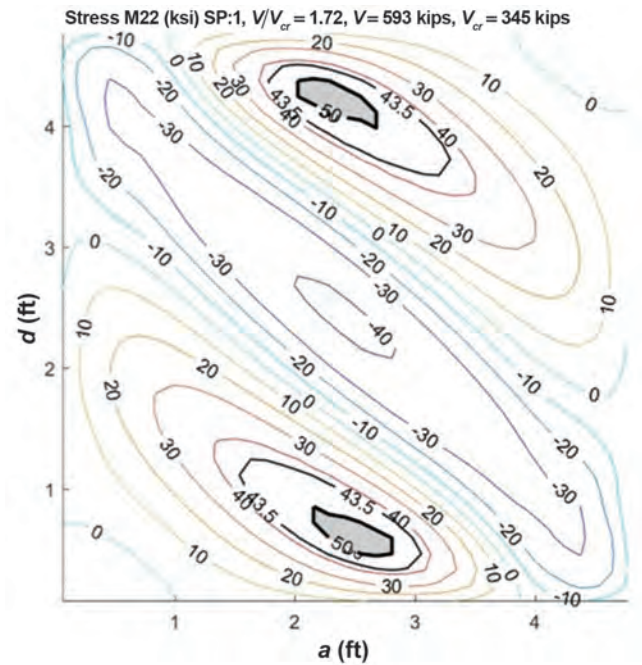
(d) Bending stress—for σ_2 direction; SP:1 face

Fig. 15(a–d). Axial and bending stresses for $V = V_u$ (ksi). Left figures are for σ_1 and right are for σ_2.
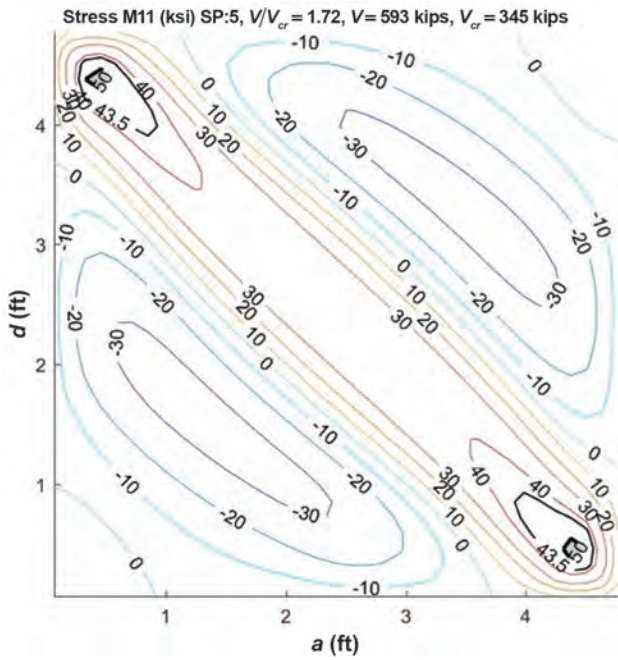
(e) Bending stress—for σ_1 direction; SP:5 face
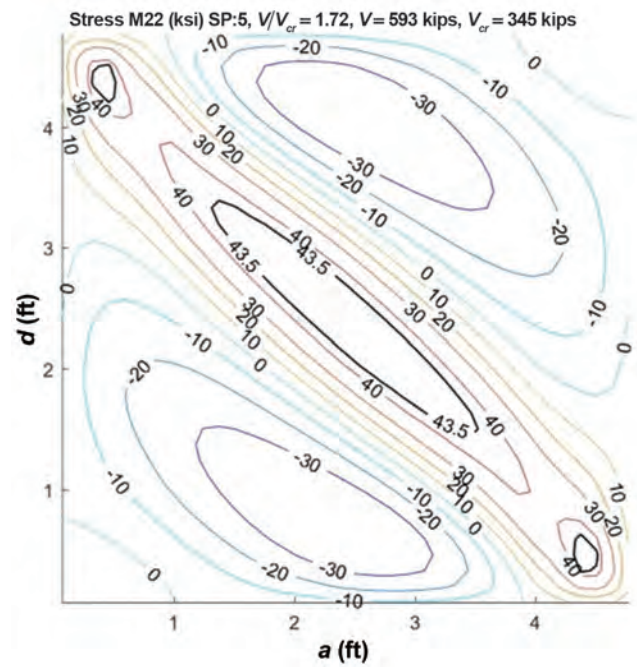
(f) Bending stress—for σ_2 direction; SP:5 face

Fig. 15(e–f). Axial and bending stresses for $V = V_u$ (ksi). Left figures are for σ_1 and right are for σ_2.
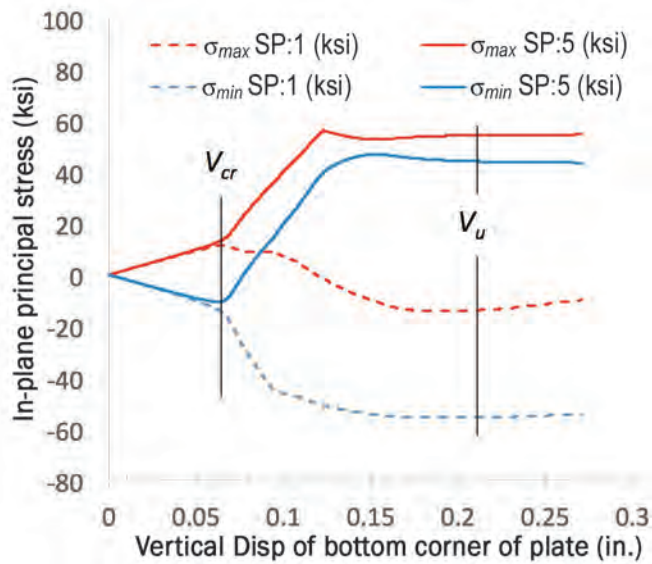
Fig. 16. σ_{min} and σ_{max} for the shell element in the center of the plate on both surfaces
SP:1 and SP:5. Elastic shear buckling, V_{cr}, and ultimate shear post-buckling, V_u, are labeled.

reach up to 26 ksi. This figure illustrates that compression continues to grow beyond V_{cr}, which is contrary to tension field theory assumption. Yoo and Lee (2006) have similarly shown that compression stresses will increase beyond elastic buckling, predominantly along the edges of the web panel. Figure 17(b) shows that tension stresses range from 24 to 40 ksi; the tension field has a stiffer load path as illustrated in the conceptual sketches in Figure 17, which translates into larger stresses.

Figure 18 plots the diagonal membrane stresses versus shear load for every element along the corner-to-corner diagonal of the tension path [Figure 18(a)] and compression path [Figure 18(b)]. One curve is plotted for each element, and because the results are perfectly symmetrical, it appears

as though only half the elements on each diagonal are plotted. The orange curves represent the elements that are inside of the bold black contour of Figure 17(a)—that is, with compressive stresses equal to or less than 13.7 ksi at V_u. Green lines represent the elements that fall outside of this region. Figure 18(a) shows that all of the elements in the tension diagonal continue to increase beyond the 13.7 ksi reached at V_{cr}.

Figure 18(b) shows that after elastic buckling, compressive stresses continue to increase for all elements along the compression diagonal. An overall reduction in the rate of stress increase is observed after elastic buckling, with elements inside of the 13.7-ksi ring experiencing a larger reduction than elements outside of the ring. While Figure 17(a)

Fig. 17. (a) Compressive and (b) tensile membrane stresses (ksi) at V_u acting along the 45° diagonal directions shown.

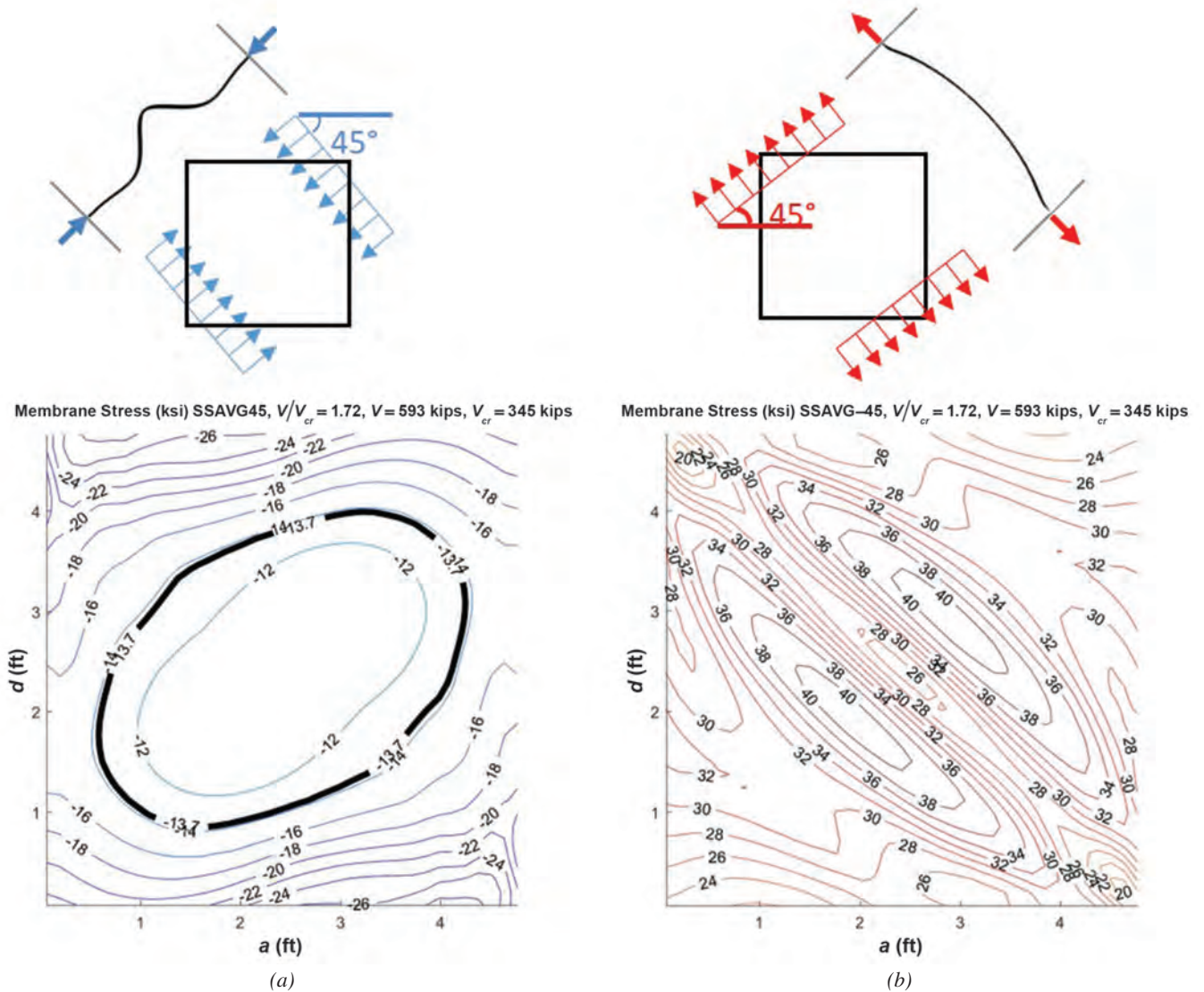shows that at V_u, some compressive stresses are below 13.7 ksi (σ_{min} at V_{cr}), Figure 18(b) shows that these elements reached stresses larger than 13.7 ksi before decreasing prior to failure.

The "intermediate" shear load V_i marked in Figure 18(b) represents the point at which an element along the compression diagonal first experiences a stress decrease. Note how V_i correlates to the transition from phase II to phase III in Figure 5. A change in stiffness in the load-deformation behavior occurs when the compression diagonal elements near the center of the plate experience reduced membrane stresses. The additional load-carrying capacity of a plate beyond V_{cr} is equal to $V_u - V_{cr}$ (see Figure 5). Figures 5 and 18 together show that about half of that additional capacity occurs while the compression load path is still in place and compressive stresses are increasing throughout. Compression is thus playing a clear role in developing the post-buckling shear strength.

The membrane stresses along the diagonal directions of the compression and tension paths (at $-45°$ and $+45°$, respectively) at V_i are shown in Figure 19. It is observed that the compressive stresses in all elements do indeed exceed that at V_{cr} (13.7 ksi). In the center of the plate, the tensile membrane stresses are larger than the compressive membrane stresses (24 ksi vs. 15.5 ksi, respectively), but at the edges of the web panel, they are similar.

INTERRUPTING THE COMPRESSION PATH

The results presented in the preceding section indicate that compression and second-order bending stresses (due to large, out-of-plane deformations) play an important role in the post-buckling performance of this slender plate. While it is not clear yet how the compression behavior directly contributes to V_u, studies that interrupt the compression field, as presented in this section, can provide some clues. To
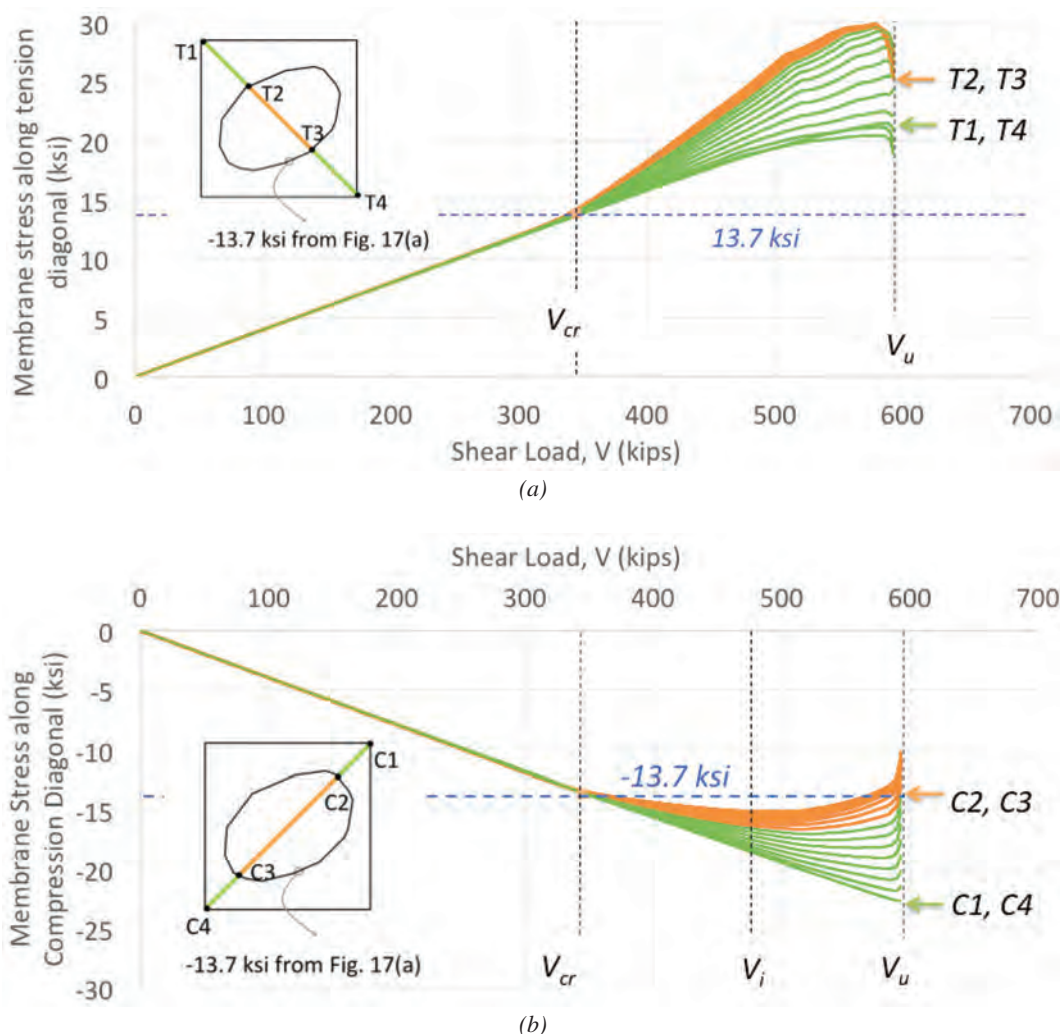

Fig. 18. Plot of membrane stresses versus applied shear load for finite elements along the (a) tension diagonal and (b) compression diagonal.

this end, the plate was modified in two ways: (1) by cutting the compression field corners by 16% of the depth, D (model name = CUT), thus reducing the area by 3%, and (2) by cutting slits near the corners along the compression field (model name = SLITS), thus reducing the area by 1%. Images of these models and the resulting V_{cr} and V_u values obtained from finite element analysis are shown in Table 1. Contour plots of the von Mises stress when the plate reaches V_u are shown for each case in Figure 20. Contour plots of the equivalent plastic strains at V_u are shown for each case in Figure 21.

Table 1 shows that interrupting the compression field delays the onset of elastic buckling and increases V_{cr} up to 24%. For the cut case, V_u is unaffected because the cut corners do not deter the development of von Mises stress

patterns similar to the full original plate, as shown in Figure 20. For the slits case, the slits alter the von Mises stress patterns on the top face of the plate (by interrupting the edges of the von Mises stress saturation), thus reducing the ultimate shear capacity below the full plate model (a 5% reduction).

The plots of equivalent plastic strains in Figure 21 show similar patterns to the von Mises stress patterns. On the SP:1 face, these strains exceed zero only in the tension field, and all three plates show similar strain patterns despite their modifications. Furthermore, the magnitude of strain values is similar for all three plates. Although not shown, bending stresses again dominate over membrane axial stresses for the cut and slits cases as discussed previously for the full case (described in detail in Figure 15).
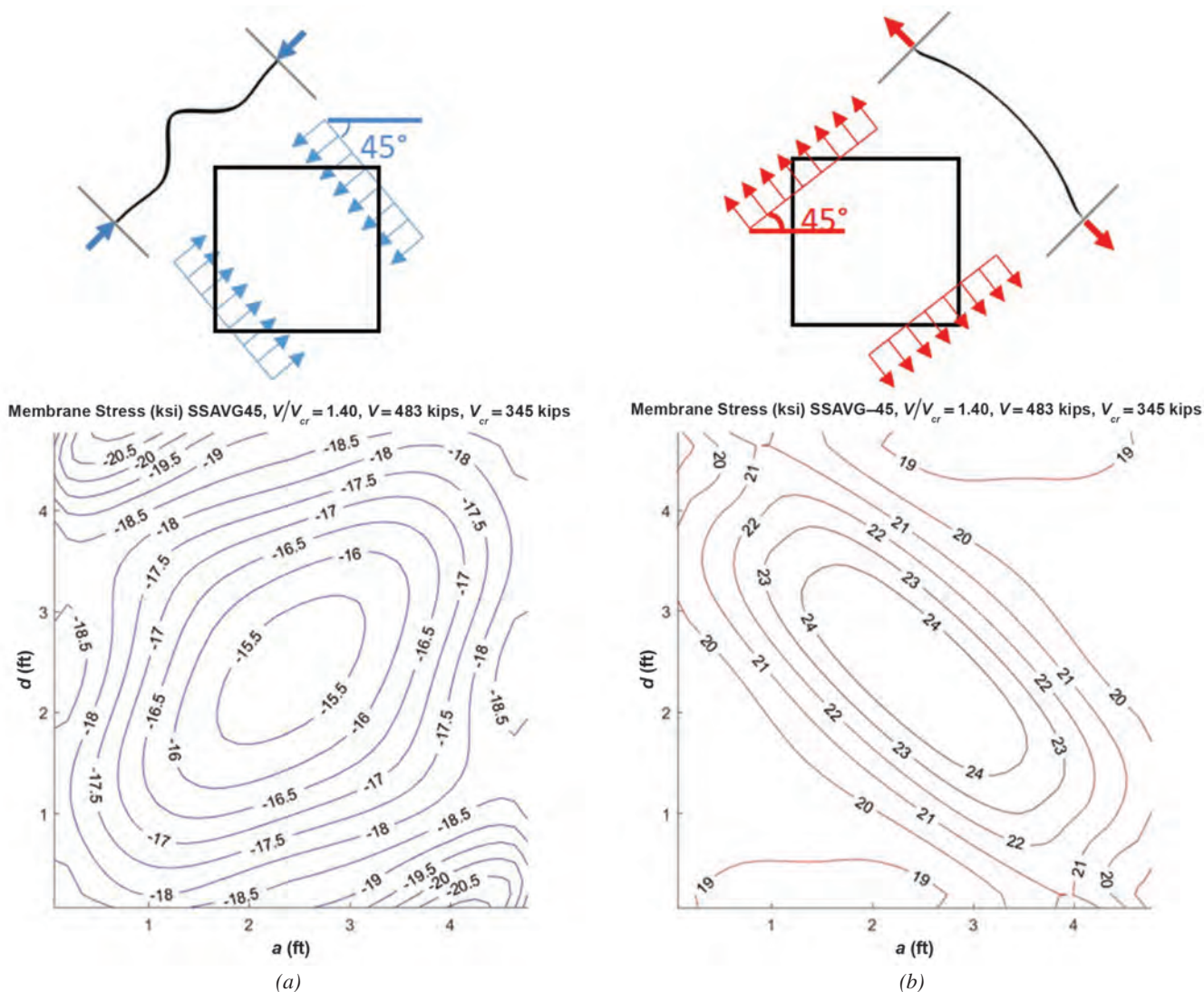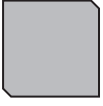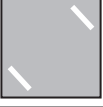
Fig. 19. (a) Compressive and (b) tensile membrane stresses (ksi) at the intermediate shear load V_i *[see Fig. 18(b)], acting along the 45° diagonal directions shown.*

Table 1. Finite Element Results of Modified Plates		V_{cr} (kips)	V_u (kips)
		(ratio to baseline)	
Full (baseline)		344 (1.00)	593 (1.00)
Cut		428 (1.24)	594 (1.00)
Slits		380 (1.10)	564 (0.95)
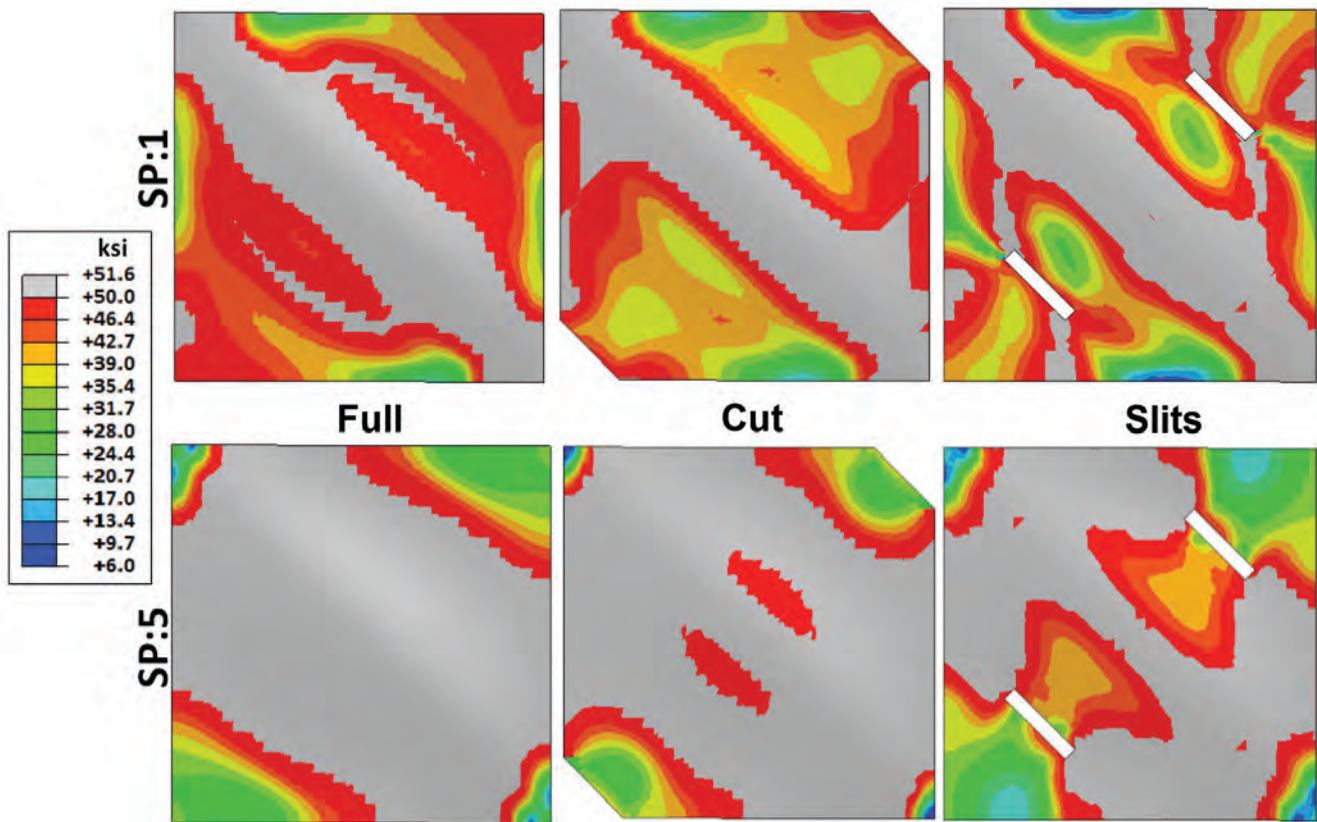
Fig. 20. Von Mises stresses at V = V_u for the full plate, the cut plate, and the plate with slits (units = ksi).

These results suggest that the elastic buckling load could be strategically modified to meet a given design objective with relatively minor modifications to the plate. The ultimate shear post-buckling load, however, is not significantly affected by these modifications. Based on these results, the authors are now exploring new potential models of ultimate plate post-buckling mechanics for thin plates that incorporate second-order bending of the post-buckled shape. Also, the mechanical impact and construction/life-cycle implications of the plate modifications will be examined in future research by the authors.

SUMMARY AND CONCLUSIONS

Post-buckling behavior of slender webs in steel plate girders has been a mainstay of plate girder design for several decades on the basis of semi-empirical equations that were originally developed in the 1960s. Though the existing state of practice is generally conservative, the assumption of pure in-plane stress in response to shear loads after the web has buckled does not capture the full mechanical responses of the thin plate. New research by the authors has begun to reexamine the post-buckling behavior of thin steel plates by considering the combined effects of in-plane stress and out-of-plane (second-order) bending. This study utilized a previously validated finite element modeling approach in Abaqus to analyze a prototype simply supported plate with an aspect ratio equal to 1.0. The results of these analyses showed that out-of-plane bulging of the post-buckled plate produces second-order bending moments due to compression along the diagonal opposite the tension field.

Although the conclusions summarized here are based only on the plate dimensions of this initial study, these results point to future research that is needed. The results are also relevant to plates of other proportions that demonstrate shear post-buckling behavior that is physically characterized by significant bulging/wrinkling on the diagonal (thus generating potentially significant bending stresses through the thickness).

- At the ultimate shear post-buckling load, V_u, the angle of principal stress direction is no longer 45° and instead varies between 15° (counterclockwise) and 65° (clockwise).

- The stress distribution through the plate thickness was separated into pure planar (i.e., axial) and bending (second-order) stresses. Bending stresses were found
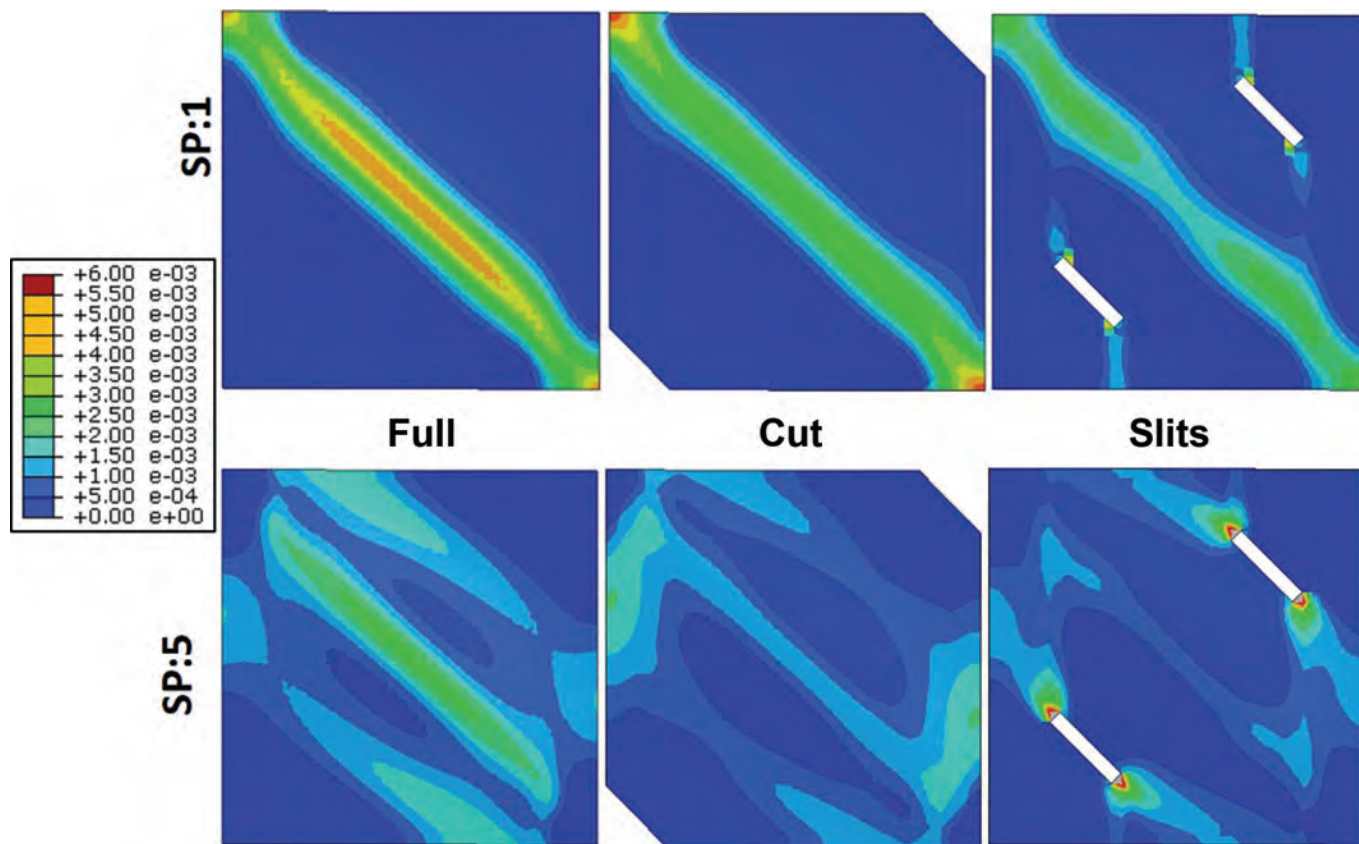

Fig. 21. Equivalent plastic strains at V = V$_u$ *for the full plate, the cut plate, and the plate with slits.*

to be significantly higher than the pure planar stresses at the ultimate post-buckling shear load. These stresses are created by second-order compression of the plate's buckled shape (i.e., the buckled half-wavelengths that bulge out-of-plane along the length of the compression field diagonal).

- At the ultimate post-buckling shear load, almost the entire plate has reached the von Mises yield boundary due to a combination of planar and bending stresses. The contours of von Mises yielding show some differences, however, for the opposing faces of the plate.

- Compression membrane stresses (which are independent of the second-order bending effects) continue to increase beyond elastic buckling, contrary to the current tension field theory assumption. These results suggest that compression effects can play a significant role in the post-buckling shear response.

Building from these results, and with the intent to further investigate the plate behavior, the authors examined some simple modifications of the plate that interrupted the compression diagonal. The results of two cases, with small through-plate cuts removed from the compression diagonal, showed (1) an increase of 10% to 24% in the shear load needed to induce buckling (i.e., the elastic shear buckling load) and (2) a negligible effect on the ultimate shear post-buckling load. These results indicate that the onset of elastic buckling can be delayed by interrupting the compression field, which may prove useful for designing girder webs.

REFERENCES

AISC (2016), *Specification for Structural Steel Buildings*, ANSI/AISC 360-16, American Institute of Steel Construction, Chicago, IL.

Basler, K. (1961), "Strength of Plate Girders in Shear," *Transactions ASCE,* Vol. 128, No. 2.

Basler, K., Yen, B.T. and Mueller, J.A. (1960), "Web Buckling Tests on Welded Plate Girders," Welding Research Council, Bulletin No. 64, September, New York, NY.

Bergfelt, A. and Hovik, J. (1968), "Thin-Walled Deep Plate Girders under Static Loads," *Proceedings of the IABSE Colloquium*, New York, NY.

Dassault Systemes (2011), "Abaqus 6.11ef Online Documentation" [online; accessed 2017].

Evans, H.R., Rockey, K.C. and Porter, D.M. (1977), "Tests on Longitudinally Reinforced Plate Girders Subjected to Shear," *Proceedings of Conference on Structural Stability*, Liege, Belgium.

FHWA (1982), *Standard Plans for Highway Bridges*, Vol. II, "Structural Steel Superstructures," Federal Highway Administration, Washington, DC.

Glassman, J. and Garlock, M. (2016), "A Compression Model for Ultimate Postbuckling Shear Strength," *Thin-Walled Structures*, Vol. 102, pp. 258–272.

Garlock, M. and Glassman, J. (2014), "Elevated Temperature Evaluation of an Existing Analytical Model for Steel Web Shear Buckling," *Journal of Constructional Steel Research,* Vol. 101, pp. 395–406. doi:10.1016/j.jcsr.2014.05.021.

Höglund, T. (1997), "Shear Buckling Resistance of Steel and Aluminum Plate Girders," *Thin-Walled Structures,* Vol. 29, pp. 13–30.

Jha, A. (2016), "Investigation of the Shear-Strength of Built-Up I-Section Members via Test Simulation," Master's Thesis, Department of Civil and Environmental Engineering, Georgia Institute of Technology, Atlanta, GA.

Kamtekar, A.G., Dwight, J.B. and Threlfall, B.D. (1972), "Tests on Hybrid Plate Girders (Report 2)," Report No. CUED/C-Struct/TR28, Cambridge University, Cambridge, UK.

Narayanan, R. and Rockey, K.C. (1981), "Ultimate Load Capacity of Plate Girders with Webs Containing Circular Cut-Outs," *Proceedings of the Institution of Civil Engineers*, Part 2, Vol. 71, pp. 845–862.

Porter, D.M., Rockey, K.C. and Evans, H.R. (1975), "The Collapse Behavior of Plate Girders Loaded in Shear," *Structural Engineering,* Vol. 53, No. 8, pp. 313–325.

Rockey, K.C. and Skaloud, M. (1972), "The Ultimate Load Behaviour of Plate Girders Loaded in Shear," *Structural Engineer*, Vol. 50, No. 1, pp. 29–48.

Timoshenko, S.P. and Gere, J.M. (1961), *Theory of Elastic Stability*, 2nd Ed., McGraw-Hill Book Company, New York, NY.

Wagner, H. (1931), "Flat Sheet Metal Girder with Very Thin Metal Web," Technical Notes 604, 605, 606, National Advisory Committee on Aeronautics, Washington, DC.

White D.W. and Barker M.G. (2008), "Shear Resistance of Transversely Stiffened Steel I-Girders," *Journal of Structural Engineering*, Vol. 134, No. 9, pp. 1,425–1,436.

Wilson, J.M. (1886), "On Specifications for Strength of Iron Bridges," *Transactions ASCE,* Vol. 15, Part I, pp. 401–403, 489–490.

Yoo, C.H. and Lee, S.C. (2006), "Mechanics of Web Panel Postbuckling Behavior in Shear," *Journal of Structural Engineering*, Vol. 132, No. 1, pp. 1,580–1,589.

Ziemian, R.D. (2010), *Guide to Stability Design Criteria for Metal Structures*, 6th Ed., John Wiley & Sons, Hoboken, NJ.

Complementary Evaluation of Diagonal Tension Field Inclination Angle in Steel Plate Shear Walls

YUSHAN FU and MICHEL BRUNEAU

ABSTRACT

Complementarily to previous studies, research was conducted to investigate whether the equivalent constant angle of diagonal tension field action should be taken as either 40° or 45° for ductile steel plate shear walls (SPSW) designed per current codes. A two-dimensional finite element (FE) model was first calibrated against results from a prior study of "limited-ductility SPSW" by comparing effective stress contours and average angle of diagonal tension field action at different locations across the web plate. Then, this SPSW was redesigned as a ductile SPSW in compliance with the 2016 AISC *Seismic Provisions* (AISC, 2016a) to have fully restrained beam-to-column connections and analyzed using strip models and finite element models, respectively. The AISC moment-axial force interaction equation was used to compare demands in the SPSW boundary elements obtained from the strip and finite element models. With respect to the use of a single angle in design, it is shown that using an inclination angle of 45° is slightly (but not significantly) more conservative than using 40° as far as boundary element design is concerned. On the basis of these observations, along with findings from previous research on the diagonal tension field inclination angle, it is recommended that a single constant angle of either 40° or 45° be used for the design of SPSW.

Keywords: steel, plate, shear, wall, inclination angle, tension, field, LS-DYNA, seismic design, ductile design.

INTRODUCTION

Steel plate shear walls (SPSW) are one of the newest lateral load-resisting structural systems introduced in the AISC *Seismic Provisions* (AISC, 2005, 2010, 2016a), on the strength of extensive research in the past decades (e.g., Astaneh, 2004; Behbahanifard et al., 2003; Berman and Bruneau, 2004; Choi and Park, 2009; Driver et al., 1997a, 1997b; Elgaaly et al., 1993; Rezai, 1999; Roberts and Sabouri-Ghomi, 1992; Timler and Kulak, 1983; to name a few). These provisions address SPSW with unstiffened infill plates (i.e., plates functioning as webs) having large width-to-thickness ratios and relying on the development of inelastic diagonal tension field action to resist lateral loads and provide hysteretic energy dissipation during earthquakes. The orientation of the post-buckling principal stresses that develop in the infill plates of SPSW due to this tension-field action varies in a complex manner as a function of drift, location along boundary elements, and stages of inelastic behavior (Fu et al., 2017; Webster, 2013; Webster et al., 2014).

Pushover analysis of nonlinear, inelastic, finite element models can capture these variations as a function of drift and other SPSW properties, but this is not a practical tool for design. To simplify this complex behavior of SPSW in a manner suitable for design, Thorburn et al. (1983) proposed a strip model that replaces the infill plates with diagonal strips. In that model, at a given story, all the strips are oriented at the same angle from the vertical. In various editions of the AISC *Seismic Provisions* (and CSA S16) (see CSA, 2001, 2009, 2014), an equation has been provided to determine the angle to be used in the strip model; this equation was derived by Thorburn et al. (1983) [and later refined by Timler and Kulak (1983)] considering the relative elastic flexibility of boundary elements surrounding a panel. Using this equation typically leads to different angles used at the different stories along the height of an SPSW. To further simplify design, the AISC *Seismic Provisions* have allowed that a single angle could be used over the entire height (AISC, 2005). Initially, the provisions indicated that this value could be taken as equal to the average of all values calculated over the SPSW height; subsequently, using a constant angle of 40° was permitted, based on a study by Shishkin et al. (2005) described later.

Since then, other researchers have investigated whether using an equivalent constant angle of diagonal tension field action of 45° may be also appropriate for design as an alternative to the value of 40° currently permitted for ductile SPSW designed according to the current AISC *Seismic Provisions* and CSA S16 (2014). From a practicing engineer's perspective, using an angle of 45° is advantageous because it facilitates construction of the strip models for the SPSW. Past results, focusing on simplified one-story SPSW having

Yushan Fu, Graduate Research Assistant, Department of CSEE, University at Buffalo, Amherst, NY. Email: yushanfu@buffalo.edu (corresponding)

Michel Bruneau, Professor, Department of CSEE, University at Buffalo, Amherst, NY. Email: bruneau@buffalo.edu

a 1:1 aspect ratio (Webster, 2013; Webster et al., 2014), suggested that it would be appropriate; a subsequent study considering a number of code-compliant SPSW of different configurations, and comparing demands from the web plate on individual elements [Fu et al. (2017)] recommended using a constant angle of 45°. To answer the remaining question on this topic, the results presented here expand on this past research by investigating demands on the boundary elements of ductile SPSW designed according to the latest AISC *Seismic Provisions* requirements, by comparing results in terms of the complete system-induced demands in each members and using axial-bending interaction equation from AISC *Specification* Section H1.1 (AISC, 2016b).

More specifically, this paper first reviews the literature related to definition of the angle to use in SPSW strip models and then uses results from one of these studies to calibrate a finite element model to replicate past results and to investigate demands on the boundary elements of some ductile SPSW. Results obtained from finite element analysis and from strip models using either 40° or 45° are then compared to assess the significance of the differences.

LITERATURE REVIEW

The current AISC *Seismic Provisions* (2016a) and CSA S16 (2014) specify that the inclination angle of the diagonal tension field measured from the vertical can be calculated by the Equation 1 derived from elastic strain energy principles in Timler and Kulak (1983) as:

$$\tan^4 \alpha = \frac{1 + \dfrac{t_w L}{2A_c}}{1 + t_w h\left(\dfrac{1}{A_b} + \dfrac{h^3}{360 I_c L}\right)} \quad (1)$$

where
  A_b = cross-sectional area of the horizontal boundary element (HBE), in.^{2} (mm^2)
  A_c = cross-sectional area of the vertical boundary element (VBE), in.^{2} (mm^2)
  I_c = moment of inertia of the VBE, in.^{4} (mm^4)
  L = bay width, in. (mm)
  h = story height, in. (mm)
  t_w = thickness of the infill plate, in. (mm)

However, the fact that this equation was derived considering the elastic flexibility of a simplified subassembly is sometimes forgotten, and its complexity may inadvertently provide a disproportionate sense of accuracy, which is counter to the variations in actual angle observed in nonlinear analyses (specifically, those in the research summarized later).

Subsequently, Shishkin et al. (2005) suggested that a constant 40° angle could be used throughout by investigating the nonlinear behavioral effects of using various constant inclination angles on 1-story, 4-story, and 15-story SPSW strip models. These SPSW were designed to have an aspect ratio between 0.75 and 2.0, column flexibility factors (defined by the 2016 AISC *Seismic Provisions* Section F5.4a) ranging between 1.3 and 3.1, and either fully restrained (stated as being "rigidly connected" in the AISC *Seismic Provision* Commentary) or pinned beam-to-column connections (except for the 15-story SPSW, which were only considered with fully restrained moment-resisting connections), as part of a parametric study. Constant angles of 38° and 50°, permitted by CSA S16-01 (2001) were considered over the structure's height. Results showed that the angle of the tension strips had little impact on the predicted ultimate strength of an SPSW. Because the 38° models behaved somewhat more flexibly than the 50° models, the 40° value was recommended as a constant value for future designs. However, only the preceding two values of angles were considered for the strip models during the parametric studies, and comparisons focused on the ultimate strengths and initial stiffness of SPSW (without comparison against finite element results).

Later studies by Moghimi and Driver (2014a, 2014b) investigated a proposed alternative type of SPSW having moderately ductile behavior to be used in low seismic regions as a possible alternative to the existing SPSW in CSA S16-09 (having performance levels defined as "Type D" for "ductile plate walls" and "Type LD" for "limited ductility plate walls") and the 2010 AISC *Seismic Provisions* ("special plate shear walls"). One part of this study addressed the inclination angle of the diagonal tension field of a hypothetical four-story type LD SPSW designed per CSA S16 (2009). Results showed that the mean value of the angle α at the ultimate capacity of the wall (defined as occurring at 2.5% drift in that study) tended to be close to 39° and 51° adjacent to the beam [horizontal boundary element (HBE)] and compression column [vertical boundary element (VBE)], respectively. In addition, the effect of the minor principal compression stresses (σ_2) on demands for the boundary elements was investigated. It was observed that due to the von Mises yield criterion, the presence of σ_2 compression stresses led to an earlier tension yielding of the web plate around the boundary elements. It was reported that this simultaneously resulted in an increase of the forces applied (by the yielding infill) perpendicular to the boundary elements and a decrease of the forces applied parallel to the boundary elements. It was indicated that using 40° for the inclination angle, together with considering σ_2 and its effects on F_y and on the strip model, would provide acceptable and conservative results for the HBE, VBE, and web design. However, modifying the strip model this way, through determination

of σ_2 and considering the von Mises interaction, might be demanding from a practical perspective.

Webster et al. (2014) conducted both experimental and analytical analyses on two one-story SPSW having pinned HBE-to-VBE connections, slender VBEs, and cutouts at the web plate corners. The variation of the inclination angle of the diagonal tension field action acting in the SPSW was presented as a function of drift. By averaging the inclination angles over single panels, the mean was found to approach a value between 43° and 45°. For simplicity, use of a constant 45° angle was recommended by Webster et al. for capacity design procedure and cyclic analysis of SPSW systems. However, it was unknown how these findings would be affected when using moment-resisting HBE-to-VBE connections and how results would change for walls having different aspect ratios and number of stories.

To expand on the Webster et al. (2014) studies and to better understand how the inclination angles varied at different locations over the web plate and how this influenced demands of HBEs and VBEs for different SPSW configurations designed according to the AISC *Seismic Provisions*, Fu et al. (2017) investigated variations of the inclination angle in four AISC-compliant SPSW having aspect ratios of 1 and 2 and either one or three stories, using nonlinear, inelastic, finite element analysis. Similarly to what was reported by Moghimi and Driver (2014b), it was observed that the average inclination angles varied between 35° and 45° along the HBE and between 45° and 65° along the VBE. Beyond that, the inclination angles were also observed to vary as a function of drifts, panel aspect ratios, and numbers of stories.

For example, comparing results using a proposed combined moment-axial force ratio, it was shown that changing the aspect ratio had a significant impact on the level of conservatism obtained in respective three-story SPSW when comparing results for analyses using the same constant angles. As the number of stories increased, the ratios calculated for the top HBEs changed from being conservative to being unconservative, whereas observations for the tension VBEs were just the opposite. Using strips oriented at 35° and 40° for HBE design and 50° for VBE design were always found to be conservative. In the perspective that a single angle is used in modeling a SPSW, it was also observed that using a single angle of 45° provided a good compromise for both HBE and VBE design. Furthermore, because the demand on web plate is not sensitive to the variation of inclination angle, a single value of 45° was recommended for the design of the entire SPSW. However, in that study, calculation of combined moment-axial force ratio was done on an element basis, accounting for the stresses induced from the web plate but without consideration of force and moment interactions between HBEs and VBEs. This shortcoming is resolved by the research presented next.

MODEL CALIBRATION

Previous research in Fu et al. (2017) investigated the development of the diagonal tension field action and its orientation based on the calibration of the one-story SPSW experimentally and numerically studied in Webster et al. (2014), in order to match the variation of the average inclination angle over a single panel as a function of drift. That model was then modified to model AISC-compliant SPSW and used to perform the research described earlier. For the complementary work presented here and to broaden the validity of the findings in Fu et al., the numerical analyses began with calibration of an LS-DYNA model to replicate those from the limited-ductility, four-story SPSW designed with pinned beam-to-column connections and analyzed using ABAQUS by Moghimi and Driver (2014b), for which the distribution of inclination angle over the entire web plate was provided. This was done because that study is the only one advocating the use of the 40° angle for which finite element analyses were conducted. Then, after comparison of the results showed the LS-DYNA to match those reported by Moghimi and Driver (2014b), the LS-DYNA model was modified to have fully restrained HBE-to-VBE connections in compliance with the current AISC seismic design specifications. Note that line elements were used here for the HBEs and VBEs in the LS-DYNA model to be consistent with the approach used by Moghimi and Driver (2014b). Then, two strip models were constructed using SAP2000: one with strip inclination angle of 40° and one with 45°. To account for the actual demands of the HBEs and VBEs, forces and moments were output directly from LS-DYNA and SAP2000 for comparison, and the AISC moment-axial force interaction equation was used to evaluate the conservatism of the resulting demands for the HBE and VBE design. Details of these analyses are presented next.

Dimensions and Boundary Conditions

The finite element model, developed using LS-DYNA, for the limited-ductility, four-story SPSW studied by Moghimi and Driver (2014b) is presented in Figure 1. The bay width of the SPSW is 236.22 in. (6000 mm), and the story heights are 165.35 in. (4200 mm) and 145.67 in. (3700 mm) for the first story and the other three stories, respectively. The sections designed according to the AISC *Seismic Provisions* (2010) for the fourth-story and second-story HBEs are W24×306 and W12×190, respectively, while W10×100 are used for both the first-story and third-story HBEs. A built-up VBE having 19.69-in. × 0.79-in. (500 mm × 20 mm) flanges and 19.69-in. × 1.97-in. (500 mm × 50 mm) web was used. The base of the wall was modeled to be continuously fixed. The thicknesses of the web plates were 0.19 in. (4.8 mm) for the third and fourth stories and 0.25 in. (6.4 mm) for the first and second stories.

Material and Element

Similarly to what was done with the ABAQUS modeling in Moghimi and Driver (2014b), the four-node Belytschko-Tsay shell element was chosen for the web plate, and the Hughes-Liu beam element with 15 cross-section integration points was selected for the HBEs and VBEs. The HBEs were pin-connected to the adjacent VBEs by releasing the in-plane rotation at the HBE ends, as shown in Figure 1. The web plates were extended to the edge of the surrounding boundary elements to account for offsets in the connection points, and each node at the edge of web plates was constrained to the corresponding node on the centerline of the boundary element in its six degrees of freedom (DOF) through NODAL_RIGID_BODY_SPC. The out-of-plane translational and rotational DOF of the nodes along HBEs and VBEs were fixed. An elastic-plastic constitutive model without strain hardening was specified for the steel web plate using MAT024_PIECEWISE_LINEAR_PLASTICITY. Boundary elements were modeled with an elastic-plastic

model having 1% isotropic strain hardening, defined using MAT003-PLASTIC-KINEMATIC_ISOTROPIC HARDENING. The specified material had a Young's modulus of 29,008 ksi (200,000 MPa), a yielding strength of 55.84 ksi (385 MPa), a Poisson ratio of 0.30, and a density of 490.06 lb/ft^3 (7850 kg/m^3).

Loading Protocol

In order to achieve the same roof drift at which the average inclination angle was reported in Moghimi and Driver (2014b), a horizontal force of 472 kip (2100 kN) was first applied at the right HBE end of each story using force control until the converge failure occurred (typically when 0.2% roof drift was reached). The nodal displacements at the right HBE ends on the last step of that analysis were output and then applied proportionally using displacement control up to 2.5% roof drift. These results obtained from the LS-DYNA model using displacement control at 2.5% roof drift are compared with the Moghimi and Driver results next.
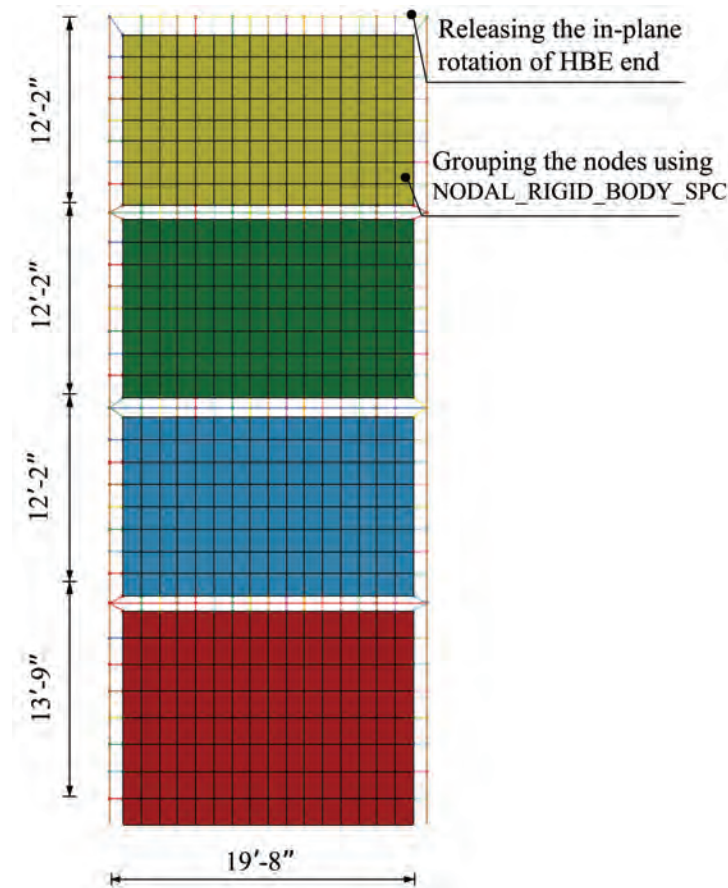

Fig. 1. Dimensions and constraints of four-story, limited-ductility SPSW.

RESULTS FROM CALIBRATION

Von Mises Stress and Effective Plastic Strain Contour

The von Mises contour and principal stress vector presented in Figure 2 show that all the web plates yielded at 1.9% roof drift. Subsequently, plotted in Figure 3 are the effective strain contours at the roof drifts of 1.9% and 2.5%, respectively. For comparison, Figure 3(c) shows the effective plastic strain contour at 2.5% drift from Moghimi and Driver (2014b); the contours and magnitude of the effective plastic strains obtained from both models are in good agreement in capturing the behavior of the limited-ductility SPSW. It also illustrates that the distribution of effective strains in that system is more severe and concentrated near the right VBE, which is different from the more uniform strain distribution that develops across the entire web of ductile SPSW designed according to the 2016 AISC *Seismic Provisions*.

Inclination Angle Analysis

From the preceding finite element analysis, the inclination angle was calculated from the resulting in-plane stresses for each shell element considered. Focusing on the areas of interest here, the inclination angle of the diagonal tension field was averaged along the HBEs and VBEs, as well as along the mid-web region used in Moghimi and Driver

(2014b). Figure 4 shows that all the curves vary extensively as a function of drift [consistently to what was reported by Fu et al. (2017)] and tend to converge at 2.5% roof drift, as the average inclination angle approached 40° for the HBE, 52° for the VBE, and 47° at the middle of the web.

INCLINATION ANGLE FOR DUCTILE SPSW

Ductile SPSW in Compliance with the AISC *Seismic Provisions*

To investigate the effects of the inclination angle used in the strip models for the design of ductile SPSW, the preceding SPSW was redesigned to have fully restrained HBE-to-VBE connections in compliance with the AISC *Seismic Provisions* (AISC, 2016a) and using the constant angle of 40°. HBEs and VBEs were designed to resist combined flexure and axial compression. The HBE was sized to resist forces determined from the capacity design procedure, while the VBEs were selected based on results of the pushover analyses conducted in SAP2000. Figure 5 illustrates the two kinds of pushover analyses conducted for this purpose. The selection of the load patterns adopted in this research was inspired by Krawinkler and Seneviratna (1998), who showed that no unique load pattern in pushover analysis is capable of bounding the distribution of inertia forces in a design earthquake, especially in the perspective of inelastic deformations. Using

(a)

(b)
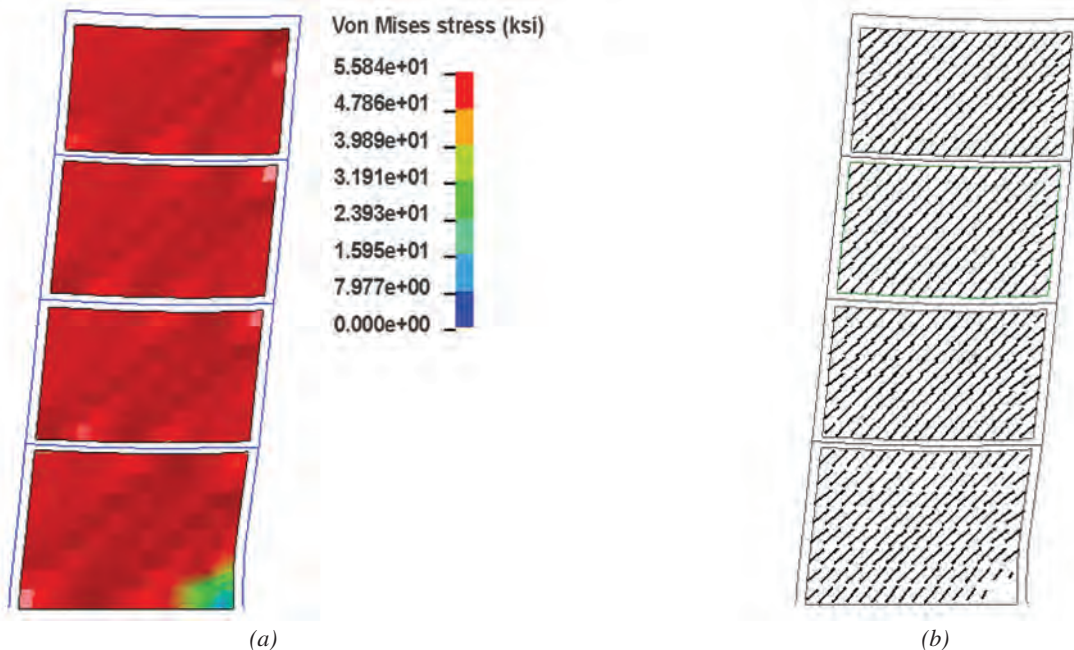
Fig. 2. Von Mises stress contour and principal stress vector: (a) von Mises contour at yield mechanism (1.9% drift) from LS-DYNA model (displacement scale factor = 5); (b) principal stress vector at yield mechanism from LS-DYNA model (displacement scale factor = 5 and vector scale factor = 0.2).

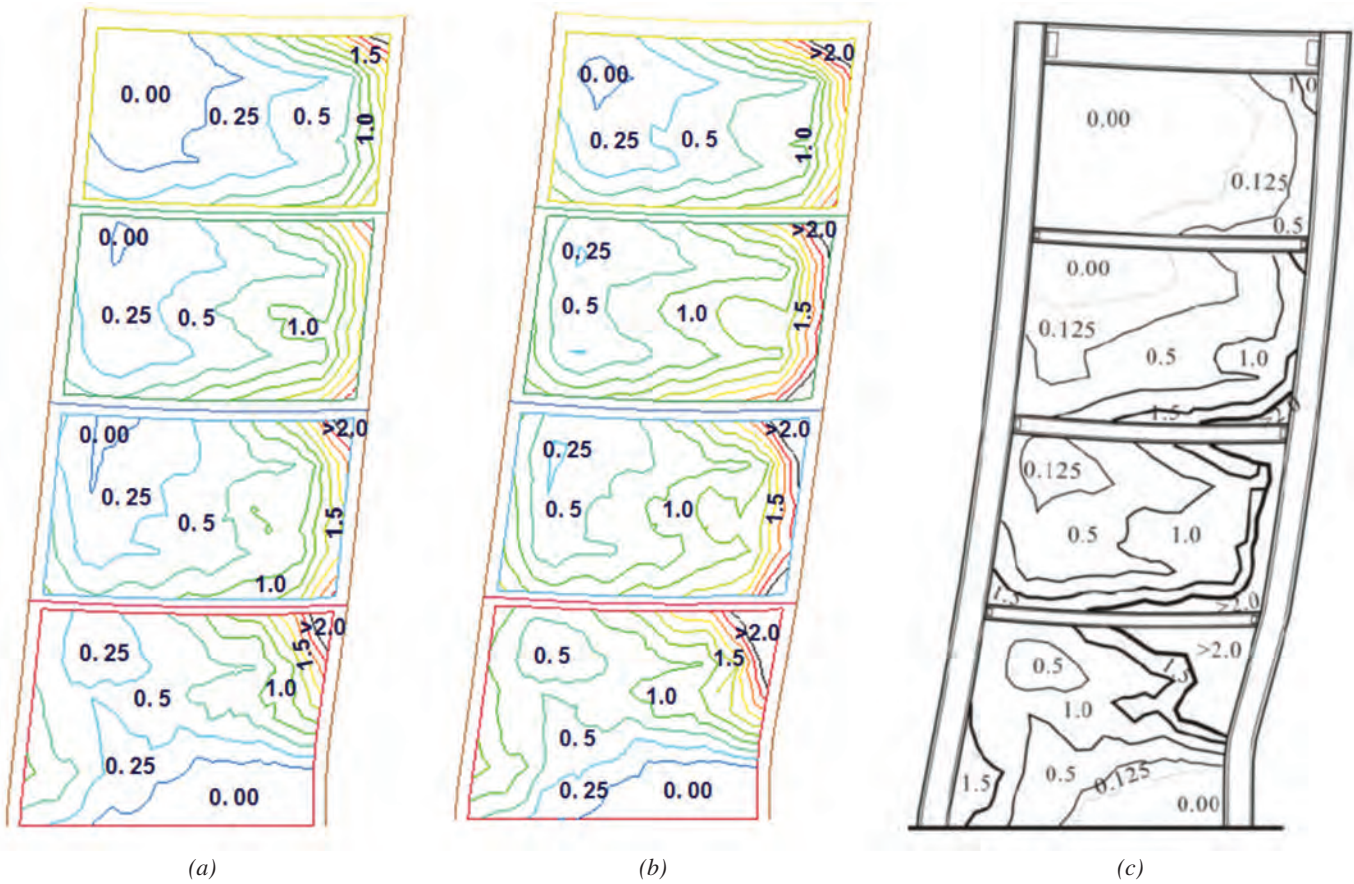*Fig. 3. Comparison on effective plastic strain contours: (a) effective plastic strain contour at yield mechanism (1.9% drift) from LS-DYNA model (%, displacement scale factor = 5); (b) effective plastic strain contour at 2.5% drift from LS-DYNA model (%, displacement scale factor = 5); (c) effective plastic strain contour at 2.5% drift from Moghimi and Driver (2014b) (%).*
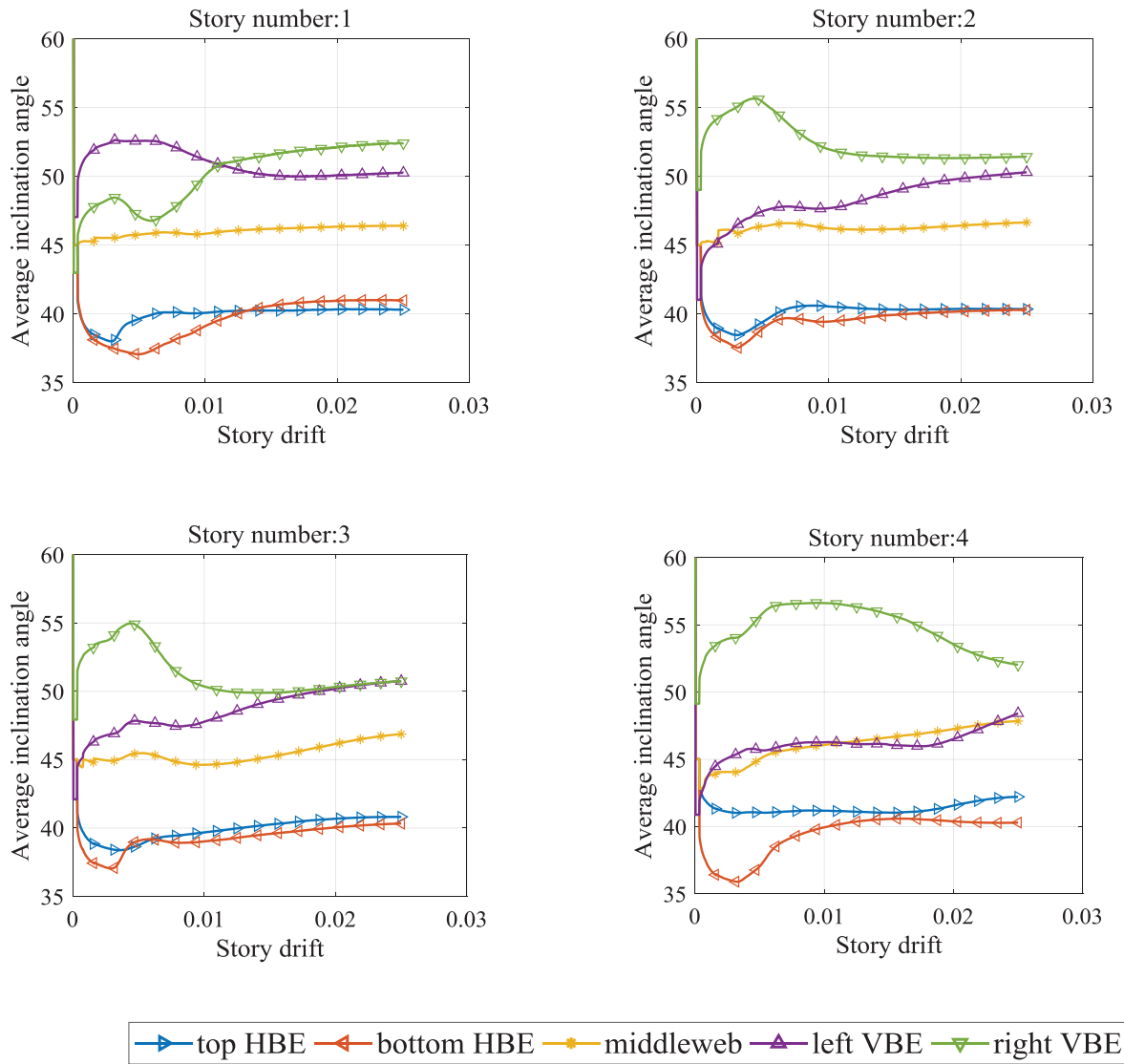
Fig. 4. Inclination angle variation.

different load patterns allows for investigating the variation of the inclination angle under those conditions as drift increases and for examining the conservativeness of using a constant angle over the structure height in such cases. Therefore, two recommended load patterns—namely, a uniform distribution of load and an inverted triangular load—were applied here. In the former case, a horizontal force of 400 kips (1779 kN) was applied at each end of the HBEs; plastic hinges were observed to have developed at the ends of all HBEs and at the base of the VBEs when displacement at the mid-point of the fourth-story HBE reached 2.5% roof drift. In the latter case, the load pattern was achieved by applying an increasing unidirectional ground acceleration until the mid-point of the fourth-story HBE reached 2.5% roof drift and the same yield mechanism was observed to have occurred. Hereafter, the SAP2000 models designed with constant angle of α and subjected to either uniform distribution or inverted triangular forces are referred to as SP-α-U and SP-α-T, respectively. Note that for the HBEs to which the web plates above and below have the same thickness (namely, the first and third HBEs in this example), design was governed by axial demands as well as by the requirement that the moment-resisting frame alone be able to carry at least 25% of the seismic base shear, which was verified by using a SAP2000 model of the bare frame consisting of the HBEs and VBEs alone.

SAP2000 Modeling of Ductile SPSW

The constitutive models used for the boundary elements and strips in the SAP2000 models were the same as those in the calibrated LS-DYNA model (described earlier). Fourteen strips were selected for each story for all the strip models. The nonlinear behavior of the tension-only-strip was achieved by applying a compression limit on the strip and releasing the rotational DOF at the strip ends. Plastic hinges were defined using P-M2-M3 hinges at both ends of each HBE and VBE to capture their nonlinear behavior.

For the redesigned SPSW, the resulting fourth-story to first-story HBEs (top to bottom) were W40×397, W12×170, W33×241, and W12×170, respectively. A single built-up VBE cross section was used along the height, with a depth d = 44.52 in. (1130.70 mm), flange width b_f = 19.33 in. (491.05 mm), flange thickness t_f = 3.89 in. (98.91 mm), and web thickness t_w = 2.17 in. (55.04 mm).

LS-DYNA Modeling of Ductile SPSW

The ductile SPSW was similarly modeled using the calibrated LS-DYNA model mentioned earlier but with some differences in the constraint, mesh and loading protocols. First, fully restrained HBE-to-VBE connections were achieved by fixing the in-plane rotation at the HBE ends. In order to capture the behavior of plastic hinges, the size of

the mesh at the HBE and VBE ends was determined based on the results from a separate study on a cantilever column, comparing the difference between base moments obtained from LS-DYNA and SAP2000. In addition, 27 integration points (nine points for each flange and nine points for the web) were applied on the beam element cross-section, as a refinement from the 15 used previously.

Comparison of Results from Finite Element Analysis and Strip Models

The SPSW designed in compliance with the 2016 AISC *Seismic Provisions* (as described earlier) was analyzed using both the LS-DYNA model described in the previous section and SAP2000 models having strips oriented at the same angle throughout (one analysis with strips at 40° and one analysis with strips at 45°). To be able to compare the results obtained using the strip models with the ones obtained using the finite element, the displacement histories obtained from SP-40°-U, SP-40°-T, SP-45°-U and SP-45°-T, in addition to the lateral loads, were applied to the corresponding LS-DYNA models, as described in Figure 5.

The appropriateness of demands from modeling using 40° and 45° in the strip model was evaluated by comparing the demands on the HBEs and VBEs obtained from SAP2000 with the corresponding demands from LS-DYNA. For this purpose, the demands obtained by considering the 2016 AISC *Specification* combined moment-axial force interaction equation were compared. For large axial load ($P_{FE}/P_{CD} \geq 0.2$), this was effectively achieved by calculating the following ratio:

$$\frac{\dfrac{8}{9}\left(\dfrac{M_{FE}}{M_{CD}}\right) + \dfrac{P_{FE}}{P_{CD}}}{\dfrac{8}{9}\left(\dfrac{M_{strip_\alpha}}{M_{CD}}\right) + \dfrac{P_{strip_\alpha}}{P_{CD}}} \qquad (2)$$

where P_{FE} and M_{FE} are forces and moments obtained from LS-DYNA, P_{CD} and M_{CD} are axial and flexural strength of the frame members, and P_{strip_α} and M_{strip_α} are forces and moments obtained from SAP2000 designed using α = 40° in one case and α = 45° in the other. The inclination angle used for the design is deemed to give conservative results compared to finite element results when the preceding combined moment-axial force demand ratio is less than or equal to 1. Furthermore, for the design to be deemed satisfactory, the ratios from the individual interaction equations in the numerator and denominator must also respectively give results less than or equal to 1.

Tables 1 and 2 present the combined moment-axial force demand ratios calculated for the HBEs, left VBE, and right VBE at each story, denoting the left and right end of the HBE as HBEL and HBER and the top and bottom of the VBE as VBET and VBEB. The ratios of (FE/CD) and (Strip/

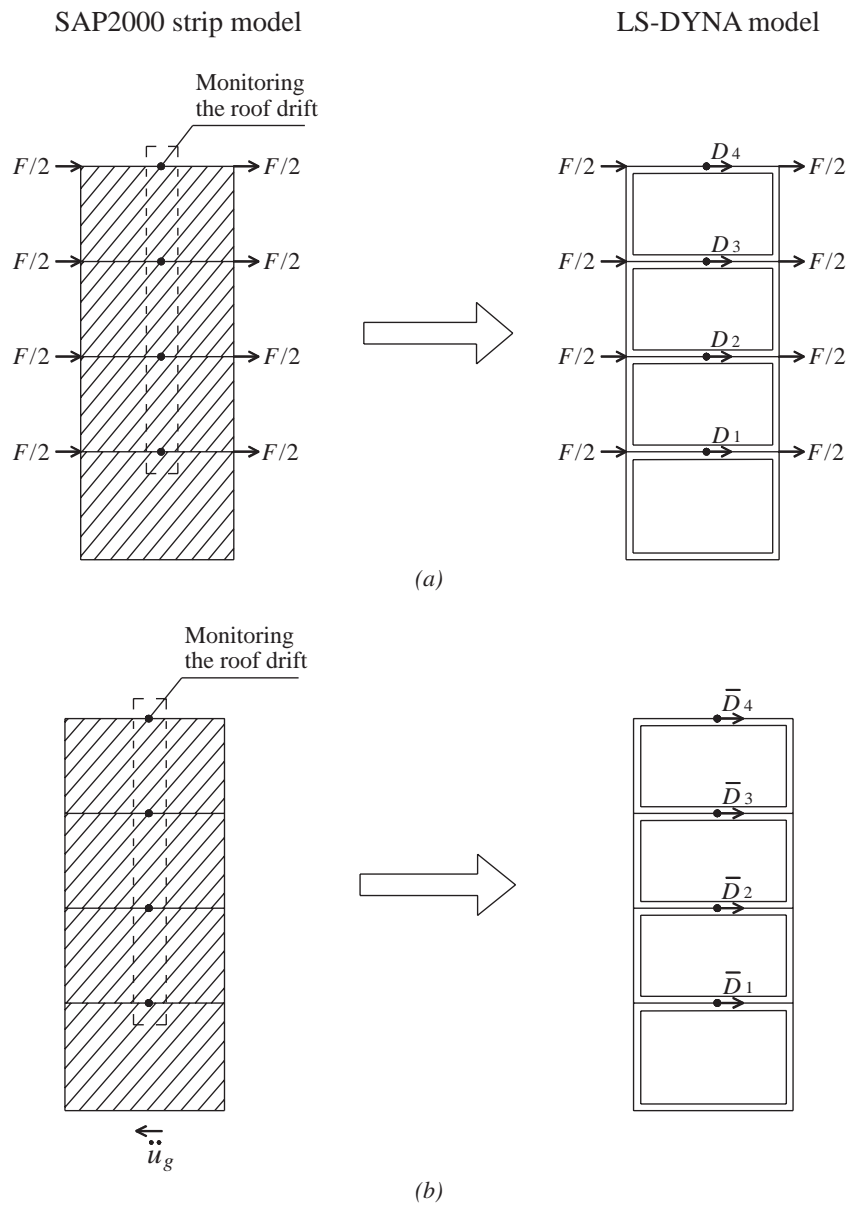SAP2000 strip model   LS-DYNA model

(a)

(b)

Fig. 5. Loading approaches for pushover analyses in SAP2000 and LS-DYNA: (a) uniform distribution of force; (b) inverted triangular force. D and $\overline{D}$ refer to displacement histories from SAP2000 model subjected to uniform distribution of force (SP-40°-U and SP-45°-U) and inverted triangular force (SP-40°-T and SP-45°-T), respectively.

Table 1. Combined Moment-Axial Demand Ratio of the SPSW Subjected to Pushover Analysis Using Uniform Lateral Load (Comparing SP-40°-U and SP-45°-U with the LS-DYNA Model Subjected to the Pushover Displacements and Loads from SP-40°-U)

	Location	4th HBEL	4th HBER	3rd HBEL	3rd HBER	2nd HBEL	2nd HBER	1st HBEL	1st HBER
HBE	$Rb\_40°$	1.08	0.91	0.91	0.94	0.92	0.91	0.83	0.94
	FE/CD	0.83	0.84	0.87	0.89	0.97	0.90	0.86	0.97
	Strip/CD	0.77	0.92	0.96	0.95	1.06	0.99	1.05	1.04
	$Rb\_45°$	1.12	0.91	0.87	0.90	0.91	0.89	0.82	0.92
	FE/CD	0.83	0.84	0.87	0.89	0.97	0.90	0.86	0.97
	Strip/CD	0.74	0.92	1.00	0.98	1.07	1.02	1.06	1.06
	Location	4th VBET	4th VBEB	3rd VBET	3rd VBEB	2nd VBET	2nd VBEB	1st VBET	1st VBEB
VBE (L)	$RcL\_40°$	1.22	0.99	1.02	0.88	0.94	1.19	1.25	1.00
	FE/CD	0.38	0.44	0.51	0.32	0.55	0.30	0.38	1.10
	Strip/CD	0.31	0.44	0.50	0.37	0.58	0.25	0.30	1.10
	$RcL\_45°$	1.28	1.02	1.07	0.86	0.92	1.07	1.18	0.99
	FE/CD	0.38	0.44	0.51	0.32	0.55	0.30	0.38	1.10
	Strip/CD	0.30	0.43	0.47	0.37	0.59	0.28	0.32	1.11
	Location	4th VBET	4th VBEB	3rd VBET	3rd VBEB	2nd VBET	2nd VBEB	1st VBET	1st VBEB
VBE (R)	$RcR\_40°$	0.91	0.88	0.91	1.00	0.98	1.12	1.10	1.02
	FE/CD	0.48	0.55	0.62	0.46	0.72	0.43	0.50	1.12
	Strip/CD	0.53	0.63	0.69	0.46	0.73	0.39	0.46	1.10
	$RcR\_45°$	0.93	0.84	0.87	0.94	0.94	1.04	1.03	1.02
	FE/CD	0.48	0.55	0.62	0.46	0.72	0.43	0.50	1.12
	Strip/CD	0.52	0.66	0.72	0.49	0.76	0.42	0.48	1.10

CD) refer to the values calculated from the nominator and denominator of Equation 2, respectively, while the Rx_α illustrates the resulting ratio from Equation 2 in certain locations (where X is replaced by b, cL and cR to represent the beam, left column, and right column, respectively) using the constant angle α for the strip model. Note that only the results obtained from LS-DYNA models subjected to SP-40°-U and SP-40°-T pushover displacements and loads are presented in Tables 1 and 2 because similar results were obtained when using the LS-DYNA models subjected to those from the 45° cases. As can be seen from the ratios for HBEs, in most of the cases (except for the left end of the fourth-story HBE),

using the inclination angle of 45° for design is slightly (but not significantly) more conservative than using 40°; more specifically, compared to results from finite element analysis, demands from forces obtained from the strip model are, on average, 1.3% larger when using 45° as inclination of the strips instead of 40°. Similar observations are obtained for the right VBEs, with results being, on average, 3.7% larger when using 45° instead of 40°. With respect to the left VBEs, although using the angle of 45° is shown to be more conservative only for the third and lower stories, the web in the fourth story was found to be incompletely yielded because the same cross-section was used for all columns.

| Table 2. Combined Moment-Axial Demand Ratio of the SPSW Subjected to Pushover Analysis Using Inverted-Triangular Lateral Load (Comparing SP-40°-T and SP-45°-T with the LS-DYNA Model Subjected to the Pushover Displacements from SP-40°-T)									
HBE	Location	4th HBEL	4th HBER	3rd HBEL	3rd HBER	2nd HBEL	2nd HBER	1st HBEL	1st HBER
	$Rb\_40°$	1.14	0.97	0.84	1.02	0.83	1.00	0.70	0.95
	FE/CD	0.71	0.84	0.73	0.95	0.87	1.00	0.73	0.99
	Strip/CD	0.62	0.87	0.86	0.93	1.04	1.01	1.04	1.04
	$Rb\_45°$	1.21	1.00	0.79	0.97	0.82	0.97	0.69	0.93
	FE/CD	0.71	0.84	0.73	0.95	0.87	1.00	0.73	0.99
	Strip/CD	0.58	0.85	0.92	0.98	1.06	1.04	1.05	1.06
VBE (L)	Location	4th VBET	4th VBEB	3rd VBET	3rd VBEB	2nd VBET	2nd VBEB	1st VBET	1st VBEB
	$RcL\_40°$	1.34	1.00	1.05	0.94	0.98	1.13	1.18	1.00
	FE/CD	0.34	0.46	0.53	0.39	0.62	0.34	0.42	1.10
	Strip/CD	0.25	0.46	0.51	0.41	0.63	0.30	0.35	1.10
	$RcL\_45°$	1.44	1.06	1.12	0.94	0.98	1.05	1.14	0.99
	FE/CD	0.34	0.46	0.53	0.39	0.62	0.34	0.42	1.10
	Strip/CD	0.24	0.43	0.47	0.42	0.64	0.33	0.37	1.11
VBE (R)	Location	4th VBET	4th VBEB	3rd VBET	3rd VBEB	2nd VBET	2nd VBEB	1st VBET	1st VBEB
	$RcR\_40°$	0.93	0.89	0.92	1.05	1.00	1.11	1.07	1.02
	FE/CD	0.48	0.58	0.64	0.53	0.78	0.48	0.53	1.13
	Strip/CD	0.51	0.65	0.70	0.51	0.79	0.43	0.50	1.10
	$RcR\_45°$	0.97	0.85	0.88	0.98	0.97	1.04	1.01	1.02
	FE/CD	0.48	0.58	0.64	0.53	0.78	0.48	0.53	1.13
	Strip/CD	0.49	0.68	0.73	0.54	0.81	0.46	0.53	1.10

Comparison of the Forces and Moments Obtained from SAP2000 and LS-DYNA

As noticed in Tables 1 and 2, in most cases, the FE/CD ratios are smaller than the Strip/CD ones, except for some of the ratios in the first and fourth stories. To investigate possible causes for these differences in the FE/CD and Strip/CD ratios, results obtained from the SP-40°-U and SP-45°-U analyses were further compared with those from the LS-DYNA model subjected to pushover displacements and loads corresponding to SP-40°-U. For this purpose, forces and moments acting on the boundary elements at the fourth story are compared in Figure 6, more specifically focusing on the possible role of (as described later) (1) the incomplete yielding of infill at the fourth floor, as revealed by the nonyielded strips near the corners of the infill in the applied parallel and normal force diagrams in Figure 6; (2) the small discrepancy in the displacements obtained in the LS-DYNA model compared to the SAP2000 model as indicated in the axial force plot of Figure 6(a); and (3) the σ_2 effects included in the LS-DYNA model and variation of the inclination angle along the boundary elements.

The applied parallel forces obtained from the SAP2000 strip model indicate that some strips near the top-right and bottom-left corners in the fourth story did not completely yield. To assess the effects of this incomplete infill yielding on the preceding findings, a separate analysis was conducted in which all the strips in the SAP2000 model were removed and replaced by forces of orientation and magnitude equivalent to what would have been developed by the strips had they all been yielded; these results correspond
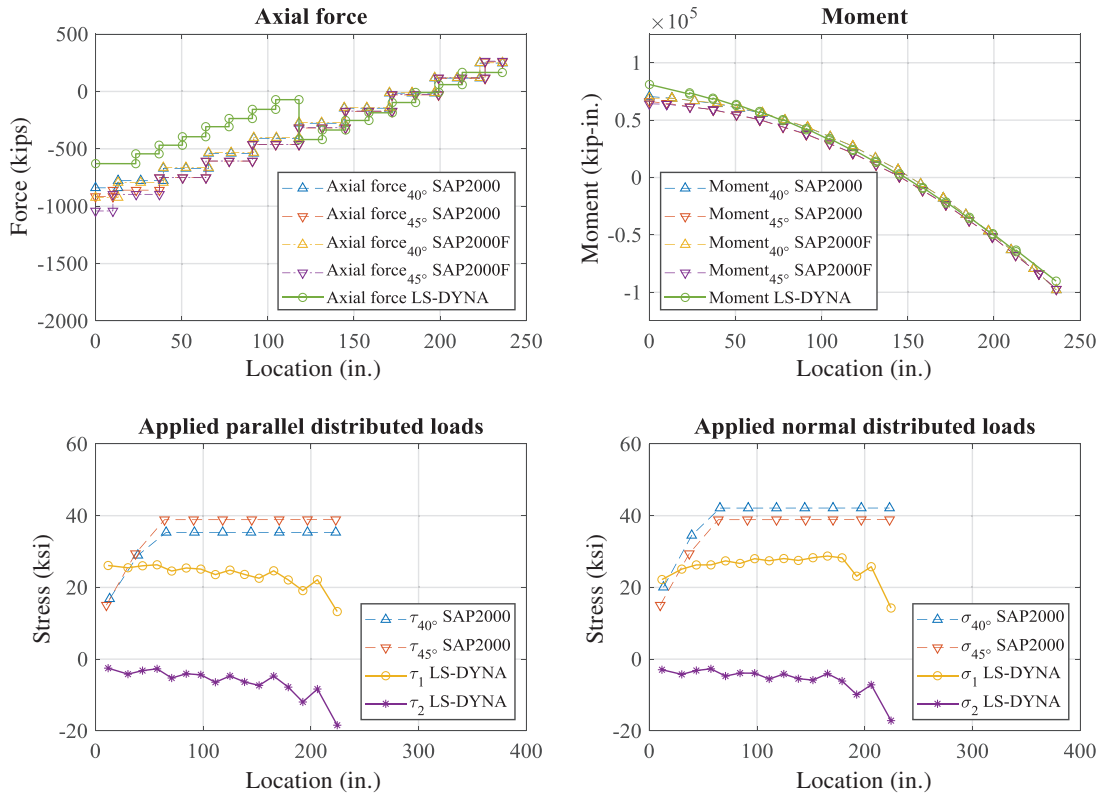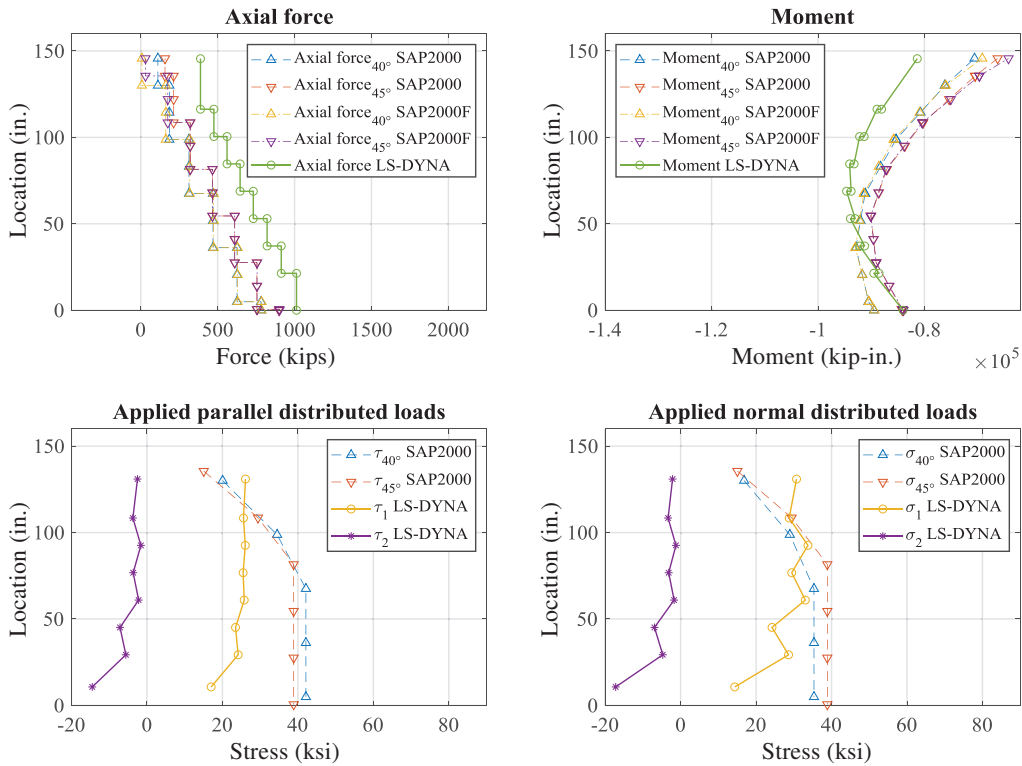
Fig. 6 (a-b). Comparison of forces obtained from the fourth-story boundary elements
in SAP2000 and LS-DYNA: (a) the fourth-story HBE; (b) the fourth-story left VBE.

to the case labeled SAP2000F in Figure 6. Comparing the resulting curves to those obtained from the original strip models, denoted by SAP2000, it is observed that the force and moment diagrams near the corners for the completely and incompletely yielded strip cases are slightly different but that this difference alone merely makes up, at most, a 5% difference between the strip model and the LS-DYNA model in terms of combined axial-moment demand ratio.

The discrepancy on the displacements between the LS-DYNA and SAP2000 models was investigated next. Given the high stiffness of SPSW, a small discrepancy in displacement histories between the SAP2000 strip model and LS-DYNA model is equivalent to applying significant forces at those locations in the FE model. For instance, the discrepancy in displacements between the strip models (SP-40°-U and SP-45°-U) and the LS-DYNA model subjected to the SP-40°-U pushover displacement and loads resulted in a difference in axial force at the fourth HBE's left end of 25.1%, when compared to the strip model using an angle of 40°, and of 31.4%, when compared to the strip model using 45°, as shown in Figure 6(a). Because the combined moment and axial force ratio of this HBE is dominated

by the moment term, this eventually led to a net 8% and 12% difference in the ratios per Equation 2 when compared to the results otherwise obtained for the 40°-strip model and 45°-strip model, respectively.

In order to study the influence of the σ_2 effects included in the LS-DYNA model, and the variation of the inclination angle along the boundary elements, the resulting axial forces of the right VBE in the fourth story from the preceding SAP2000 equivalent strip models were compared with those from the LS-DYNA model subjected to SP-40°-U pushover displacements and loads. This is because the difference in axial force diagram accumulated from top to bottom is only due to the σ_2 effects and to the variation in inclination angle along the VBE. By summing up the applied forces parallel to the right VBE, the results from the FE model were found to be less than those obtained from the 45°-strip model by 3.4% and less than the 40°-strip model by 12%.

Although the difference in axial force and moment obtained from SAP2000 and LS-DYNA models was found to be attributed to all of the preceding factors, the demand-to-strength ratios calculated from SAP2000 (denominators) are still comparable to those from LS-DYNA (numerators).
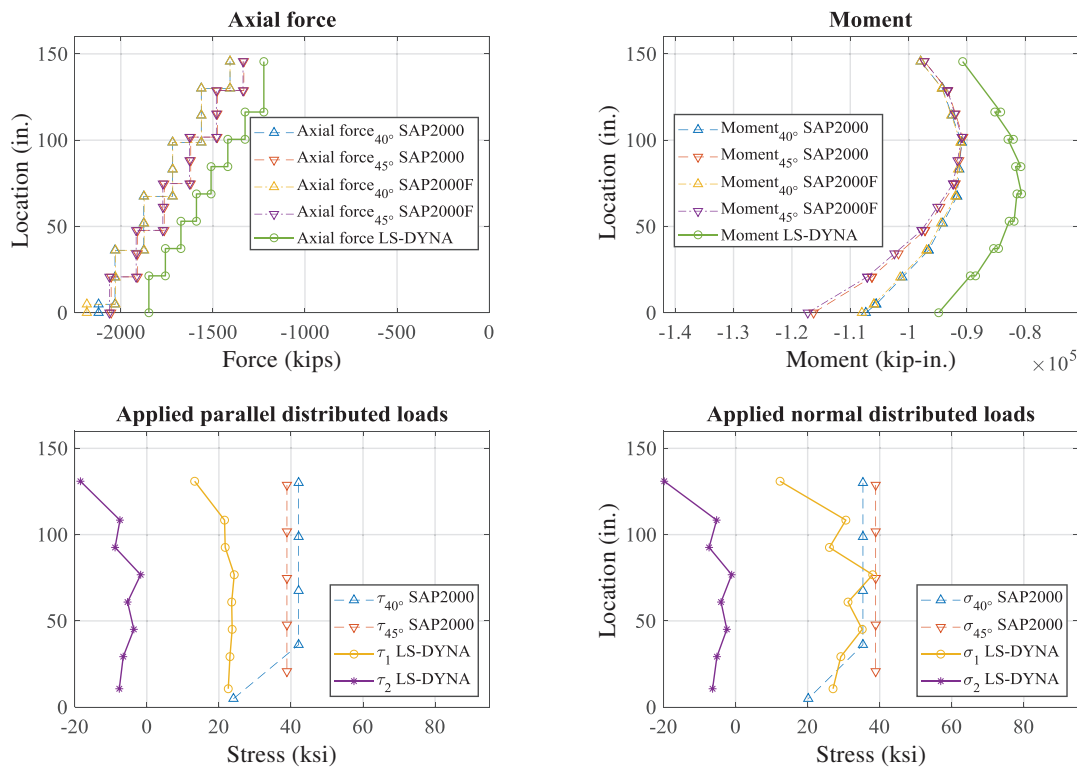
(c)

Fig. 6 (c). Comparison of forces obtained from the fourth-story boundary elements in SAP2000 and LS-DYNA: (c) the fourth-story right VBE. Subscripts "1" and "2" in applied-distributed-loads diagrams represent the maximum principal stress and minimum principal stress obtained from LS-DYNA, respectively.

It is also found that using the inclination angle of 45° is slightly (but not significantly) more conservative than using 40° for boundary element design of the SPSW. Effectively, either 40° or 45° could be used for design.

CONCLUSION

This study expanded on and complemented prior research to determine whether a constant angle of 40° or 45° should be used for the orientation of the tension field action considered in ductile SPSW designed in compliance with the current edition of the AISC *Seismic Provisions* (and of CSA S16). A finite element model was first constructed to replicate a prior study of limited-ductility SPSW, comparing effective stress contours and the average angle of diagonal tension field action at different locations across the web plate. Then, this SPSW was redesigned to have fully restrained beam-to-column connections in compliance with the AISC *Seismic Provisions*, and the finite element model was similarly modified. Pushover analysis results from the finite element model were compared with those obtained from two corresponding strip models analyzed using constant angles of 40° and 45°, respectively. By calculating demands on boundary elements using the AISC moment-axial interaction equation, it was found that using an inclination angle of 45° is slightly (but not significantly) more conservative than using 40° in terms of forces applied to the boundary element of the SPSW. On the basis of these findings, as well as those from previous research investigating the diagonal tension field inclination angle in SPSW, it is found that either 40° or 45° could be effectively used for design of the entire SPSW.

FUTURE RESEARCH

While a limited number of SPSW have been considered here, the previous study by Fu et al. (2017) also showed that 45° was adequate on the basis of demands on VBEs and HBEs on an element-by-element basis due to stresses induced from the web plate only. That prior study considered SPSW having different aspect ratios and number of stories. The more rigorous comparison of true boundary elements forces performed here shows that even when considering the fact that demands on HBEs also affect demands on VBEs (due to shear and axial forces transferred at the ends of HBEs), the recommendation to use 45° remains valid. While the authors are comfortable with this recommendation, future research could investigate the sensitivity of this condition for taller SPSW or other geometries.

REFERENCES

AISC (2005), *Seismic Provisions for Structural Steel Buildings*, ANSI/AISC 341-05, American Institute of Steel Construction, Chicago, IL.

AISC (2010), *Seismic Provisions for Structural Steel Buildings*, ANSI/AISC 341-10, American Institute of Steel Construction, Chicago, IL.

AISC (2016a), *Seismic Provisions for Structural Steel Buildings*, ANSI/AISC 341-16, American Institute of Steel Construction, Chicago, IL.

AISC (2016b), *Specification for Structural Steel Buildings*, ANSI/AISC 360-16, American Institute of Steel Construction, Chicago, IL.

Astaneh-Asl, A. (2001), "Seismic Behavior and Design of Steel Shear Walls," Steel Technical Information and Product Services Report, Structural Steel Educational Council, Moraga, CA.

Behbahanifard, M., Grondin, G. and Elwi, A. (2003), "Experimental and Numerical Investigation of Steel Plate Shear Walls," Structural Engineering Report No. 254, Department of Civil and Environmental Engineering, University of Alberta, Edmonton, AB, Canada.

Berman, J.W. and Bruneau, M. (2004), "Steel Plate Shear Walls Are Not Plate Girders," *Engineering Journal*, AISC, Vol. 41, No. 3, pp. 95–106.

CSA (2001), *Limit States Design of Steel Structures*, CAN/CSA S16-01, Canadian Standards Association, Toronto, ON, Canada.

CSA (2009), *Design of Steel Structures*, CAN/CSA S16-09, Canadian Standards Association, Toronto, ON, Canada.

CSA (2014), *Design of Steel Structures*, CAN/CSA S16-14, Canadian Standards Association, Toronto, ON, Canada.

Choi, I.R. and Park, H.G. (2009), "Steel Plate Shear Walls with Various Infill Plate Designs," *Journal of Structural Engineering*, ASCE, Vol. 135, No. 7, pp. 785–796.

Driver, R.G., Kulak, G.L., Kennedy, D.J.L. and Elwi, A.E. (1997a), "Seismic Behaviour of Steel Plate Shear Walls," Structural Engineering Report No. 215, Department of Civil Engineering, University of Alberta, Edmonton, AB, Canada.

Driver, R.G., Kulak, G.L., Kennedy, D.J.L. and Elwi, A.E. (1997b), "Finite Element Modelling of Steel Plate Shear Walls," *Proceedings of the Structural Stability Research Council Annual Technical Session*, Toronto, ON, Canada, pp. 253–264.

Elgaaly, M., Caccese, V. and Du, C. (1993), "Post-Buckling Behavior of Steel-Plate Shear Walls under Cyclic Loads," *Journal of Structural Engineering*, ASCE, Vol. 119, No. 2, pp. 588–605.

Fu, Y., Wang, F. and Bruneau, M. (2017), "Diagonal Tension Field Inclination Angle in Steel Plate Shear Walls," *Journal of Structural Engineering*, ASCE, Vol. 143, No. 7.

Krawinkler, H. and Seneviratna, G.D.P.K. (1998), "Pros and Cons of a Pushover Analysis of Seismic Performance Evaluation," *Engineering Structures*, Vol. 20, Nos. 4–6, pp. 452–464.

Moghimi, H. and Driver, R.G. (2014a), "Performance-Based Capacity Design of Steel Plate Shear Walls. I: Development Principles," *Journal of Structural Engineering*, ASCE, Vol. 140, No. 12.

Moghimi, H. and Driver, R.G. (2014b), "Performance-Based Capacity Design of Steel Plate Shear Walls. II: Design Provisions," *Journal of Structural Engineering*, ASCE, Vol. 140, No. 12.

Rezai, M. (1999), "Seismic Behavior of Steel Plate Shear Walls by Shake Table Testing," Ph.D. Dissertation, Department of Civil Engineering, University of British Columbia, Vancouver, BC, Canada.

Roberts, T.M. and Sabouri-Ghomi, S. (1992), "Hysteretic Characteristics of Unstiffened Perforated Steel Plate Shear Walls," *Thin-Walled Structures*, Vol. 14, No. 2, pp. 139–151.

Shishkin, J.J., Driver, R.G. and Grondin, G.Y (2005), "Analysis of Steel Plate Shear Walls Using the Modified Strip Model," Structural Engineering Report No. 261, Department of Civil and Environmental Engineering, University of Alberta, Edmonton, AB, Canada.

Timler P.A. and Kulak, G.L. (1983), "Experimental Study of Steel Plate Shear Walls," Structural Engineering Report No. 114, Department of Civil Engineering, University of Alberta, Edmonton, AB, Canada.

Thorburn, L.J., Kulak, G.L. and Montgomery, C.J. (1983), "Analysis of Steel Plate Shear Walls," Structural Engineering Report No. 107, Department of Civil Engineering, University of Alberta, Edmonton, AB, Canada.

Webster, D.J. (2013), "The Inelastic Seismic Response of Steel Plate Shear Wall Web Plates and Their Interaction with the Vertical Boundary Members," Ph.D. Dissertation, University of Washington, Seattle, WA.

Webster, D.J., Berman, J.W. and Lowes, L.N. (2014), "Experimental Investigation of SPSW Web Plate Stress Field Development and Vertical Boundary Element Demand," *Journal of Structural Engineering*, ASCE, Vol. 140, No. 6.

Guide for Authors

Scope *Engineering Journal* is dedicated to the improvement and advancement of steel construction. Its pages are open to all who wish to report on new developments or techniques in steel design, research, the design and/or construction of new projects, steel fabrication methods, or new products of significance to the uses of steel in construction. Only original papers should be submitted.

General Papers intended for publication should be submitted by email Margaret Matthew, editor, at **matthew@aisc.org**.

The articles published in the *Engineering Journal* undergo peer review before publication for (1) originality of contribution; (2) technical value to the steel construction community; (3) proper credit to others working in the same area; (4) prior publication of the material; and (5) justification of the conclusion based on the report.

All papers within the scope outlined above will be reviewed by engineers selected from among AISC, industry, design firms, and universities. The standard review process includes outside review by an average of three reviewers, who are experts in their respective technical area, and volunteers in the program. Papers not accepted will not be returned to the author. Published papers become the property of the American Institute of Steel Construction and are protected by appropriate copyrights. No proofs will be sent to authors. Each author receives three copies of the issue in which his contribution appears.

Manuscripts Manuscripts must be provided in Microsoft Word format. Include a PDF with your submittal so we may verify fonts, equations and figures. View our complete author guidelines at **www.aisc.org/ej**.

Smarter. Stronger. Steel.